UC San Diego
UC San Diego Electronic Theses and Dissertations

Title

Characterization and Deployment of the POLARBEAR-2b Receiver to Measure the Cosmic Microwave Background Polarization

Permalink

https://escholarship.org/uc/item/3qj480rv

Author

Ito, Jennifer Chiemi

Publication Date

2022

Peer reviewed|Thesis/dissertation

UNIVERSITY OF CALIFORNIA SAN DIEGO

Characterization and Deployment of the POLARBEAR-2b Receiver to Measure the Cosmic Microwave Background Polarization

A dissertation submitted in partial satisfaction of the
requirements for the degree
Doctor of Philosophy

in

Physics

by

Jennifer Chiemi Ito

Committee in charge:

Professor Kam Arnold, Chair
Professor Alison Coil
Professor Dan Green
Professor Shirley Meng
Professor Kaixuan Ni

2022

The dissertation of Jennifer Chiemi Ito is approved, and it is acceptable in quality and form for publication on microfilm and electronically.

University of California San Diego

2022

DEDICATION

To my family, my home.

EPIGRAPH

If I have seen further
it is by standing on the shoulders of Giants.
—Isaac Newton

TABLE OF CONTENTS

LIST OF FIGURES

LIST OF TABLES

ACKNOWLEDGEMENTS

In life and especially in the work presented in this dissertation, I stand on the shoulders of giants. I would like to all thank those who have taught me, worked with me, supported me, and encouraged me over the years. I would not have reached this point, accomplishing what I did, without you all.

Firstly, thank you to Kam Arnold who is an amazing role model of an advisor. Thank you for how you care about your graduate students and for all your technical guidance and mentorship. Thank you for the advice on work-life boundaries. Thank you for your patience and for encouraging me in my strengths and training me in my weaknesses. Finally, thank you for supporting me in my outreach endeavors, career ambitions, and especially as I transition to my new job.

To the broader UCSD cosmology group, thank you for the years of camaraderie. To Brian Keating, thank you for your leadership of the group. To Nick Galitzki and Grant Teply, thank you for your help especially early on in my graduate career in learning about Simons Array and the CMB. To my fellow graduate students, both past and present, thank you. Words cannot express how grateful I am to have been a part of this group with you all. To Max Silva-Feaver, thank you for sharing about the cosmology group in the first place. It has been great being in the same cohort and lab group with you. Thanks for all the runs to AoE. To Bryce Bixler, thanks for becoming one of my traveling and receiver assembling companions. To Tran Tsan, thank you for your faithful leadership of the Graduate Women in Physics group. It was really great being able to work with you in leading that organization. To Jake Spisak, Joe Seibert, Megan Russell, and Michael Randall, thank you for all the great times at lunch or BASH and always being willing to help me out, to make emergency shipments to the site, and to answer any questions I have. To those who graduated before me - David Leon, Lindsay Ng Lowry, Logan Howe, Marty Navaroli, Praween Siritanasak, and Tucker Elleflot, thank you for everything you taught me and always being willing to answer any questions I had. To Logan, Praween, and

To my UCSD friends I've made outside of my academic setting, thank you for the weekly meetings and boba tea runs. Specifically to Jacob Johnson, Esther Lim, and Tim Woodford, thank you for all the lunch hangouts, virtual and in-person. To Greg and Tanya Ehlert, thank you for always listening, sometimes for hours, and for all your emotional support and guidance as I navigated this stage in life.

To those who helped me get to graduate school. To Takashi Nakajima and Art Gerwig, the amazing professors of physics from my community college, thank you for how much you taught me about physics, education, and community. Thank you for having the confidence in me and my abilities to volunteer me as the supplemental instruction leader for your physics classes multiple semesters which sparked in me my desire to teach physics at the collegiate level. Your support and encouragement even after I moved on is much appreciated. Thanks to John Haberstroh who became my undergraduate research mentor while at UC Berkeley and led the Berkeley Compass Project which provided a community for us physics transfer students. Thank you to my research advisors at UC Berkeley. To Woon-Seng Choong, staff scientist at the Lawrence Berkeley National Laboratory who gave me my foot in the door to research, thank you for teaching me one of the most important lessons in my career - RTFM, read the * manual. To Chung-pei Ma, professor at UC Berkeley, thank you for giving me my first opportunity to work in astronomy research.

To my close friends who have been with me through multiple stages in life. To Sara and Daniel, it's been a privilege growing up with you two and an even greater honor keeping in touch as we've all gone our separate ways. Thank you for always being supportive of me and my endeavors through words of encouragement, regular video calls, and in-person hangouts. To Orphen, thank you for all the Palomar sunsets, Berkeley walks, and conversations about life over the many years. It is an honor to be living life alongside you. To Rachel, I don't think I would have survived a 350 sq. ft. studio for a year with anyone else. You're an amazing roommate and now dear friend. Thank you for all your continued constant support and encouragement

and sharing in life.

Thank you to Kyle for being so supportive of me and my research work and all my trips to Chile. Thank you for caring for me in so many different ways and always looking out for me. You inspire me to be a better person.

Finally, thank you to my amazing relatives and immediate family. You have been with me through it all, and your love and support have been constant. Thank you to my grandmother for letting me rent her condo for the entirety of my graduate career. Thank you to my parents for all your sacrifices, including taking care of my horse, and providing me the opportunity to attend graduate school. Thank you to Kid for being the best sister one could ask for and for all of your support and love and movie/music quotes.

VITA

2015	B. A. in Physics, University of California Berkeley
2015	B. A. in Astrophysics, University of California Berkeley
2018	M. S. in Physics, University of California San Diego
2022	Ph. D. in Physics, University of California San Diego

PUBLICATIONS

The POLARBEAR Collaboration: S. Adachi, T. Adkins, M. A. O. Aguilar Faúndez, K. S. Arnold, C. Baccigalupi, D. Barron, S. Chapman, K. Cheung, Y. Chinone, K. T. Crowley, T. Elleflot, J. Errard, G. Fabbian, C. Feng, T. Fujino, N. Galitzki, N. W. Halverson, M. Hasegawa, M. Hazumi, H. Hirose, L. Howe, J. Ito, O. Jeong, D. Kaneko, N. Katayama, B. Keating, T. Kisner, N. Krachmalnicoff, A. Kusaka, A. T. Lee, E. Linder, A. I. Lonappan, L. N. Lowry, F. Matsuda, T. Matsumura, Y. Minami, M. Murata, H. Nishino, Y. Nishinomiya, D. Poletti, C. L. Reichardt, C. Ross, Y. Segawa, P. Siritanasak, R. Stompor, A. Suzuki, O. Tajima, S. Takakura, S. Takatori, D. Tanabe, G. Teply, K. Yamada, Y. Zhou, Improved upper limit on degree-scale CMB B-mode polarization power from the 670 square-degree POLARBEAR survey, *The Astrophysical Journal*, Volume 931, Issue 2, May 2022

Darcy Barron, Kayla Mitchell, John Groh, Kam Arnold, Tucker Elleflot, Logan Howe, Jen Ito, Adrian T Lee, Lindsay N Lowry, Adam Anderson, Jessica Avva, Tylor Adkins, Carlo Baccigalupi, Kolen Cheung, Yuji Chinone, Oliver Jeong, Nobu Katayama, Brian Keating, Joshua Montgomery, Haruki Nishino, Christopher Raum, Praween Siritanasak, Aritoki Suzuki, Sayuri Takatori, Calvin Tsai, Benjamin Westbrook, Yuyang Zhou, Integrated Electrical Properties of the Frequency Multiplexed Cryogenic Readout System for Polarbear/Simons Array, *IEEE Transactions on Applied Superconductivity*, Volume 31, Issue 5, March 2021, Pages 1-5.

Yuuko Segawa, Haruaki Hirose, Daisuke Kaneko, Masaya Hasegawa, Shunsuke Adachi, Peter Ade, Mario Andrés Osvaldo Aguilar Faúndez, Yoshiki Akiba, Kam Arnold, Jessica Avva, Carlo Baccigalupi, Darcy Barron, Dominic Beck, Shawn Beckman, Federico Bianchini, David Boettger, Julian Borrill, Julien Carron, Scott Chapman, Kolen Cheung, Yuji Chinone, Kevin Crowley, Ari Cukierman, Tijmen de Haan, Matt Dobbs, Rolando Dunner, Hamza El Bouhargani, Tucker Elleflot, Josquin Errard,

Giulio Fabbian, Stephen Feeney, Chang Feng, Takuro Fujino, Nicholas Galitzki, Neil Goeckner-Wald, John Groh, Grantland Hall, Nils Halverson, Takaho Hamada, Masashi Hazumi, Charles Hill, Logan Howe, Yuki Inoue, Jennifer Ito, Greg Jaehnig, Oliver Jeong, Nobuhiko Katayama, Brian Keating, Reijo Keskitalo, Shuhei Kikuchi, Theodore Kisner, Nicoletta Krachmalnicoff, Akito Kusaka, Adrian T Lee, David Leon, Eric Linder, Lindsay Ng Lowry, Aashrita Mangu, Frederick Matsuda, Yuto Minami, Josh Montgomery, Martin Navaroli, Haruki Nishino, Julien Peloton, Anh Thi Phuong Pham, Davide Poletti, Giuseppe Puglisi, Christopher Raum, Christian L Reichardt, Colin Ross, Maximiliano Silva-Feaver, Praween Siritanasak, Radek Stompor, Aritoki Suzuki, Osamu Tajima, Satoru Takakura, Sayuri Takatori, Daiki Tanabe, Grant P Teply, Calvin Tsai, Clara Verges, Ben Westbrook, Yuyang Zhou, Method for rapid performance validation of large TES bolometer array for POLARBEAR-2A using a coherent millimeter-wave source, *AIP Conference Proceedings*, Volume 2319, Issue 1, February 2021.

J Ito, LN Lowry, T Elleflot, KT Crowley, L Howe, P Siritanasak, T Adkins, K Arnold, C Baccigalupi, D Barron, B Bixler, Y Chinone, J Groh, M Hazumi, CA Hill, O Jeong, B Keating, A Kusaka, AT Lee, K Mitchell, M Navaroli, ATP Pham, C Raum, CL Reichardt, TJ Sasse, J Seibert, A Suzuki, S Takakura, GP Teply, C Tsai, B Westbrook, Detector and readout characterization for POLARBEAR-2b, *International Society for Optics and Photonics*, Volume 11453, December 2020, Conference Millimeter, Submillimeter, and Far-Infrared Detectors and Instrumentation for Astronomy X.

T Elleflot, K Arnold, D Barron, KT Crowley, M Dobbs, J Groh, M Hasegawa, M Hazumi, C Hill, L Howe, J Ito, O Jeong, D Kaneko, N Katayama, B Keating, A Kusaka, AT Lee, LN Lowry, C Raum, J Seibert, M Silva-Feaver, P Siritanasak, A Suzuki, S Takakura, S Takatori, C Tsai, B Westbrook, Effect of stray impedance in frequency-division multiplexed readout of TES sensors in POLARBEAR-2b, *Journal of Low Temperature Physics*, Volume 199, Issue 3, May 2020, Pages 840-848.

Jenny E Greene, Melanie Veale, Chung-Pei Ma, Jens Thomas, Matthew E Quenneville, John P Blakeslee, Jonelle L Walsh, Andrew Goulding, Jennifer Ito, The MASSIVE Survey. XII. Connecting Stellar Populations of Early-type Galaxies to Kinematics and Environment, *The Astrophysical Journal*, Volume 874, Issue 1, March 2019, Pages 66-88.

Irina Ene, Chung-Pei Ma, Melanie Veale, Jenny E Greene, Jens Thomas, John P Blakeslee, Caroline Foster, Jonelle L Walsh, Jennifer Ito, Andy D Goulding, The MASSIVE Survey – X. Misalignment between kinematic and photometric axes and

intrinsic shapes of massive early-type galaxies, *Monthly Notices of the Royal Astronomical Society*, Volume 479, Issue 2, September 2018, Pages 2810–2826.

Melanie Veale, Chung-Pei Ma, Jenny E. Greene, Jens Thomas, John P. Blakeslee, Jonelle L. Walsh, Jennifer Ito, The MASSIVE survey – VIII. Stellar velocity dispersion profiles and environmental dependence of early-type galaxies, *Monthly Notices of the Royal Astronomical Society*, Volume 473, Issue 4, February 2018, Pages 5446–5467.

Melanie Veale, Chung-Pei Ma, Jenny E. Greene, Jens Thomas, John P. Blakeslee, Nicholas McConnell, Jonelle L. Walsh, Jennifer Ito, The MASSIVE Survey – VII. The relationship of angular momentum, stellar mass and environment of early-type galaxies, *Monthly Notices of the Royal Astronomical Society*, Volume 471, Issue 2, October 2017, Pages 1428–1445, https://doi.org/10.1093/mnras/stx1639

Melanie Veale, Chung-Pei Ma, Jens Thomas, Jenny E. Greene, Nicholas J. McConnell, Jonelle Walsh, Jennifer Ito, John P. Blakeslee, Ryan Janish, The MASSIVE Survey – V. Spatially resolved stellar angular momentum, velocity dispersion, and higher moments of the 41 most massive local early-type galaxies, *Monthly Notices of the Royal Astronomical Society*, Volume 464, Issue 1, January 2017, Pages 356–384.

ABSTRACT OF THE DISSERTATION

Characterization and Deployment of the POLARBEAR-2b Receiver to Measure the Cosmic Microwave Background Polarization

by

Jennifer Chiemi Ito

Doctor of Philosophy in Physics

University of California San Diego, 2022

Professor Kam Arnold, Chair

The Simons Array, located in the Atacama Desert in northern Chile, is a project designed to measure the polarization of the cosmic microwave background (CMB). Studying the CMB in this capacity provides insight into the history of our Universe and contributes to the understanding of its current evolution. The POLARBEAR-2b receiver is the second cryogenic receiver designed and built for the Simons Array. This instrument houses over 7,000 transition-edge sensor bolometers cooled to a base temperature of 250 millikelvin that are read out with a digital frequency multiplexing scheme that minimizes the internal wiring. The signals are amplified using superconducting quantum interference devices that are cooled to 4 Kelvin. The optical

components of this receiver include a ultra-high molecular weight polyethelyne window, a cryogenic, continuously rotating half-wave plate, an infrared-blocking filter, and three reimaging alumina lenses with a lyot aperture. Careful assembly methods of all the elements mentioned to build the receiver are necessary to ensure successful operation of the instrument during in-lab testing and in the field.

POLARBEAR-2b was integrated at UC San Diego before it began its deployment in January 2020 and was hoisted onto the Paul Simons telescope in July of 2022. This dissertation focuses on the final in-lab integration testing and results as well as the receiver assembly methods and modifications that enabled a successful field deployment of the POLARBEAR-2b receiver.

Chapter 1

Cosmology and the Cosmic Microwave Background

1.1   Modern Cosmology

Cosmology is firstly defined as "a branch of philosophy dealing with the origin and general structure of the universe, with its parts, elements, and laws, and especially with such of its characteristics as space, time, causality, and freedom," with the second definition being "the branch of astronomy that deals with the general structure and evolution of the universe" [7]. While cosmology is commonly known as a specialization of physics and astronomy, cosmology as a branch of philosophy predates its emergence as a field in physics and astronomy. Before cosmology was cosmogony[1] which focused on the origin of the Universe instead of just the structure and evolution; hence, this type of study of the Universe was more philosophical and religious in nature [20]. However, beginning in 1917 with Einstein's theory of general

---

[1]Perhaps one of the greatest confusions is this difference between cosmology and cosmogony. Cosmology is the study of the structure and evolution of the Universe whereas cosmogony is the study of the origin of the Universe. Cosmology may imply a cosmogony, but it does not directly define it.

relativity, cosmology quickly developed strictly as a branch of physics and astronomy and has continued to indirectly describe a cosmogony [34, 20].

Einstein's first solution to his general relativity equations resulted in a static, eternal Universe. However, in 1922, physicist Alexander Friedmann presented a mathematical argument that multiple dynamical models of possible Universes could be described using Einstein's general theory of relativity. This is the first time that an origin for the Universe was derived from physics and not philosophy [20]. In 1931, a Belgian astrophysicist and priest Georges Lemaître proposed a solution to Einstein's theory that described the Universe as currently expanding and having a beginning as a "primeval atom". During this time, the late 1920s, Edwin Hubble determined experimentally that the Universe is expanding.

While there was now evidence for an expanding Universe, the dominant cosmogony remained that the Universe did not have a beginning but remained in a steady state where matter was continuously being created in the expanding Universe. However, a rivaling theory, nicknamed the "big-bang theory" by its critics, was postulated by George Gamow in a 1948 paper. Building on Lemaître's primeval atom, Gamow proposed that the "big-bang" Universe would at first be radiation dominated, and as the Universe expanded, the energy would convert mostly to matter. Ralph Alpher and Robert Herman joined Gamow in his work and predicted that a remnant of radiation would remain from this "big-bang" and have a temperature of around 5 degrees Kelvin. In 1963, astronomers Arno Penzias and Robert Wilson discovered an all-sky microwave radiation that was analyzed in 1965 by Robert Dicke as radiation having a temperature of about 3 degrees Kelvin [12]. This discovery was accepted as the remnant radiation of the big-bang and is known as the cosmic microwave background. With this, the big-bang model became the foundation for the current widely accepted model for modern cosmology - the standard cosmological model.

1.2   The Standard Cosmological Model

Einstein's general theory of relativity provides a way to see how energy in and the geometry of the Universe are related. Einstein's original equations can be expressed as shown in Equation 1.1.

$$G_{\mu\nu} = 8\pi G T_{\mu\nu} \tag{1.1}$$

The energy information is incorporated into $T_{\mu\nu}$ which is the energy-momentum tensor. The geometry of the Universe is described with the Einstein tensor $G_{\mu\nu}$. The variable G is the gravitational constant, and the speed of light is set to 1.

Later, Einstein added a parameter called the cosmological constant. Although he removed the constant when it was determined that the Universe was expanding, the cosmological constant has been reinserted as it has been observationally determined as necessary for describing a dynamical Universe [24]. The general relativity equations for the current cosmological model is then

$$G_{\mu\nu} + \Lambda g_{\mu\nu} = 8\pi G T_{\mu\nu} \tag{1.2}$$

The cosmological constant is Λ, and $g_{\mu\nu}$ is the metric tensor.

To solve this, the cosmological principle is applied which states the Universe is homogeneous and isotropic. Homogeneity means that the Universe is the same everywhere while isotropy means that there is no preferred direction in space. Having one does not automatically imply the other is true. The metric[2] that satisfies the cosmological principle is known as the Friedmann-Lemaître-Robertson-Walker (FLRW) metric and can be written as

---

[2]A metric turns coordinate distance into a physical distance. In two dimensional coordinate geometry, the metric is the Pythagorean theorem which tells the physical distance between two coordinate points. In general, there are four space-time dimensions - time and three spatial dimensions.

$$ds^2 = \sum_{\mu\nu=0}^{3} g_{\mu\nu} dx^\mu dx^\nu \qquad (1.3)$$

where

$$g_{\mu\nu} = \begin{pmatrix} -1 & 0 & 0 & 0 \\ 0 & a^2(t) & 0 & 0 \\ 0 & 0 & a^2(t) & 0 \\ 0 & 0 & 0 & a^2(t) \end{pmatrix} \qquad (1.4)$$

The variable a is a parameter called the scale factor and describes the expansion of the Universe. This scale factor measures the physical coordinate distance of a system. Figure 1.1 illustrates how the coordinate system itself is scaling up while the coordinates of the box corners remain constant as a function of time. Each side of the box (physical distance) is expressed as the scale factor as a function of time $a(t)$ multiplied by the distance between two coordinates. How $a(t)$ evolves with time is dependent on the energy density of the Universe. The scale factor at present day equals 1.
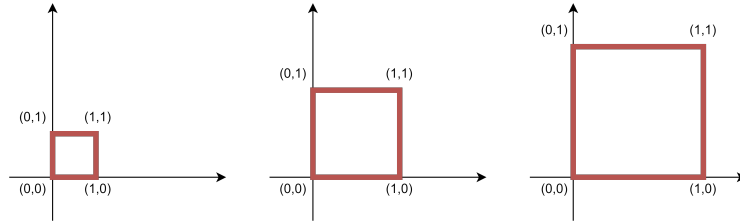
Figure 1.1: This figure illustrates the expansion of a coordinate system. The co-moving distance (distance between two coordinate points) remains constant while the physical distance grows as time progress from left to right. The physical distance is proportional to the co-moving distance times the scale factor which increases with time.

The Hubble parameter is defined as Equation 1.5 and shows how quickly the scale factor changes. The numerator is the time derivative of the scale factor.

$$H(t) \equiv \frac{\dot{a}}{a} \tag{1.5}$$

After using the FLRW metric to solve Einstein's equations, the result is the Friedmann equations which is a function of curvature of the Universe. There are three different options for curvature. The first is a spherical or closed geometry where the sum of the angles in a triangle equal more than 180°. The second possible geometry is the hyperbolic or open geometry where the sum of the angles in a triangle equal less than 180°. The third possibility is a flat geometry where the sum of the angles in a triangle equals 180°. Assuming the cosmological principle and a flat Universe, the first Friedmann equation can be written as

$$H^2(t) = \frac{8\pi G}{3}\left[\rho(t) + \frac{\rho_c - \rho_0}{a^2(t)}\right] \tag{1.6}$$

where

$$\rho_c = \frac{3H_0^2}{8\pi G} \tag{1.7}$$

which is called the critical density. Here, G is the gravitational constant and H_0 is the present day Hubble parameter.

Another method for determining the geometry of the Universe is by the density parameter Ω. The density parameter (Equation 1.8) is the ratio of the observed energy type over the critical density. The sum of the density parameters for each type of energy describes the curvature of the Universe. If Ω_{total} is 1, then the Universe is flat. If $\Omega_{total} < 1$, the Universe is closed. If $\Omega_{total} > 1$, the Universe is open.

$$\Omega = \frac{\rho}{\rho_c} \tag{1.8}$$

The current calculation for the density parameter is very close to but not exactly one indicating that our Universe is very close to flat. One method of determining the

5

energy densities in the Universe is by studying the cosmic microwave background.

1.3 The Cosmic Microwave Background

The early high energy state that Gamow proposed is presently described as an ionized plasma of nuclei, electrons, and photons. The temperature was above 3000 K so no stable atoms could form since any bound electron was immediately scattered by a high energy photon. Through these collisions, the photons are in thermal equilibrium and can be described as black-body radiation. Equation 1.9 shows the intensity of a gas of photons with a black-body spectrum as a function of frequency.

$$I_\nu = \frac{4\pi\hbar\nu^3/c^2}{\exp\{2\pi\hbar\nu/k_B T\} - 1} \tag{1.9}$$

As the Universe expanded, it cooled and a phenomenon known as Big Bang Nucleosynthesis occurred which determined the relative abundances of cosmic particles. As the Universe continues to cool, photons also lose energy and can no longer easily ionize nuclei. Neutral hydrogen forms beginning an epoch called recombination, and at the end, photons no longer interact with any atoms and are thereby decoupled and free-streaming. These free-streaming photons are what make up the cosmic microwave background (CMB).

With the expansion of the Universe, the number density of photons decreases and the photons are redshifted. The relationship between redshift (z) and the wavelength and the scale factor (a) is shown in Equation 1.10

$$1 + z \equiv \frac{\lambda_{obs}}{\lambda_{emit}} = \frac{1}{a} \tag{1.10}$$

Due to how energy density changes with frequency and temperature, the CMB retains its black-body spectrum [22]. Presently, the CMB is measured to have a black-body spectrum with a temperature of 2.725 ± 0.001 Kelvin.

After its initial discovery, the CMB has been rigorously studied and continues to push the advancement of scientific technologies to better study the CMB. The Cosmic Background Explorer (COBE) satellite was the first instrument to show that the predicted blackbody spectrum of the CMB and the actual measurement of the CMB agreed (Figure 1.2). This study confirmed the homogeneous and isotropic nature of the CMB.
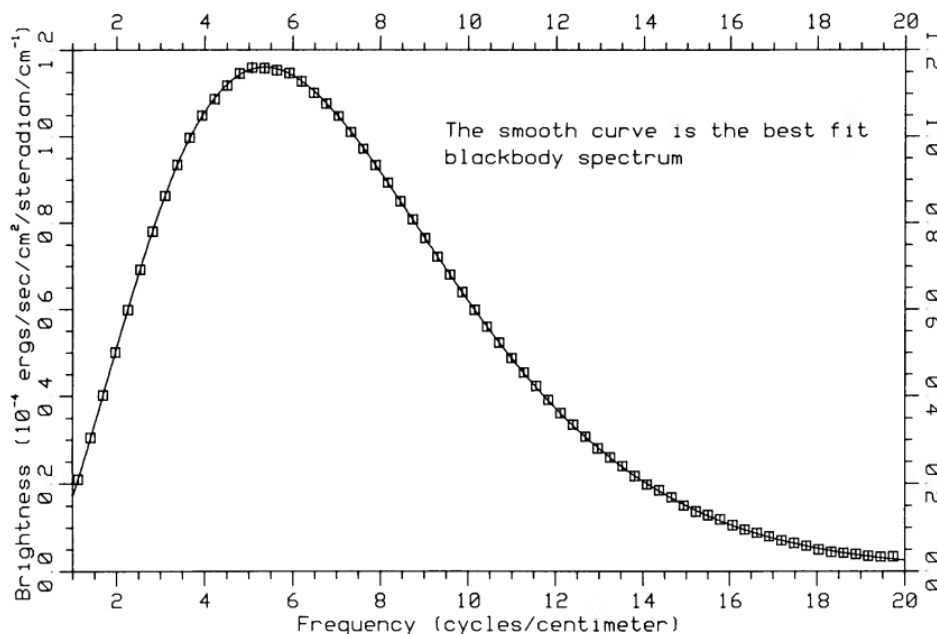
Figure 1.2: This plot shows the initial measurement of the CMB taken by the COBE satellite. The data points are well-fit by a black-body spectrum curve. The plot is taken from the original paper published in 1990 [25].

1.3.1 Temperature Anisotropies

While the CMB is isotropic to less than $\sim 0.01\%$, there are small temperature fluctuations over different spatial areas. Instead of looking at deviations over spatial dimensions, it is possible to quantify a temperature power spectrum as a function of angular scale. The initial ionized plasma can be modeled as a perfect fluid with

gravitational potential wells. Baryonic matter falls into the potential well, and the density oscillates creating temperature fluctuations. The oscillations can be treated like sounds waves and described as a superposition of harmonic oscillators of different scales. The CMB temperature map of the sky can be Fourier transformed in order to understand the magnitude of the oscillations across the different size scales.

The temperature power spectrum is depicted by Figure 1.3 from the Planck Collaboration. The x-axis are the spherical harmonics that denote angular scale. The smaller ℓ represents larger angular scale and the higher ℓ represents small angular scales. The corresponding angle for a given ℓ is

$$\theta \approx \frac{180°}{\ell}$$

The y-axis is

$$D_\ell^{TT} = \frac{\ell(\ell+1)C_\ell^{TT}}{2\pi} \tag{1.11}$$

where

$$C_\ell = \frac{1}{2\ell+1} \sum_{m=-\ell}^{\ell} \langle a_{\ell m} a_{\ell m}^* \rangle \tag{1.12}$$

represents the power spectrum amplitude where a_{lm} is the amplitude of the associated spherical harmonic in the decomposition of the sky map into its spherical harmonic components.

The resulting temperature power spectrum contains information beyond temperature fluctuations. The location and relative heights of its peaks encode the distribution of energy in the Universe as well as its geometry. The features shown in Figure 1.3 can be described by a single 6-parameter model [30]. The six parameters used are the baryon density today, the cold dark matter density today, the Thomson scattering optical depth due to reionization, the scalar spectrum power-law index,
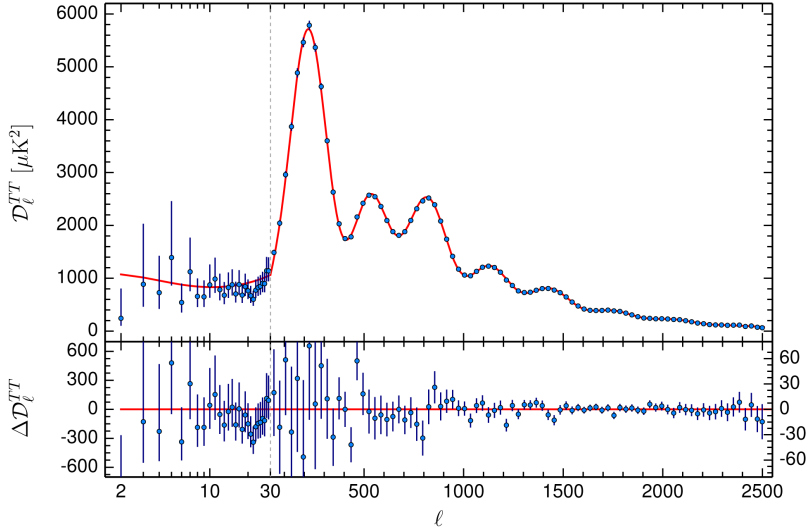
Figure 1.3: This figure shows the temperature power spectrum as a function of spherical harmonics (ℓ). The blue points are analyzed data from Planck and the red line is the theoretical curve. The bottom plot shows the residuals between the data and theory. Figure courtesy of the ESA and the Planck Collaboration [30].

the log power of the primordial curvature perturbations, and an approximation to the angular size of the sound horizon [29].

The first peak provides information about the geometry of the Universe. The position in ℓ of the first peak contains information regarding densities of different types of energy and is consistent with a flat Universe. The relative height and location of the second peak tells more about baryon matter in the Universe. The more baryons means the second peak is relatively suppressed compared to the first peak. The amount of baryons also affects the peak positions slightly by slowing oscillations and by damping oscillations which would be more evident in the tail of the curve. The relative height of the third peak indicates the amount of dark matter in the Universe. The amount of dark matter would also affect the location of the peaks. The position of the higher peaks and the rate at which they are damped can provide further confirmation on the relative energy densities and curvature of the Universe. These higher peaks are on angular scales that are smaller than the mean

9

free path of a photon at recombination. As a photon executes a random walk path, it may thermally average out which would eliminate any temperature fluctuations on that scale causing the amplitude of the peaks at high ℓ to be exponentially damped.

1.3.2 Polarization

Another effect of temperature anisotropies is the polarization of the CMB. The polarization is theorized to come from Thomson scattering that occurred in quadrupole temperature anisotropies that existed during recombination. Thomson scattering occurs when a photon elastically scatters off of a free charged particle such as an electron. It polarizes photons similarly to how photons are polarized when scattering off a surface. The result is linear polarization of the CMB photon.

Quadrupole temperature anisotropies can be generated by two means - scalar and tensor perturbations. Scalar perturbations are equivalently density perturbations. The resulting relatively high and low density regions correspond to hot and cold spatial regimes which create quadrupole anisotropies. Tensor perturbations, or gravitational waves, squeeze and stretch space creating hot and cold regions. Thompson scattering from density perturbations cause photons to have curl-free polarization and as such are called E-modes, while tensor perturbations imprint divergence-free polarization and are referred to as B-modes. Gravitational lensing can also convert E-mode polarization into B-mode polarization.

1.4 Inflation

There are two dominant inconsistencies that arise with an isotropic and flat Universe.

- Horizon problem - Given the age of the Universe at the time of last scattering, there is not enough time for the CMB to be homogeneous and isotropic. CMB

photons on opposite sides of the Universe are not in causal contact.

- Flatness problem - Also known as a fine-tuning problem, the flatness problem addresses the fact that very unique circumstances had to have happened for the Universe to have the nearly flat geometry we observe today as being just under or over dense would cause a run-away effect.

In order to address these two problems, a theory called inflation has been developed as an event that would be evident in the temperature anisotropies and polarization of the CMB. Inflation is a theorized hyper-expansion of the Universe less than fractions of a second after physical energy came into existence[3]. It solves the horizon problem since photons that began in causal contact are rapidly spread out such that they are still in thermal equilibrium. This rapid expansion also generates a scenario where under certain conditions the Universe would asymptote to a flat geometry.

While inflation can explain the mechanisms that caused some of the aforementioned observed properties in the CMB, the evidence that is considered as the "smoking-gun" proof for inflation would be finding primordial B-mode polarization in the CMB. This polarization would be caused by tensor perturbations that developed from inflation. Finding this polarization is the scientific motivation for the project that is described in this dissertation.

1.5   Foregrounds

There are other millimeter wavelength signals that contaminate the CMB signal and obfuscate the search for primordial B-modes. These signals are termed as foregrounds. Some are polarized while others are not. Careful removal of the polarized foregrounds is necessary to accurately detect a primordial B-mode signal.

---

[3]Some call this singular event the Big Bang while others define the Big Bang as something that is continuing now.

The first common culprit that dominates at frequencies above 100 GHz is thermal dust emission from our galaxy. In the interstellar medium, there are dust grains that emit thermal radiation from intrinsic vibrations. The second common source of foreground is synchrotron radiation. Synchrotron radiation dominates at lower frequencies. It is broadband emission that occurs when charged particles travel in curved paths, such as cosmic ray electrons being affected by the galactic magnetic field. Both thermal emissions from dust and synchrotron radiation are polarized foregrounds. Figure 1.4 shows the RMS brightness temperature as a function of frequency for the CMB, thermal dust emissions, and synchrotron radiation. Brightness temperature is the blackbody temperature that a source would have to have such that its intensity at that frequency matches that of a blackbody.
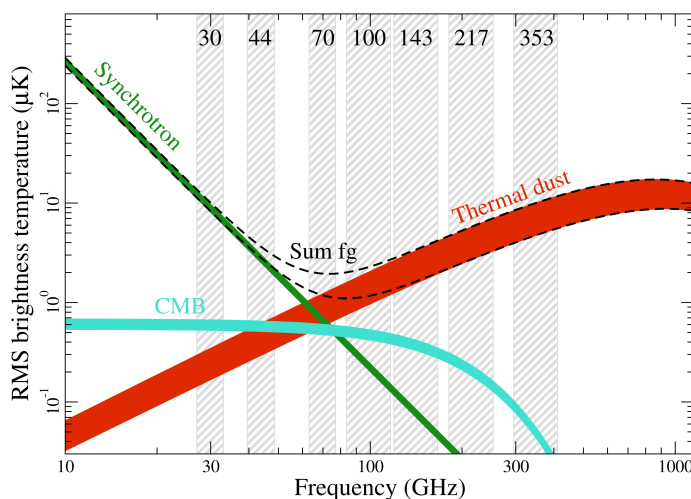
Figure 1.4: This figure shows the RMS brightness temperature vs frequency of the CMB, thermal dust emissions, and synchrotron radiation. The black dotted lines show the sum of these two foreground emissions. Figure courtesy of the ESA and the Planck Collaboration [28].

12

1.6   State of the Field

Discovering this primordial B-mode polarization of the CMB is an exciting and ongoing area of research. In addition to primordial B-modes, further study on lensed B-modes is pursued to study the matter distribution in the Universe and to better understand constraints on the sum of neutrino masses. The current B-mode power spectrum from four ground-based CMB experiments is shown in Figure 1.5.
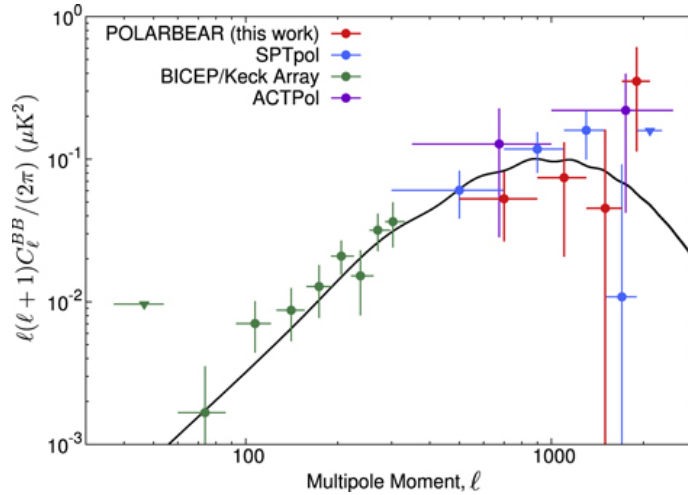
Figure 1.5: This plot shows the B-mode polarization spectrum from four ground-based CMB experiments. The black curve is the theoretical 2015 Planck ΛCDM spectrum. The figure was generated by the POLARBEAR Collaboration and was originally published in [2].

The following chapters focus on detailing the Simons Array which is a set of next-generation POLARBEAR receivers whose science goals are to detect primordial B-modes and contribute to the current studies on the lensed B-modes. The last published sensitivity projections for Simons Array are $\sigma(r) = 0.006$ for $r = 0.1$ and $\sigma(\Sigma_{i=1}^3 m_\nu^i) = 40$ meV for the sum of neutrino masses [19].

1.7 Acknowledgements

The dissertation author acknowledges the authors of [25] for Figure 1.2.

The dissertation author acknowledges the ESA and the Planck Collaboration for Figures 1.3 and 1.4 that were originally published in [30] and [28] respectively.

The dissertation author acknowledges the POLARBEAR Collaboration for Figure 1.5.

Chapter 2

Simons Array Overview

2.1 Observation Site

The Simons Array telescopes are located on the Cerro Toco plateau in northern Chile. They sit at an elevation of 5200 meters where the atmosphere is approximately half of that at sea level. Due to atmospheric water vapor reflecting and emitting millimeter wavelength light, the geographical site to establish these ground-based instruments must be in a dry environment to reduce pollution of the CMB signal. The water in the atmosphere is measured by a metric called precipitable water vapor (PWV) which is a unit that measures the equivalent depth of water that could be precipitated in a column of atmosphere. On average, the PWV at the Cerro Toco plateau is ~1 mm.

Figure 2.1 shows the atmospheric transmission as a function of frequency. The CMB as a 2.725 Kelvin blackbody has a peak frequency of ~ 160 GHz and is also measurable at 90 GHz. Therefore, our CMB detectors were designed to take advantage of the two transmission windows containing these frequencies. Figure 2.1 also shows how different levels of PWV affects transmission as a function of frequency. Water vapor and oxygen emit photons within our detector frequencies which gen-

erates a fundamental limit to our sensitivity. This emphasizes the requirement of a low-PWV observation site for ground-based instruments. Larger PWV levels cut transmission particularly at higher frequencies.
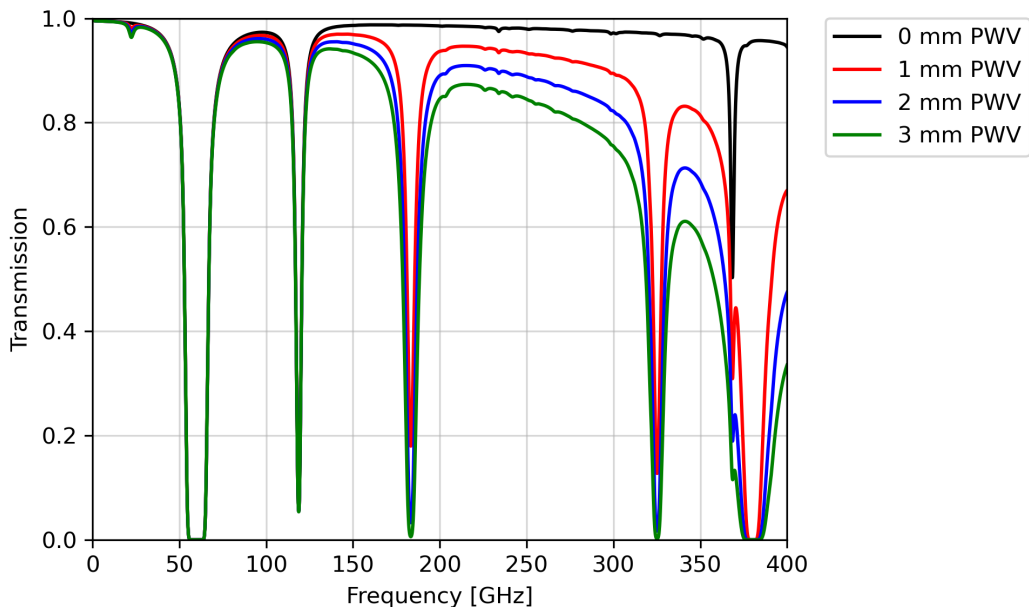
Figure 2.1: A plot that shows the transmission windows given different levels of PWV. The upper most curve is with hypothetical 0 mm of PWV, and as the PWV increases, the maximum transmission, especially at higher frequencies, decreases. The average PWV at the site is $\sim$ 1 mm. This plot was generated using the am modeling software [27]

2.2 The Simons Array Telescopes

Simons Array is a set of three identical telescopes coupled with cryogenic receivers. They are roughly arranged in a line from north to south. The northern most telescope, which is the Nicholas Simons telescope, hosts the Polarbear-2a (PB-2a) receiver and has been undertaking an engineering run since its first light in 2018. The

southern most telescope, the Paul Simons telescope, is the new home of the second receiver, namely POLARBEAR-2b (PB-2b). The middle telescope is the Huan Tran telescope which houses the original POLARBEAR receiver. The third receiver of Simons Array, POLARBEAR-2c (PB-2c), will replace this original POLARBEAR receiver in this telescope.

The telescopes utilize a Gregorian Mizuguchi-Dragone design which provides low cross polarization and low astigmatism [37, 36]. Each telescope has a 2.5 meter primary mirror coupled to a 1.3 m-diameter secondary mirror which then couples to the receiver. Panels around the primary mirror are installed to reduce ground reflections and extend the primary diameter to 3.5 meters. The secondary mirror is enclosed in the receiver enclosure with the receiver. The telescope can move in azimuth $400°$ and elevation from just below the horizon at $(0°)$ to zenith $(90°)$.

A boom structure extends from the base of the primary mirror and is the attachment point for the receiver, its enclosure, and the saddlebags. The saddlebags are cabinets that house the electronics for reading out the detectors, receiver controllers, and monitoring receiver temperatures (housekeeping). The receiver enclosure is made of aluminum honeycomb panels that are bolted to an aluminum frame that is attached to the boom structure. The enclosure is designed to protect the receiver and secondary mirror from the outside elements. A baffle cone allows photons from the primary mirror to enter the receiver enclosure.

2.3 Polarbear-2 Receivers

POLARBEAR-2 receivers (PB-2) are cryogenic structures and the next generation of the original POLARBEAR cryogenic receiver (PB-1) that began observations in 2012. While the general structure of the PB-1 and PB-2 receivers is the same, a PB-2 receiver houses nearly six times as many detectors as PB-1 and incorporates new polarization modulator technologies and other changes necessary for supporting
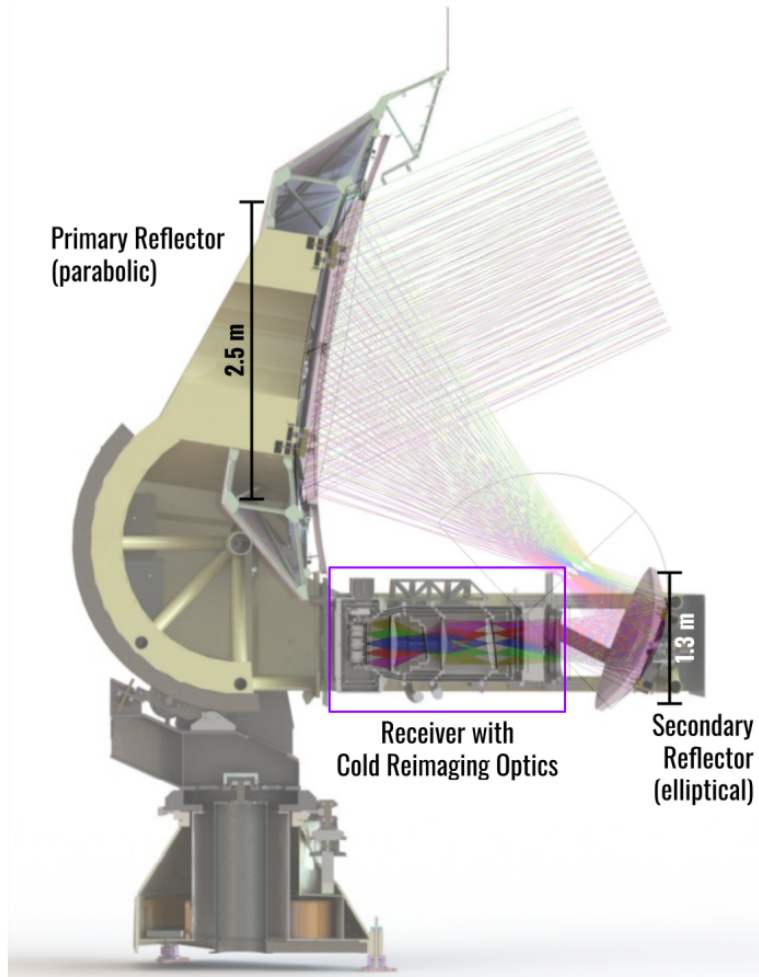
Figure 2.2: Cross section of the telescope with the receiver overlaid with a ray diagram. Figure courtesy of Lindsay Ng Lowry and was originally published in [23].

more detectors. This section describes the general structure of PB-2 receivers with some notes specifically regarding PB-2b as PB-2b is the focus of this dissertation.

Each receiver consists of two sections, the backend and the optics tube. Figure 2.3 shows a cross section of the receiver with some dimensions and major components labeled. The section from the backend aperture to the window is referred to as the optics tube, and the section to the left of the backend aperture is called the backend. The backend section houses the detectors and cold detector readout. The optics tube, as the name implies, houses all the optical elements. The receiver as a whole consists of nested aluminum shells with the innermost shells at a nominal temperature of 4 K, the middle shells at a nominal temperature of 50 K, and the outermost shells at ambient temperature ($\sim$ 300 K). Multi-layer insulation (MLI) is placed in between each set of shells to thermally isolate them from each other. The focal plane of detectors is further cooled by a ^{3}He/^{4}He fridge to 0.25 K.

2.3.1   Receiver Structure

The Backend

The backend of the receiver has outer dimensions of approximately 1.2 m $\times$ 0.4 m $\times$ 0.9 m. The 4 K shell is divided into two compartments with a rectangular opening in between. The larger section houses the focal plane tower (FPT) and superconducting quantum interference devices (SQUIDs) for reading out the detectors. The smaller section houses thermometry readout boards for the FPT, millikelvin refrigerator, and 4 K shell. The millikelvin refrigerator heatstraps are fed through the rectangular opening between the two compartments connecting the FPT to the millikelvin fridges.
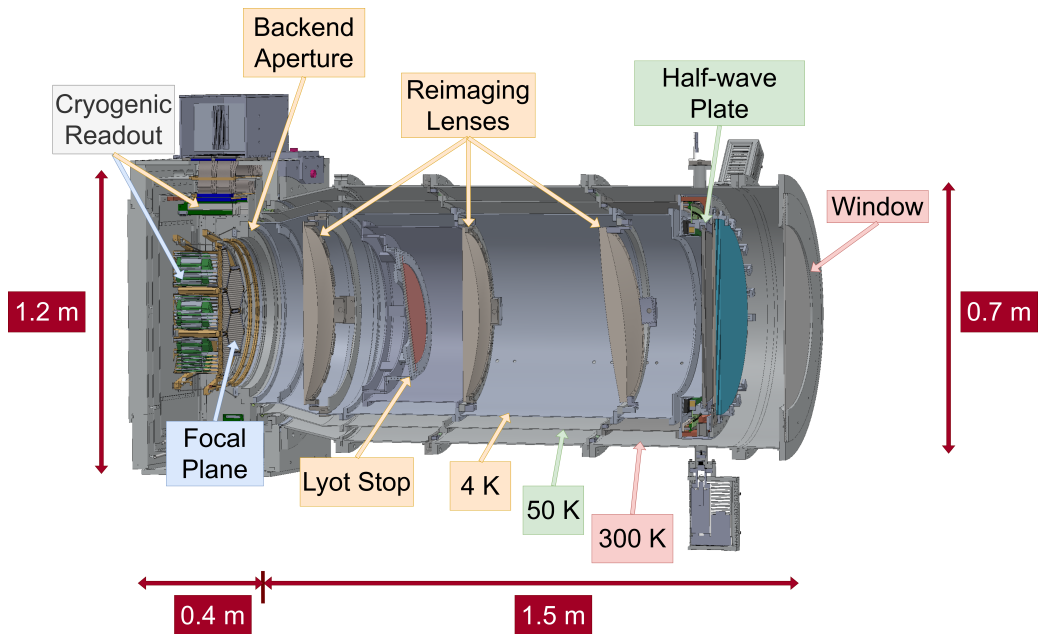
Figure 2.3: Cross section of the PB-2b receiver, the second of the three Simons Array receivers. The box-like structure on the left side of the backend aperture is the backend, and the cylindrical structure extending to the right of the backend aperture is the optics tube. Unique to PB-2b is the half-wave plate inside the receiver (Section 2.4.1).
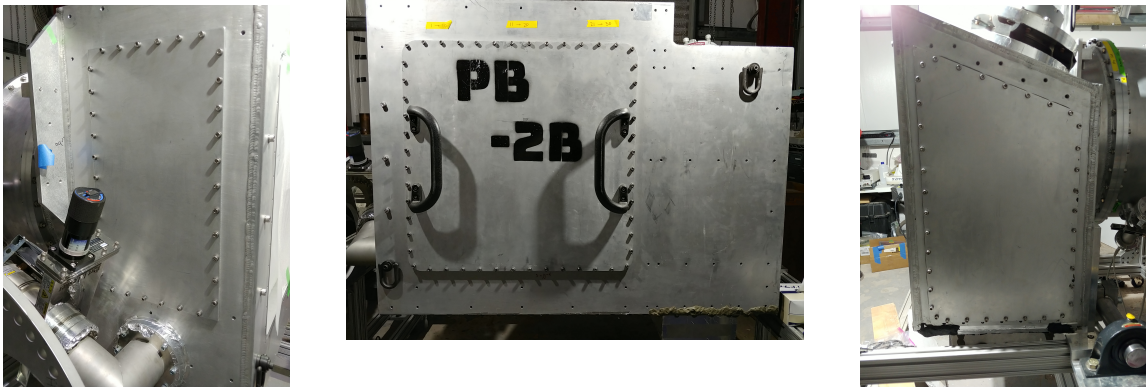
Figure 2.4: Three photos that show the three different sides of the backend. The center image is the backdoor of the backend, and the left and right photos are the left and right sides respectively of the backend. The front (not shown) has the backend aperture to which the optics tube is mounted. The left side is referred to as the turbo side since an Agilent turbo pump is mounted on that side for pumping out the receiver. The right side is referred to as the PTC side since that side has the backend pulse-tube cryocooler mounted in it.

The Optics Tube

The optics tube is also built from sets of three concentric cylindrical shells, where the innermost shell is at 4 K, the middle shell is at 50 K, and the outermost shell is the vacuum shell at room temperature (~ 300 K). It measures approximately 1.5 meters in length and 0.7 meters in diameter. There are three anti-reflection coated alumina lenses and a lyot stop that resides in the 4 K shell. At 50 K, there is an alumina infrared (IR) blocking filter. A millimeter wavelength transparent cap is placed on the sky-side end of the outermost shell. This cap is referred to as the "window" and vacuum seals the sky-side of the optics tube.

2.3.2   Receiver Cryogenics

There are two pulse tube cryocoolers (PTCs) integrated with the receiver. One is installed in the backend, and the other is mounted in the optics tube. Each PTC

has two stages (coldheads) with the first stage providing ~ 50 W of cooling power at 50 K with ~ 1.35 W of cooling power at 4 K for the second stage. The entire cooling system is comprised of a compressor, pressurized hoses and a PTC. These PTCs utilize adiabatic expansion and compression of helium gas to extract heat from the system. We use PT415 cryocoolers and systems provided commercially by Cryomech[1].

The cryogenic requirements of the receiver come from the necessity of cooling multiple components to certain temperatures. In the backend, the detectors and cryogenic readout have certain requirements. Fundamentally, the detector noise is determined by the temperature at which they are operated, so to keep the detector noise below the photon noise from the atmosphere, the detector bath temperature must be $\sim<0.3$ K. The superconducting transition temperature of the detector is set using this requirement and must be cooled below its transition temperature for operation. Other superconducting components like lossless transmission lines and SQUIDs are used and must be cooled below their superconducting transition temperature in order to use them as intended. In the optics tube, the reimaging lenses and the lyot stop are cooled to ~ 4 K to minimize their optical loading on the detectors. In PB-2b, the cryogenic half-wave plate (Section 2.4.1) must be cooled below its critical temperature so that it can levitate.

At UC San Diego, the PB-2b backend with its PTC was validated independently and calculated to have a loading of ~ 40 W on the 50 K stage and ~ 0.30 W on the 4 K stage [15]. The PB-2b optics tube was validated at UC Berkeley and calculated to have a loading of ~ 38 W on the 50 K stage and ~ 0.8 W on the 4 K stage [18]. Figure 2.5 shows the receiver cooling of the final in-lab PB-2b receiver run after integration in the lab at UCSD.

For cooling to sub-Kelvin temperatures, we use helium adiabatic refrigerators

---
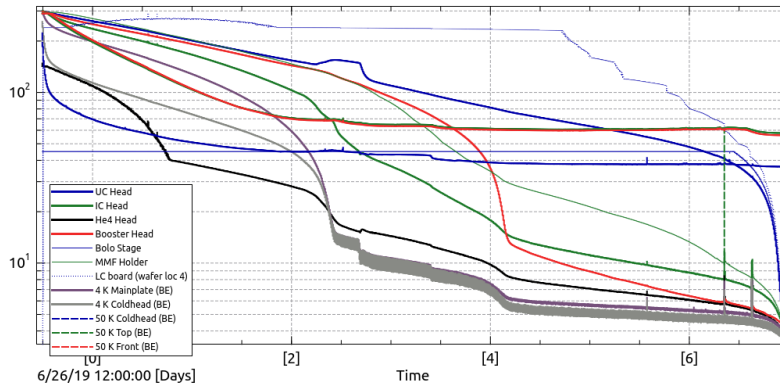
(a) Temperature curve of certain backend elements
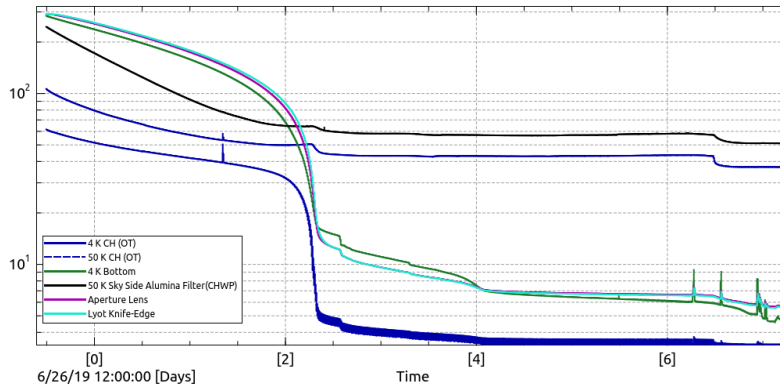
(b) Temperature of certain optics tube elements

Figure 2.5: *Top*: A plot of the cooldown curve of the main 4 K and 50 K elements of the PB-2b backend during the final in-lab integrated receiver run. *Bottom*: This figures shows the cooldown curve of the main 4 K and 50 K elements of the PB-2b optics tube during the same run.

from Chase Research Cryogenics[2] which are multi-stage adsorption fridges. They cool through evaporative cooling of ^{3}He and ^{4}He as the coldest temperatures achieved are lower than 2 K. Figure 2.6 shows a cartoon of one stage of a refrigerator. There are four basic parts: heat switch, pump, condenser, and evaporator. With the heat switch open, gas condenses into the evaporator creating a pool of liquefied helium in the evaporator. When the heat switch is closed, the pump cools down, drawing evaporated helium up from the evaporator, thereby cooling the evaporator. The evaporator is considered the "head" and is what the millikelvin heat straps attach to to cool the FPT. The fridge in PB-2b uses three successive stages of cooling (one of ^{4}He and two of ^{3}He) to achieve the detector temperature of 0.25 K in the expected 1.0 μW of thermal load on the focal plane.
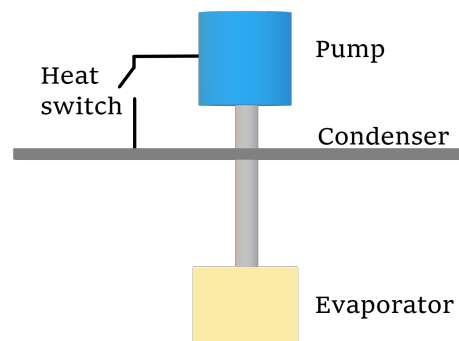
Figure 2.6: A cartoon of a single stage in the millikelvin refrigerator. There are four basic parts: heat switch, pump, condenser, and evaporator. With the heat switch open, gas condenses into the evaporator creating a pool of liquefied helium. When the heat switch is closed, the pump cools down, drawing evaporated helium up from the evaporator, thereby cooling whatever is attached to the evaporator.

2.3.3   Detectors and Cryogenic Readout

Polarbear-2 receivers utilize a digital frequency multiplexing (DfMux) scheme in order to read out thousands of detectors in a more efficient manner. Figure 2.7 shows a general schematic of the system. Starting from the warmest stages at room temperature, the iceboards and SQUID controller boards control the cryogenic readout and detectors. Both the iceboards and SQUID controller boards are designed and produced by McGill University. At 4 K live the SQUID cards which are connected to the multiplexing unit (LC boards) by niobium-titanium waveguides (striplines) and reside at sub-Kelvin temperatures. The LC boards are niobium chips with inductor-capacitor resonators, where each resonator couples with a detector (bolometer). A single LC chip has 40 resonators providing a multiplexing factor of 40.

This system operates by generating a single current in the iceboard comprised of different frequency tones and sending it to the LC chip. Each resonator selects out a specific tone. The resonator is connected in series to the detector so the tone is amplitude-modulated by the incoming signal from the detector. All the tones from a single multiplexing unit are then summed and sent to the signal amplifier (SQUID) before returning to the warm electronics.

The following two sections describe the cryogenic readout and detectors, and Chapter 4 discusses their validation results during the final in-lab integrated run.

Cryogenic Readout

The first cryogenic readout component described here is the SQUID which resides at the 4 K stage in the backend. We use arrays of DC SQUIDs as sensitive, low impedance ammeters to amplify our detector signal. Functionally, SQUIDs are magnetic flux to voltage transducers. A DC SQUID is a superconducting ring with two parallel Josephson junctions[3] as shown in Figure 2.8. When superconducting,

---

[3]A Josephson junction is a weak insulator sandwiched between two superconducting materials such that the phase of the current wavefunction on either side of the inductor are related.
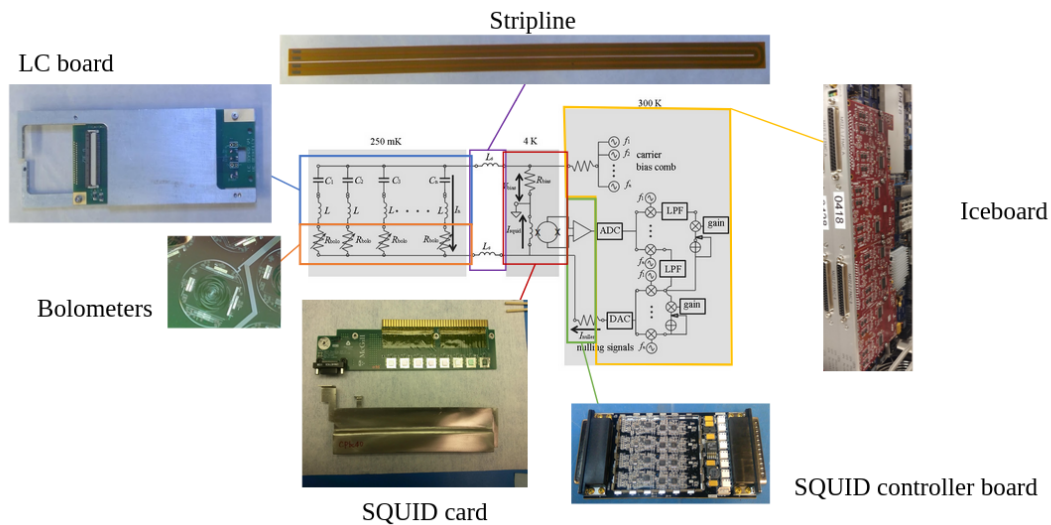
Figure 2.7: A diagram of the DfMux scheme. The center drawing is a circuit diagram of the system, and the photos surrounding it show what the physical components look like. The iceboard and SQUID controller board are room temperature electronics that control the cryogenic readout and detectors. The SQUID card is a signal amplifier connected to the LC board (multiplexing unit) via the stripline (waveguide). Each LC board has inductor-capacitor resonators where each resonator is connected to a bolometer (detector).

current flows freely through the ring with zero resistance unless the current exceeds the critical current, and voltage begins to build within the ring. The critical current of the Josephson junctions are lower than the critical current in the rest of the ring. Also, any magnetic flux through the ring is quantized due to the nature of the superconducting current. A single quantum of flux is $\Phi_0 = \frac{h}{2e}$ where h is the Planck constant, and e is the elementary charge. If there is a change in magnetic flux through the SQUID, the current in the SQUID changes so that the total magnetic flux through the SQUID is an integer multiple of the fundamental flux unit Φ_0.
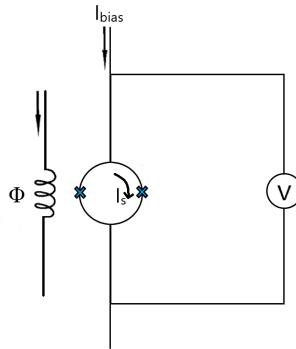
Figure 2.8: A circuit schematic of a DC SQUID. The SQUID itself is the loop with two x's which are the two Josephson junctions. There is a current bias with a high output impedance that flows current through the loop, creating a voltage across the loop. A change in current generated at the detector travels through to the input coil of the SQUID (on the left) and creates a change of magnetic flux through the SQUID which then changes the current out of the SQUID. This change of output current is what we measure.

In order to operate SQUIDs as magnetometers, a current bias is applied to the SQUID that is greater than the critical current of the Josephson junctions so that there is a measureable voltage across the SQUID. If a magnetic flux is applied to the

27

SQUID, a current is induced in the SQUID loop which produces a change in voltage. The relationship between the applied magnetic flux and the change in voltage for a given bias current is represented by a V-Φ curve as shown in Figure 2.9. In our SQUID arrays, the applied magnetic flux comes from the input coil which is an inductor that is coupled to the SQUID. We apply a current bias through the SQUID as well as a current through the input coil which we call a flux bias current. When there is no current coming from the detector, these biases keep the SQUID at a constant voltage and magnetic flux relationship.

We utilize a negative feedback configuration called digital active nulling (DAN) to null the current coming from the bolometer. If there is a difference between the nulling signal and the signal from the bolometer, this is amplified by the SQUID and DAN adjusts the nulling current so that it cancels out the signal from the bolometer. We measure the nulling current to determine the magnitude of the signal coming from the detectors.
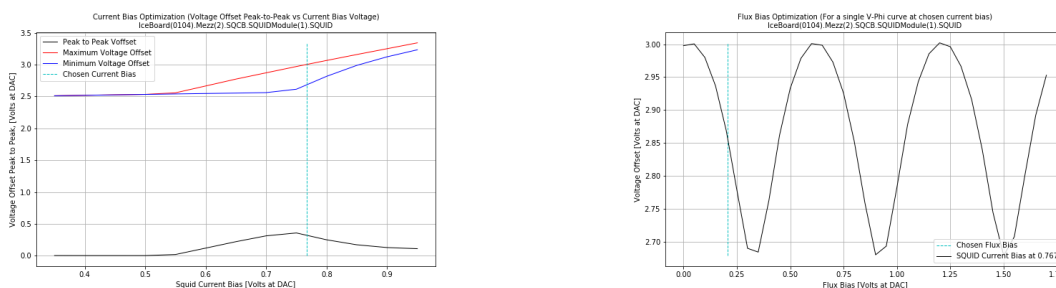
Figure 2.9: *Left*: An IV curve of a DC SQUID. The x-axis is the SQUID current bias, and the y-axis is the voltage across the SQUID. *Right*: A V-Phi curve where the x-axis is the flux bias, and the y-axis is the voltage across the SQUID. The blue line indicates the selected bias (tuning point) for the SQUID. These plots were generated by a software library called pydfmux [26] that is used to operate the SA readout system.

The second component in the cryogenic readout is the niobium LC resonator chips which physically are installed behind the detectors and are cooled to 250 mK.

The multiplexing factor in the DfMux scheme is defined by the number of inductor-capacitor resonators on the LC chip. In our design, there are forty resonators on each LC chip. The frequency spread on these LC chips is based on the range of possible output frequencies from the warm electronics and the amount of frequency spacing required to limit resonator cross-talk. For PB-2, the resonators are equidistant in frequency space on logarithmic scales from 1.6 Mhz to 4.6 Mhz. Figure 2.10 is an example of a network analysis which shows what frequency channels are available on a given LC chip.
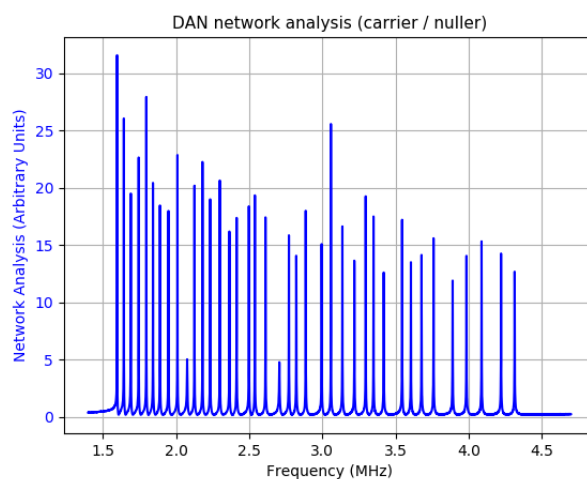
Figure 2.10: An example result of what is called a network analysis of an LC chip. Different frequencies are fed to the LC chip and each LC resonator picks out its specific frequency resulting in the peaks shown here. This plot was also generated by the pydfmux software [26] mentioned in Figure 2.9.

Detectors

The PB-2 focal planes each consist of seven detector modules installed into a structure called the FPT (see Figure 2.11). Each module has a detector wafer of 7,588 detectors or equivalently 271 pixels. The detectors we use are transition-edge sensor (TES) bolometers coupled to a sinuous antenna [39]. There are four

or six bolometers connected to each antenna where four are optical and two are dark for characterization. Frequency filters between the antenna and the optical bolometers define the spectral band that each bolometer measures. For PB-2a and PB-2b, the filters were designed to pass spectral bands centered at 90 GHz and 150 GHz as these are in two atmospheric transmission windows near the maximum emission frequency of the CMB. The third receiver, PB-2c, was designed for detecting higher frequencies in order to measure galactic foregrounds to subtract from our CMB science measurements.
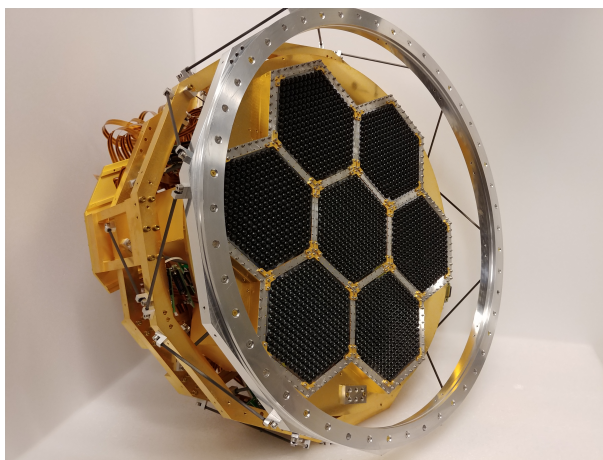
Figure 2.11: A photo of a fully populated FPT that was installed into PB-2b.

TES bolometers utilize the superconducting transition of its material so that it operates as a temperature-sensitive variable resistor (Figure 2.12). Our bolometers are made out of aluminum-manganese with a transition temperature of 450 mK. Therefore, to take advantage of this transition temperature, the detectors arrays are cooled to provide a thermal bath of 250 mK, and then the thermistors are self-heated to their superconducting transition temperature.

The bolometers (Figure 2.12) are voltage-biased to take advantage of a negative electrothermal feedback capability. As photons hit the bolometer and deposit power onto it, the temperature of the TES increases which could quickly drive the bolometer
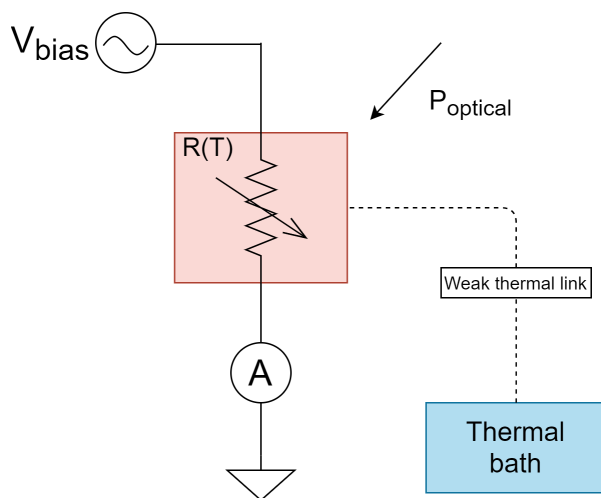
Figure 2.12: A cartoon drawing of a TES bolometer. The red boxed area is the detector itself symbolized as a temperature-variable resistor. It is weakly coupled to a thermal bath and is voltage-biased for operation. A photon ($P_{optical}$) hits the bolometer, increasing the temperature and thereby increasing its resistance which results in a measurable change in current.

normal. As photons hit the bolometer and the temperature increases, this also causes the resistance to increase (Figure 2.13). Since the TES is voltage biased, the voltage across the TES is constant, so according to the electrical power equation $P = V^2/R$, the power decreases as resistance increases which lowers the temperature of the bolometer. This negative feedback loop enables us to use these TES bolometers without driving them out of their superconducting transition.

Figure 2.13 is an example of a detector's resistance as a function of temperature. Starting from the right, at temperatures above the transition temperature of the bolometer, the bolometer is in its normal state and the resistance is designed to be 1.2 Ω based on requirements from our readout electronics [8]. As the temperature decreases to the left, we reach the transition temperature where the resistance dramatically drops. Once below the transition temperature, the bolometer is now superconducting with zero resistance. However, there is stray impedance due to

readout components that needs to be subtracted from the measured resistance. The stray impedance is the remaining impedance in the circuit when the bolometer is superconducting.
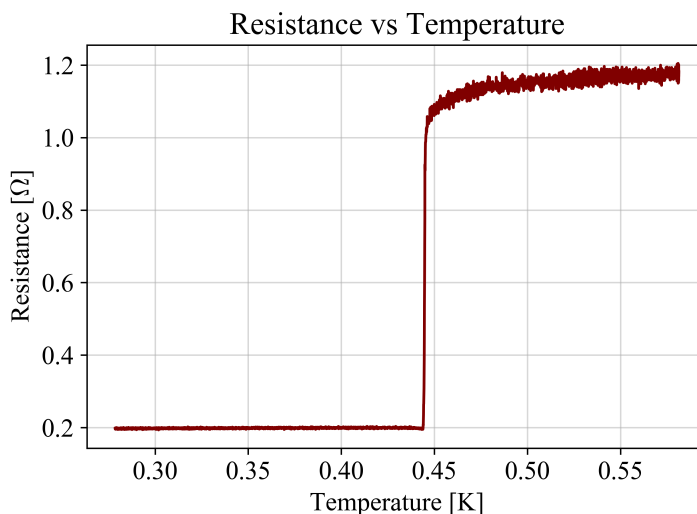
Figure 2.13: This figure shows the relationship between temperature and resistance of a PB-2b bolometer. The x-axis is temperature in Kelvin, and the y-axis is resistance in Ohms. The vertical line is the superconducting transition regime. The regime to the right is the normal state of the bolometer. The flat line to the left shows the bolometer in its superconducting stage. It is at a non-zero resistance due to parasitic resistances in the detector readout chain.

Figure 2.14 shows the current measured through the bolometer as a function of the voltage across the bolometer. Starting from the right, the bolometer is in its normal state, and as the voltage decreases to the left, the current also falls. The bottom of the curve, or the turnaround point, indicates the beginning of the superconducting transition. As the voltage continues to decrease, the current actually increases as the bolometer's resistance lowers. The jump indicates the bolometer fully transitioning into its superconducting state. The straight line on the left shows the stray impedance in the detector readout system. When corrected for stray impedances, this line will be vertical at zero describing the superconducting state of the bolometer.

32
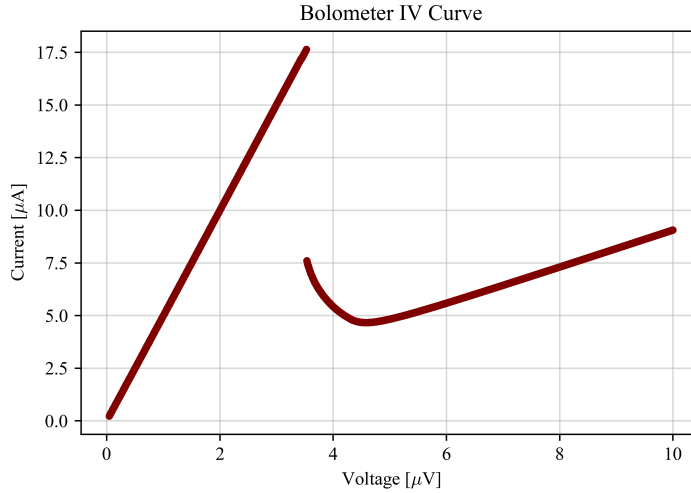
Figure 2.14: This figure shows an example of an IV curve of a single bolometer from PB-2b. The x-axis is voltage in microvolts and the y-axis is current in microcurrent.

Descriptions of how these measurements are performed is in Section 4.2.

2.4 Polarbear-2b Receiver-specific Elements

2.4.1 Cryogenic Half-wave Plate

In order to reduce low-frequency noise in the polarization measurement, a polarization modulator is used. In POLARBEAR-2a, a continuously rotating half-wave plate polarization modulator was successfully implemented external to the receiver at ambient temperature [35, 14]. However, in order to reduce thermal emission from the HWP, a cryogenic HWP (CHWP) was designed and developed for PB-2b that would sit inside the optics tube of the receiver in front of the three reimaging lenses [13]. The CHWP assembly consists of two main sections, the rotor and the stator where the rotor rotates during regular operations while the stator consists of elements that remain stationary. The CHWP is a stack of three sapphire plates sandwiched

33

between two alumina plates AR-coated with duroid-mullite [32]. This sapphire stack is mounted to a magnetic ring on the rotor while a ring of yttrium-barium-copper-oxide (YBCO) is part of the stator [13]. When temperatures drop below ~ 90 K, the YBCO superconducts levitating the HWP. During operation, the wave plate is able to continuously spin.

The CHWP was successfully integrated with the receiver and various tests were performed during the final in-lab run. The wave plate was successfully gripped and centered while warm and cryogenic. The CHWP was also spun and stopped safely. Additionally, it was determined that spinning the CHWP did not cause magnetic interference in the detectors. There also was no CHWP-induced heating on the focal plane [13].

2.4.2   Receiver Strut Redesign

The backend and optics tube sections of the receiver both utilize hollow G10 struts to create a support structure between aluminum shells of different thermal stages. The original design for both the backend and optics tube struts consist of a hollow G10 rod with end tabs that are inserted into the rod. The struts used in the backend aperture truss structure have G10 end tabs while the other struts have aluminum end tabs. A hole is drilled in either the rod or the end tab to allow the gas that would otherwise be conductive to escape from the strut.

In the backend, longer struts are used to support the backend shells within each other, while shorter struts are arranged into a truss-like structure at the aperture of the backend to support the interface between the backend and optics tube (see Figure 2.15). In the optics tube, these G10 struts are placed in an orientation to keep the nested cylindrical shells concentric (see Figure 2.16). A set of G10 struts exist at the aperture lens and at the field lens between the 4 K and 50 K shells and the 50 K and 300 K shells resulting in 4 sets of 8 struts.
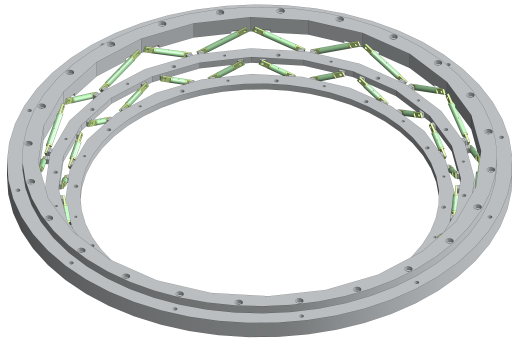
(a) SolidWorks drawing
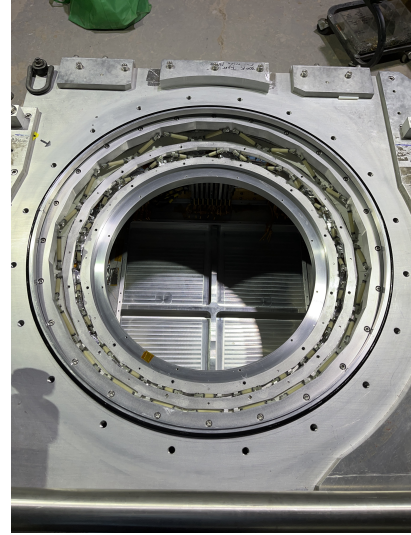
(b) Photo of the backend aperture

Figure 2.15: *Left*: This shows a drawing of the truss structure at the backend aperture. The lower, smaller diameter ring is the 4 Kelvin stage and is the interface between the 4 Kelvin taper shell and the FPT. The middle ring is the 50 Kelvin stage, and the outermost ring is the 300 Kelvin and vacuum shell. *Right*: This photo shows the backend aperture truss structure integrated into the front of the backend. The FPT mounts beneath it, and the optics tube sections stack on top. Photo courtesy of Lindsay Ng Lowry.
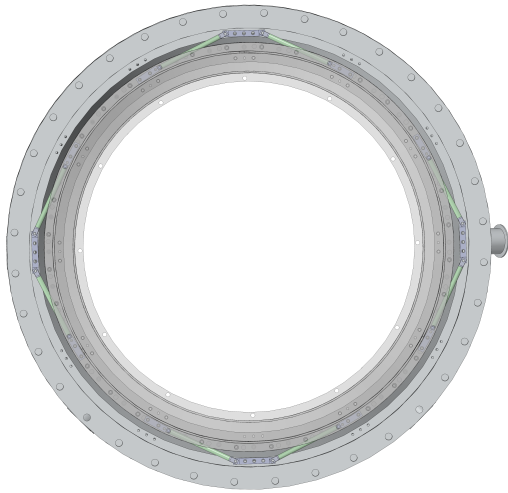
(a) SolidWorks drawing - top view   **(b)** Photo - side view
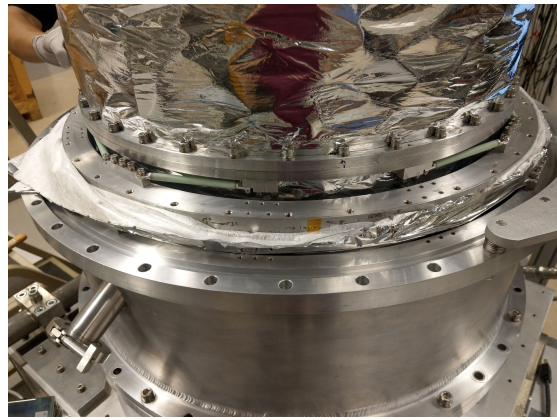
Figure 2.16: *Left*: The left drawing is a top view of the optics tube, looking down the boresight towards the detectors. This shows the G10 support struts that are between the 50 Kelvin and 300 Kelvin shells. The eight G10 struts are arranged in pairs equidistant around the shells. There are identical support structures between the 4 Kelvin and 50 Kelvin shells. *Right*: The right photo shows a side view of the 4 K to 50 K G10 strut structure at the aperture lens during an in-lab run. The G10 struts shown here are the original G10 struts.

Modifications were pursued for struts in backend and optics tube sections of the receiver, but only the optics tube G10 struts were deployed. The following sections describe the motivation for redesigning the struts, the actual modification, and the stress testing and results of the modified struts. The last section describes slight modifications that were made to the carbon fiber struts used in supporting different thermal stages in the FPT.

Redesign Motivation

In the backend aperture, it was discovered that 2 out of 24 struts had small cracks in their G10 tabs although the tabs were determined to be still structurally sound. In the optics tube, over time with multiple disassembly and reassembly of receiver, the epoxy holding the aluminum end tabs in the G10 rod would fail allowing the end tab to be easily pulled out of the G10 rod. A tension test (Section 2.4.2) was performed to check the strength the of solid but used optics tube G10 strut. The test setup and results are shown in Figure 2.20a and Figure 2.21a respectively.

Strut Redesigns and Assembly

For the backend aperture struts, it was decided to remake these with the same original G10 rod design but with aluminum end tabs to mitigate the cracking found in the G10 end tabs. For the remaining struts, the G10 rod design remained the same, but the end tabs were modified following the concept from Crowley et al.[6]. The tab for the backend (optics tube) is designed with one end that inserts into (covers over) the G10 rod and has a ribbed pattern (Figure 2.17). This ribbed pattern creates flow channels for the adhesive. Due to space constraints, we could not redesign the aluminum tab to fit over the G10 rod for the backend struts.

In assembling these rods, much care was taken in cleaning each component, and procedures were adapted from those described in Crowley et al.[6]. After being machined, the aluminum tabs were cleaned in an ultrasonic bath for minimally 30
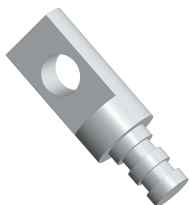
(a) Redesigned backend end tab
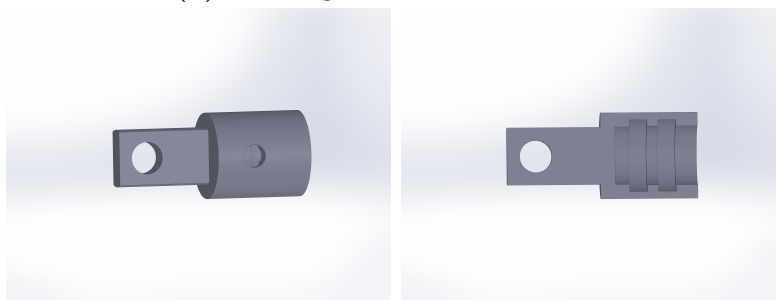
(b) Redesigned optics tube end tab

Figure 2.17: *Top*: A drawing of the redesigned aluminum end tab for the backend G10 support strut. The ribbed pattern inserts into the G10 rod. *Bottom*: These drawings show the redesigned aluminum end tab for the optics tube support struts. The left image highlights the epoxy injection hole, and the right image is a cross-sectional drawing to show the epoxy flow channels. The socket end fits over the G10 rod. Both of these designs are following the concept from Crowley et al.[6].

minutes with a mild detergent. The tabs were then rinsed in water and dried with air. Next, the end of each tab that inserts into (covers over) the G10 rod was abraded with a steel brush with isopropyl alcohol. This was intended to roughen the aluminum surface so that the epoxy would adhere to it better. Afterwards, the tab was rinsed thoroughly with isopropyl alcohol and dried with air. Finally, it was set to air dry for at least 10 minutes.

To prepare the G10 rods for assembly, the inner (outer) surface of the ends of each G10 rod was abraded with wet-dry sandpaper. This served a dual-purpose of abrading and cleaning the ends, removing any hydrophobic surface. A standard water-break test was performed to make sure that the ends were abraded properly. After that, the ends were rinsed with isopropyl alcohol and dried with air. The rod would then air dry for minimally 30 minutes.

Once both components were dry, they were assembled using 3M's grey 2216 epoxy to glue the aluminum end tabs to the G10 rod. The epoxy cartridge is mounted in an applicator with a mixing nozzle attached to it so that the epoxy parts are mixed appropriately as it is applied. The epoxy was applied in a way to prevent air gaps in the epoxy joint. For the backend struts, the epoxy was applied to the flow channels carefully ensuring that the whole channel was filled. Additional epoxy was applied to the bottom edge of the tab so that when it was inserted in the G10 rod, it would seal the interface. However, one also had to be careful to not inject too much epoxy such that it filled the whole G10 rod. The shorter G10 struts were short enough that it was very easy to insert too much epoxy. For the optics tube struts, there was an epoxy injection hole that was used for filling the cap with epoxy once it was on the end of the G10 rod. The cap was considered filled adequately when epoxy would overflow from the bottom of the end cap around the circumference of the rod.

After the epoxy was applied, the rods were minimally baked in an oven at 80 °C for 120 minutes. They cured on a specially machined frame so that the tabs would set planar (Figure 2.18). The tabs were not secured down in any way, and it was
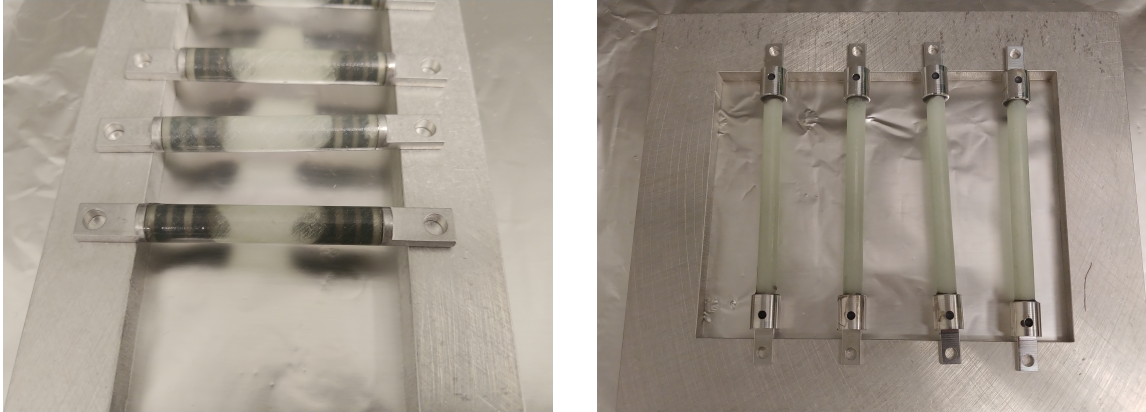
Figure 2.18: *Left*: This photo shows newly-made, longer backend aperture struts curing in their frame. *Right*: This photo shows newly-made OT struts curing in their frame. All struts shown here as examples were made from Type 1 G10 (Table 2.1)

found that it was not necessary as the rods maintained their shape before and after baking.

G10 Strut Strength Criteria

In order to estimate how much force these optics tube G10 struts needed to withstand, a simplified model was analyzed. The backend aperture was set as the pivot point for the optics tube which is assumed to be rigid. From the SolidWorks model, the mass was calculated for everything at the 4 Kelvin stage and separately for everything at the 50 Kelvin and 4 Kelvin stages. The mass of the 4 Kelvin stages would be used to calculate the strength required for the struts that support the 4 Kelvin shells against the 50 Kelvin shells, and the mass of the 4 Kelvin and 50 Kelvin stages combined would be used to calculate the strength required for the struts that support the 50 Kelvin shells against the 300 Kelvin shells. The center of mass locations for each was also calculated using the SolidWorks model.

Assuming the G10 struts act as a single force at each lens location counteracting the gravitation force on the optics tube (Figure 2.19), the summation of torques on
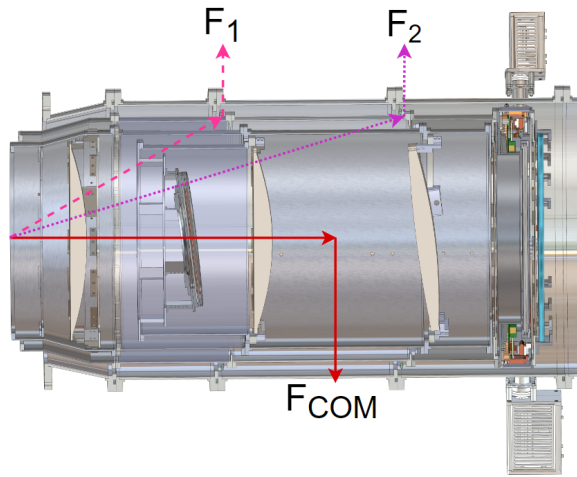
Figure 2.19: This diagram illustrates the three different forces that were considered to be relevant in calculating the torque on the backend aperture. The backend aperture is set as the pivot point, and the optics tube is considered rigid. The solid, red line is the torque from the gravitational force (F_{COM}) on the optics tube center of mass. The dashed, pink line is the consolidated force from the G10 struts at the aperture lens (F_1), and the dotted, purple line is the consolidated force from the G10 struts at the field lens (F_2).

the optics tube structure is set to equal zero. Equation 2.1 is the summation of torques.

$$\sum \tau_p = -R_{com} \times F_{com} + R_1 \times F_1 + R_2 \times F_2 = 0 \qquad (2.1)$$

In this equation, the subscript p refers to the pivot point. The first torque term is the rotation of the center of mass due to the gravitational force. The second and third terms are the opposing torques provided by the G10 struts. The two unknowns are F_1 and F_2 and are the forces at the two different locations R_1 and R_2. All the distance terms are found from the SolidWorks model.

In order to find a second independent equation, the relationship between F_1 and F_2 was defined. The upper bound for each G10 strut force was calculated by assuming that only one force (F_1 or F_2) supported the optics tube against the gravitational force (Equation 2.2). Next, the ratio of the results gave a relationship between F_1 and F_2.

Finally, Equation 2.1 was used to calculate the total force required at each location by the eight G10 struts. Since there were four distinct locations (two from each scenario), the result was a set of four forces. The largest of the four forces was divided by four to get the force required of each G10 strut. Since each G10 strut around the optics tube does not support the weight all in the same way, the force was not divided by eight. The result, with a safety factor of 1, is 388 N. The criteria for new suitable struts was to sustain a force 5 times greater than this, meaning a mechanical safety factor of 5.. This criteria is most likely a very conservative value given the support for the inner shells comes from being secured to the previous shell. These struts are intended to mitigate against any sagging of the sky-side flange of the shell.

$$\sum \tau_p = -R_{com} \times F_{com} + R_{1,2} \times F_{1,2} = 0$$
$$F_{1,2} = \frac{R_{com} \times F_{com}}{R_{1,2}} \tag{2.2}$$

Strut Testing and Results

In order to validate the strength of this new strut design, tension and shear tests were performed on new backend and optics tube struts. These tests were performed on an Instron 3367 machine that can sustain up to 30 kN of force. The bottom mounting plate was stationary while the top mounting plate moves only in the vertical direction.

For the tension tests, a pair of braces were designed that would hold the strut on each end with a stainless steel dowel pin (Figure 2.20a). The top jig moved upward and applied a force parallel with the strut. The vertical force applied was recorded by the computer software.

For the shear tests, a pair of jigs were made that would secure the strut on one end and press down on the end other (Figure 2.20b). There were two types of shear tests that were executed and designed to determine the flexibility and perpendicular force that these struts could endure. The first type (type 1) secured one end of the strut and pressed down on the free end. The secured end could rotate slightly before being constrained by the jig, so as the free end continued to be pressed down, the rod would flex. The value of the downward force was recorded.

A secondary shear test (type 2) was also designed using the same jigs from shear test type 1 (Figure 2.20c) and is considered an improved version of the first shear test since it more accurately represents how an optics tube strut might experience a shear force in the receiver. The strut was initially positioned horizontally and secured at both ends with screws. Both ends of the strut can rotate about the screw given enough force. The upper mounting plate moved upward, pulling the strut such

that it was being extended diagonally in parallel and perpendicular directions with respect to its axis. Since the force that was measured on the Instron is only the vertical component of the force, the force along the axis of the rod is larger than the force reported by the Instron software.

Three types of G10 rods were tested with various tension and shear tests. Table 2.1 summarizes the differences and overall decision for using each rod type. Type 1 material was from the same vendor as the original G10 struts, but during testing, this was found to be too weak for our application. Type 2 G10 rods were stronger since the rods had thicker walls, but since the walls were thicker, the concern was adding too much thermal loading to the optics tube. The final type[4], type 3, was determined to be appropriate for deployment from their tension and shear test results. The average test results are reported in Table 2.2. These average results are from the optics tube G10 struts since those were made in all three types of G10 material.

Table 2.1: This table summarizes the types of G10 rod material that were tested to find suitable material for deployment. The original vendor supplied type 1 G10 rods but these were discovered to be inadequate for deployment. A couple other G10 types were assembled and tested with various dimensions. The third type of G10 was determined to be deployable based on the tension test results (see Table 2.2).

G10 Rod Type	Outer Diameter [mm]	Inner Diameter [mm]	Deployed?
Type 1	8.00	7.00	No, material too weak
Type 2	7.94	4.76	No, rod wall too thick
Type 3	7.92	6.35	Yes!

Table 2.2 shows that the safety factor criteria of 5 was exceeded with G10 type 2 and type 3 struts for tension tests. Under tension, the failure mode for G10 struts made out of type 1 material was the G10 rod itself failing. The failure mode for type 2 and type 3 G10 struts was the aluminum end tab failing which occurred around

---

[4]This material was purchased through PlastiFab San Diego. They generally source material from two different vendors Accurate Plastics and Norplex. The material we received was from Accurate Plastics.
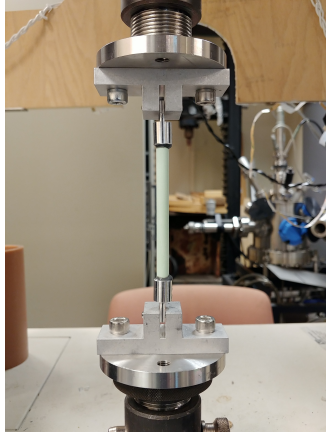
(a) Tension test setup
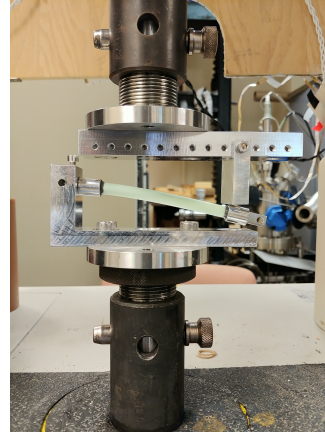
(b) Shear test type 1 setup
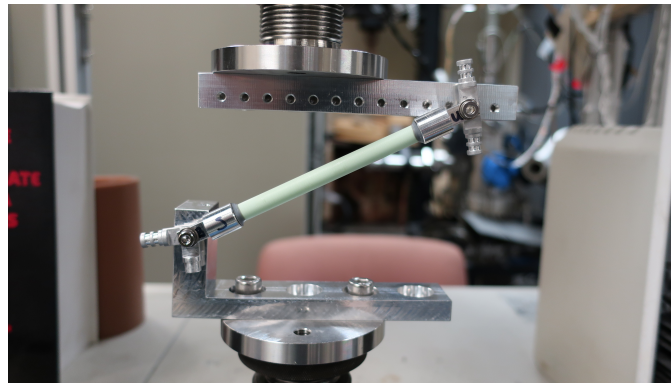
(c) Shear test type 2 setup

Figure 2.20: These photos show examples of the different testing setups. *Top left*: This is an example of the tension test setup. A steel dowel secures the rod in the top and bottom jigs. The top jig moves upward, applying tension along the strut which is recorded. *Top right*: This setup shows shear test type 1 where the right end of the strut is secured by a dowel pin through the end tab and a set screw on top. The strut can rotate downwards until jig tower blocks any further rotation. The top jig presses down on the free end of the strut, and the vertical component of the sustained force is recorded. *Bottom*: This photo shows the setup for shear test type 2. The same shear test jigs are used here as in shear test type 1, except the strut is now secured by screws on both ends. The screws are tightened as much as possible with an L-key, but the strut ends can still rotate about the screw given enough force. The vertical jig moves upwards creating a tension force along the rod, and the vertical force component is recorded.

the expected value of 3000 N [6]. With types 2 and 3, we improved upon the original struts.

Table 2.2: This table presents the average maximum vertical force recorded in both tension and shear tests from all OT G10 struts. The values are presented in Newtons, and the tension test includes the safety factor in brackets. The criteria is to sustain a tension force above a safety factor of 5, and this is the only requirement on the struts. The shear test results are informational only. The values are lower for the shear tests because only the vertical component of the force was recorded. Values with an asterisk indicate that only one strut was tested with this G10 type and configuration. The data from individual struts can be found in Appendix A

G10 Strut	Average Maximum Vertical Force [N]		
	Tension [SF]	Shear Type 1	Shear Type 2
Type 1	9.8×10^2 [2.5]	3.3×10^1	*3.2×10^2
Type 2	2.9×10^3 [7.6]	1.7×10^2	-
Type 3	2.8×10^3 [7.2]	*1.2×10^2	*1.0×10^3

One reason for lower force values is due to a limitation in the test setup. The tests were stopped because either the top and bottom jigs would collide or the strut was bent so far down, it would collide with the bottom jig. The other factor for the lower values this is that the Instron machine only measures the vertical component of force so the recorded value is only the amount of force use for pushing down on the strut end. None of the struts failed during these tests and survived such that tension tests could be performed on them afterwards.

Shear test type 2 provides the more interesting result. Shear test type 2 was performed only with G10 types 1 and 3 due to limitations of time and strut resources; however, we were able to compare the weakest G10 type with the one being considered for deployment in this configuration. The strut made of type 1 G10 ripped when the Instron measured a vertical force of 321 N. Based on the length of the rod and the vertical displacement when this failure happened, the force along the strut is calculated to be 990 N which gives a safety factor of approximately 2.5. The strut

made of G10 type 3 did not fail during the test. The test stopped due to the user-programmed extension stop limit. This stop limit was based on the failure point from testing the type 1 G10 strut. The recorded vertical force was 1038 N. The calculated force along the strut was 2249 N which gives a safety factor over 5. While the strut did not break, the force it sustained was enough to bend one of the screws holding it in place. Also, the aluminum tabs were beginning to deform. Taking into account all the results of the test, we were confident that the type 3 G10 struts were adequately strong for our purposes.

The fasteners which held the backend aperture struts in place were not accessible without extensive disassembly of the backend; therefore, the two backend aperture struts that were compromised were not replaced. It was determined that leaving those two struts did not compromise the structural stability of the backend aperture. The optics tube G10 struts were replaced during the 2022 assembly and successfully installed (Figure 2.22).

Carbon Fiber Strut Testing

Additionally, tension tests were performed on redesigned carbon fiber struts which support different thermal stages in the FPT. Those aluminum end tabs were also redesigned following the design in Crowley et al. [6]. The purpose of the redesign was also to increase the strength of the adhesion between the carbon fiber rod and the aluminum end tab.

The epoxy strength between the carbon fiber rod and aluminum end tab in the original strut was compared to the epoxy joint strength in a new strut. Two of each rod were tested under tension. The original carbon fiber strut failed at an average of 300 Newtons with the carbon fiber rod pulling out of the aluminum end tab. The newly modified strut failed at an average of 600 Newtons in the same way. Since the amount of force required to break the new rods was two times that of the original strut (which had already successfully been used in the PB2a experiment), it was

47

(a) Plot of tension vs extension

(b) Photo of a broken Al tab

Figure 2.21: *Left*: This plot shows the force vs extension on four different rods. The black curve shows the result of a tension test on an original G10 rod. There are two small dips towards the peak which corresponds to the epoxy audibly cracking before the end tab pulled out completely. The red curve shows the results on a deployed (type 3) G10 strut. The little dip around 2.5 m is when the rod began pulling out of the end cap. The gentle decline after the maximum force is due to the aluminum tab stretching before the aluminum tab finally breaks around 5.5 mm of extension (see Figure 2.21b). This length is more than 3.5 times that of the original G10 rod. The blue curve is the result of type 1 G10 which clearly withstood less force before failure of the G10 material. The green curve shows the result from a type 2 G10 strut which possibly could have worked for deployment as well, but there was concern about the thickness of the rod wall adding extra thermal loading. The failure mode for this strut is also that the aluminum end tab broke as shown in Figure 2.21b. *Right*: Photo of a broken aluminum tab which was the common failure mode for G10 struts made with type 2 and 3 G10 rods. The tab deformed, stretching under tension, until it reached its breaking point.

48

Figure 2.22: This photo shows the new OT struts installed between the 4 K and 50 K shells at the aperture lens.

determined that these modified carbon fiber struts were appropriate for use in the field since it was clear that this modified design and epoxy method enhanced the strength of the epoxy joint.

2.5 Acknowledgements

ley and Megan Russel at the University of California San Diego for their work in designing and assembling the G10 and carbon fiber struts.

Chapter 3

Polarbear-2b Receiver Assembly

Each receiver described in Chapter 2 required assembly for each in-lab test and for deployment at the site. This chapter will describe the work required for assembling the POLARBEAR-2b receiver for in-lab testing and deployment. Careful documentation of receiver assembly was developed and necessary for a successful field deployment. Since the receiver requires disassembly for safe transport to the site, detailed instructions were necessary for reassembling the receiver at the site. This was made even more critical as individuals with past assembly experience graduated and moved on from the project.

As the receiver can be separate into two main parts (see Figure 2.3), the assembly work can be divided into two components, the backend assembly and optics tube assembly. Section 3.1 describes the backend assembly which includes building the cryogenic readout and detector modules as well as populating and installing the focal plane tower (FPT). The optics tube assembly involves building up the optical chain and is outlined in Section 3.2. The third section, Section 3.3, describes the method for aligning the optical elements in the receiver which is necessary to achieve the designed optical performance. Proper lens alignment is vital for successful use of the instrument. Finally, the last section (Section 3.4) describes a receiver modification

that were performed in the time frame that the receiver was being deployed to the site.

3.1   Backend Assembly

Assembling the backend involves multiple components that build, assemble, or install the detectors and cryogenic readout and prepare the backend to be put under vacuum and cooled. The following subsections describe the cryogenic readout assembly and installation, the FPT assembly and installation, and the final steps to close the backend.

3.1.1   Cryogenic Readout Assembly

SQUID Card Assembly and Installation

One of the initial tasks in assembling the backend is installing populated SQUID cards. Their purpose and functionality are described in Section 2.3.3. The SQUID cards are printed circuit boards (PCBs) with eight locations to mount SQUIDs. Each SQUID card must have SQUIDs mounted onto them and connected electrically with aluminum wirebonds.

One of the challenges in working with SQUIDs is eliminating magnetic flux from being trapped in a SQUID loop [33]. Potential sources of external magnetic flux include the Earth's magnetic field and the magnetic fields generated from currents in the rest of the instrument [38]. Each SQUID is mounted on top of a small niobium foil which traps flux when superconducting. Additionally, the SQUIDs mounted on their PCB are covered with a cryoperm shield which is shown in the bottom half of Figure 3.1a [31].

Once the SQUID cards are assembled, they are inserted into a wiring harness in the top of the backend. There is a gold-plated copper braid that attaches to the
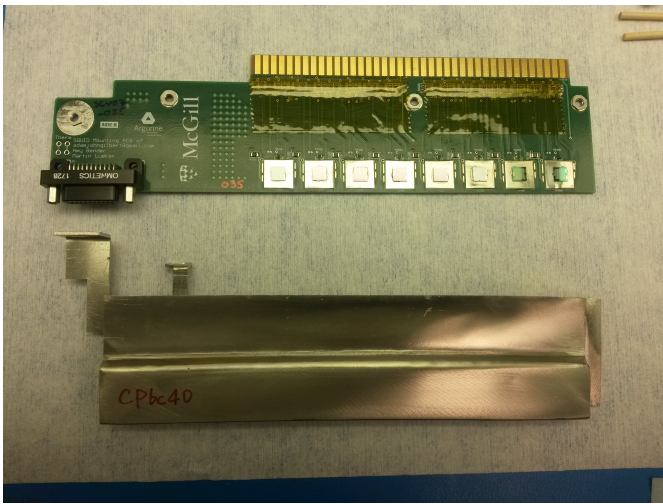
(a)   **(b)**

Figure 3.1: *Left*: A photo of a fully populated SQUID card with its cryoperm sleeve for magnetic shielding beneath it. The cryoperm sleeve slips over the SQUID card. *Right*: This photo is of the SQUID card installed in the backend with its heatstrap attached.

SQUID card on one end and the 4 K shell on the other end. It acts as an electrical grounding strap and a thermal conduit for cooling the SQUID card (Figure 3.1b).

Readout Quanta Assembly and Installation

At the sub-millikelvin stage sit the LC multiplexing readout. A single PCB called an adapter board has a micro D-Sub connector which plugs into the SQUID card on one side, and on the other side is connected to a group of LC chips through striplines. This unit consisting of the adapter board, striplines, and LC boards are called readout 'quanta'. There are both 'large' and 'small' quanta. If there are eight LC resonators chips, the quanta is designated as 'large', and if there are six resonator chips, the quanta is designated as 'small'. Functionally, for a large (small) quanta, one adapter board PCB and four (three) pairs of striplines connect eight (six) LC resonator chips to a single SQUID card with eight (six) SQUIDs. The assembly method of these readout quanta and how these quanta are installed onto the detector wafer are described in [10].
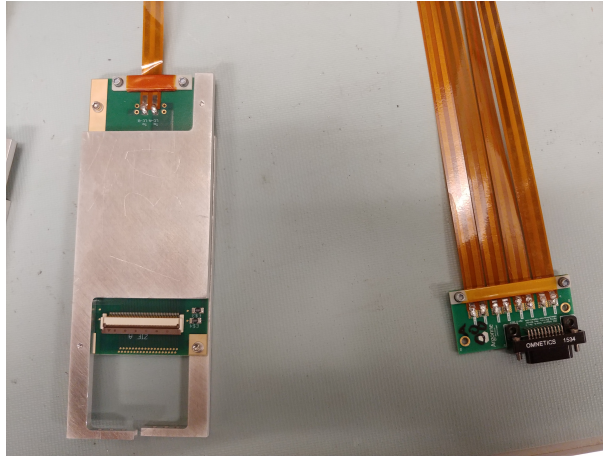
Figure 3.2: A photo of one of the LC boards as part of a large quanta. The adapter board (on the right) is connected to a total of 4 LC boards where each board houses 2 LC chips. A small quanta, in contrast, is an adapter board connected to 3 LC boards.

3.1.2 Focal Plane Tower Assembly

The focal plane consists of seven detector modules. Each detector module requires assembly (Figure 3.3) before it can be installed into the FPT. The following subsections describe the FPT assembly process once the detector modules are built.
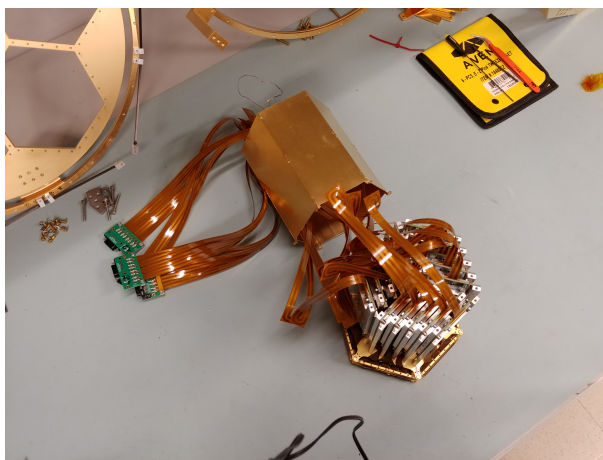
Figure 3.3: Photo of a detector module assembled with its cover removed. The detectors are face-down on the table. The LC readout quanta are mounted to a plate that covers the backside of the detectors. When completely assembled, the golden can fits around the standing LC boards.

Detector Module Installation

After the detector modules are assembled, they are installed into the FPT. This is done in a specific order for the sake of ease and so that flex cables on the edges of the detector wafer do not have to be excessively manipulated. During the process of installation, it is best to have only at most two wafers on either side of the module that is currently being installed. This way, when installing the detector module, it can be inserted at an angle such that the tabs on the wafer's mechanical mount can interlock easily without having to excessively press on the flex cables. Kapton tape was also used to press the flex cables close to the detector module which aided in

protecting the flex cables and provided more space around the edge of the module during installation.

When installing a detector module, it is important to adjust the position[1] of the module so that the screws that secure the module can be inserted smoothly. This ensures that the detector module is properly positioned on the focal plane and that all the modules can easily fit. There are also interlocking tabs on the wafer's mechanical holder that must be carefully interlocked together with the other detector modules as each detector module is installed (Figure 3.4b).

(a)   (b)
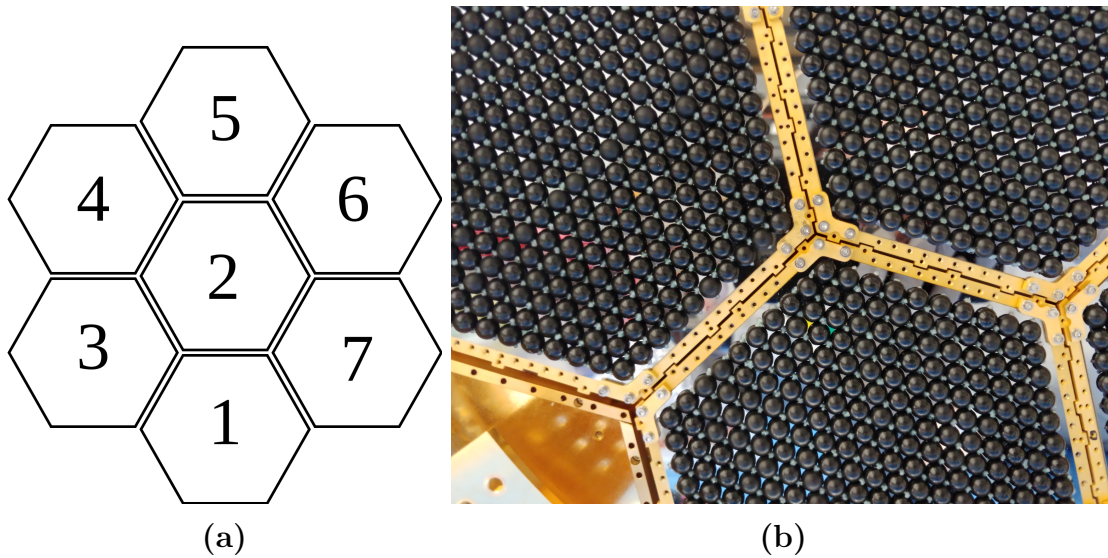
Figure 3.4: *Left*: A close-up view of the interlocking tabs between the detector modules. This does not show the RF shield that is eventually placed between the detector modules. *Right*: This drawing illustrates the order of installation for each detector module. This is the FPT as viewed from the front. The intent is that each detector module being installed only has at most two detector modules already installed next to it. The final detector module necessarily has three neighboring modules. However, if the other modules have been properly positioned, installing the last module is not particularly harder.

---

[1]The detector module can be shifted around slightly due to the space in the screw clearance holes.

Figure 3.4a illustrates the order of installation. If the receiver is pointed at horizon, the FPT can be split into three vertical columns where two detector modules are in the left and right columns and three detector modules are in the middle column. The bottom detector module in the middle column is installed first and then the one above it which is the center detector module. Next, the remaining detector modules are installed in a clockwise pattern starting with the module in the bottom of the left column. For the first six detector modules, there are at most two adjacent detector modules. The final detector module has three adjacent modules which makes it the most difficult module to install. However, with the taped flex cables and being careful about properly installing the adjacent modules, this final module is easily installed without any extra manipulation.

Stripline Heatsinking

Every single stripline is secured to two heatsinks on the back of the FPT. Each heatsink is a grill-like rack with flat bars. One heatsink thermalizes the striplines to 350 mK, and the second heatsink thermalizes the striplines to 1 K. This allows heat to be removed at each temperature stage.

A single clamp secures three or four striplines to the heatsink rack. To ensure efficient cooling, the striplines must be well-attached to the heatsink. As the clamp is tightened on both ends, the center of the clamp might pucker just enough such that the striplines at the center are no longer clamped well. To prevent this, layers of kapton tape were placed on the clamp in a stepped function with more layers of tape at the center and less layers at the edges. To check that they were clamped down hard enough, we attempted to shift each stripline after clamping. If they did not move, they were secured adequately. If they did move, extra kapton tape was added. Clamping the striplines to these heatsinks is delicate work as the striplines are fragile and must be maneuvered in awkward positions.
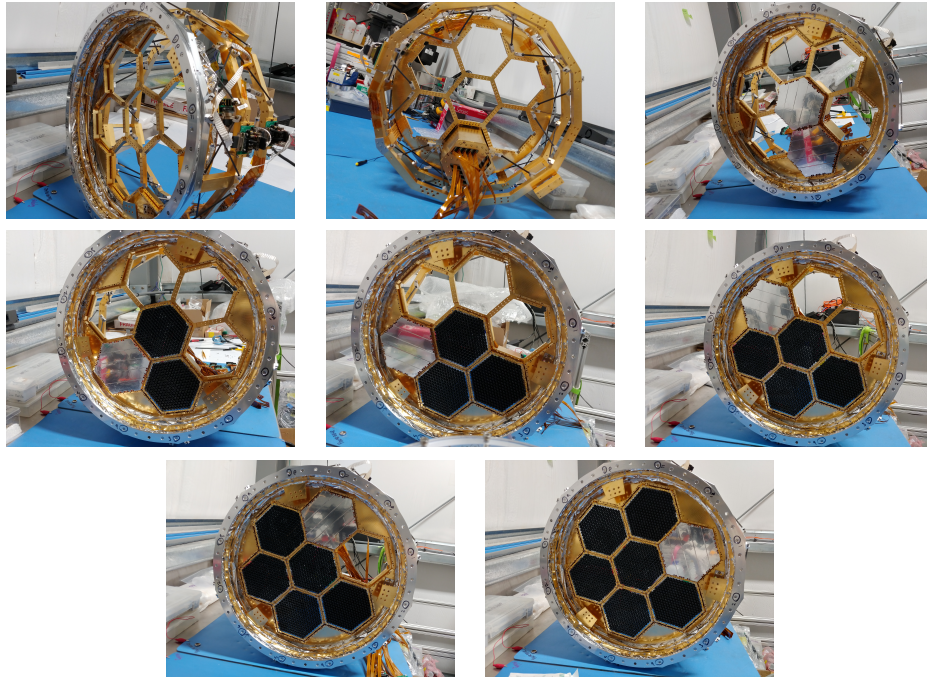
Figure 3.5: This is a series of photos that show the gradual population of the FPT. It begins at the top left and ends at the bottom right and progress from left to right, top to bottom. Each new wafer is installed with a cover to protect the lenslets. The cover is seen in these photos with very reflective tape on it.

Figure 3.6: *Top left*: This photo shows the FPT facing down onto the table with all the striplines before they are heatsunk. *Top right*: This photo shows the striplines after being heatsunk to both the 1 K and the 350 mK heatsinks. *Bottom*: This photo is a close-up that shows how the striplines are clamped to the heatsink rack.

3.1.3 Focal Plane Tower Installation

Once the FPT is ready to be installed into the receiver, the FPT is mounted onto a hand-crank lifting apparatus. Using this, the FPT is carefully inserted into the 4 K cavity and mounted to the backend aperture (the interface between the backend and optics tube). Shoulder screws are used for stability and strength. The shoulder on the screw requires the screw to be inserted parallel to the clearance hole as the shoulder removes any space allowing the screw to be inserted at an angle. Therefore, the process of mounting the FPT can be arduous. Since the lifting apparatus sags under the weight of the FPT, rotating the receiver so that the backend aperture plane is parallel with the FPT face is difficult especially since the backend cannot be rotated in small enough amounts at times.

After the FPT has been successfully mounted inside the backend, the adapter boards are plugged into the SQUID cards that are already installed in the backend. A gold-plated copper piece is attached to the adapter board. This serves as a heatsink and a grounding conduit. After the heatsink is attached, the adapter board is connected to the SQUID card by a micro D-Sub connector. As the boards are plugged in, the connections are carefully documented[2] for future reference of what detectors are connected to what SQUIDs. Once all the adapter boards are connected, the striplines are tied and taped down so that they do not thermally short to the 4 K backend shell and cause excess loading on the millikelvin stages.

Finally, heatstraps are attached to the FPT at three locations, each at a different temperature stage. These heatstraps are gold-plated copper foils that cool the FPT to 1 K, 350 mK, or 250 mK based on the fridge to which they are attached. Nitric acid is used to clean the copper oxide from the fridge coldhead to maximize thermal conductivity of the interface, and the heatstrap attachment is cleaned with isopropyl alcohol. On the FPT side, the rings to which the heatstraps attach are gold-plated to

---

[2]This is necessary in making a hardware map that allows communication to the detectors through its specific readout chain.
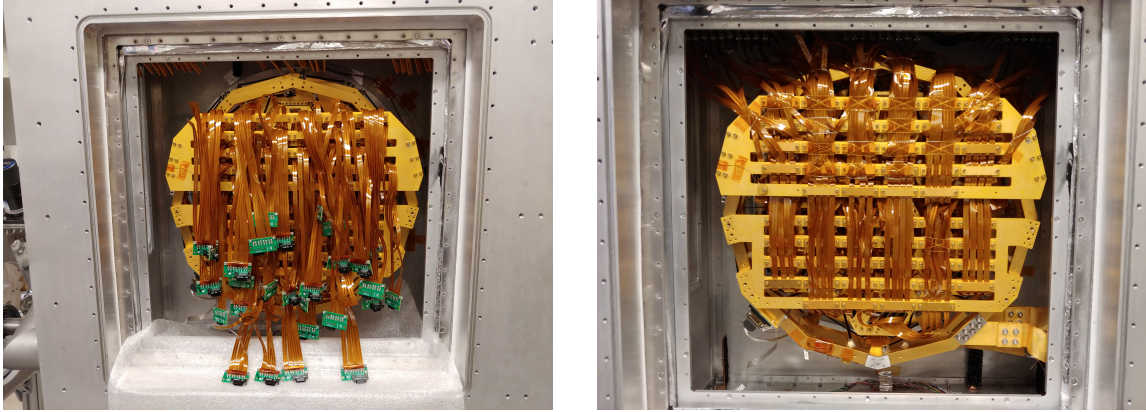
Figure 3.7: *Left*: This photo shows the back of the FPT just after mounting it into the backend. *Right*: This photo shows the finished state of the back of the FPT after connecting the adapter boards to their respective SQUID cards and tying down the striplines so that they do not excessively thermally short to the 4 K backend shell.

prevent oxidation of the structure, and the surfaces are also cleaned with isoporpyl alcohol before the heatstrap is attached. Once the heatstraps are connected on both sides, the foils are tied in place so that they do not thermally short to each other or the 4 K backend shell and cause excess loading. Finally, a D-Sub cable is connected to the FPT to read out the thermometers on critical stages of the tower.

3.1.4 Close-up

Before closing the backend, a final check of thermometry is performed, and charcoal getters are also installed to aid in the cooling process.

The last task involves installing aluminum panels on three of the four sides of the backend. Each side requires alternating layers of an aluminum panel and an MLI blanket. These blankets patch the gap in the existing MLI that separates each successive thermal shell. After the 4 K and 50 K panels and MLI blankets are in place, the final panels are vacuum panels that seal the backend. Once these are installed, the backend assembly is considered complete.

3.2   Optics Tube Assembly

The optics tube is assembled by stacking concentric aluminum cylindrical shells. There are three sets of shells that are nested within each other where each set is at a different temperature stage. The innermost shells are cooled to 4 K, the middle shells to 50 K, and the outermost shells are at room temperature (300 K) and provide the vacuum chamber structure. The 4 K shells are lined on the inside with an absorptive foam to reduce reflections. The 4 K and 50 K shells are each wrapped on the outside with MLI to insulate them and reduce thermal loading on successively cooler stages. As each shell is installed, N-grease is applied to facilitate thermal conduction between the shell being currently installed and the previous shell. This is only relevant for 4 K and 50 K interfaces.

The first optics tube shells to be installed are diameter-increasing shells called taper shells. This adapts the smaller diameter of the FPT to the larger diameter that accommodates the diameter of the lenses. The taper shells are the only set of shells where the order of shells installed goes from warmest to coldest. This is required due to the tapered shape of the shells. Once the 4 Kelvin shell is installed, the collimator lens is mounted in it. The lens is attached by four mounting blocks spaced equidistant around the lens. There are 12 6N aluminum heatstraps that are the thermal conduit for cooling the lens. These are placed in groups of three in between each mounting block.

After the collimator lens is in place, a sheet of aluminized mylar is stretched across the aperture. It is a single piece that is secured to the 4 K, 50 K, and vacuum shell flanges. This seals the backend and protects the SQUIDs from radio frequency interference. A narrow ring at 300 K secures the RF shield in place so that the next set of shells can be installed. This next set, labeled as the lyot shells, must be mounted with extreme care as the detector-side flange clamps the RF shield to the previous shell section. Shifting the shells after setting them down on the receiver
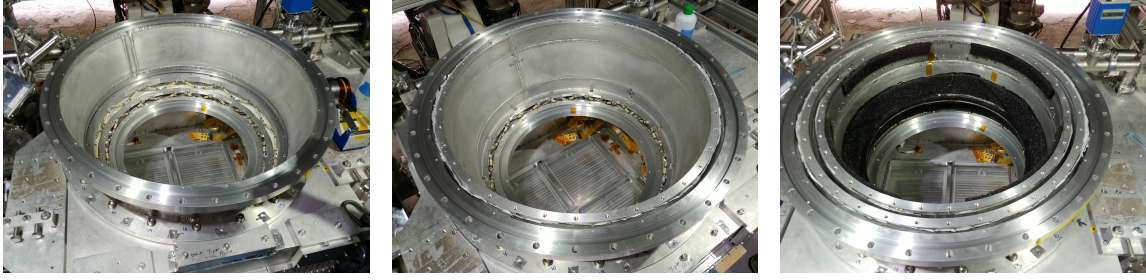
Figure 3.8: This shows the stacking of the taper shells onto the optics tube. The left most photo shows the 300 K or vacuum shell. The 50 K shell is added in the middle photo, and the 4 K shell is installed in the right photo. The collimator lens (not shown) would be installed into the 4 K shell next.

could rip the RF shield such that it no longer seals off the backend, rendering it useless.

Next, the aperture lens with the lyot tower are assembled as a unit on the ground and then installed into the receiver. The aperture lens is secured by four equidistant mounting blocks to an aluminum ring that is then mounted into a 4 K shell. There are 12 6N heatstraps attached between the lens and its mounting ring to conduct heat away from the lens. The lyot tower consists of a stepped structure with the lyot stop at the top and two metal mesh filters. One filter is teflon coated while the other one is not. When assembling the unit and installing it into the receiver, the orientation is important as the lyot aperture must be tilted in the proper direction to create a circular image on the primary mirror. Once the lens and lyot tower are attached to the same 4 K shell and installed onto the receiver, the remaining 50 K and 300 K shells are mounted.

The field lens is the final 4 K lens. Like the aperture lens, the field lens is secured to an aluminum ring by four equidistant mounting blocks with heatstraps. However, this lens is attached at an angle with respect to its ring at a similar angle and for the same reason as the lyot stop.

Since the second PTC's heatstraps attach to the 4 K and 50 K field lens shell

sections, those connection surfaces are cleaned and polished if necessary to facilitate thermal conduction. This is done while the shells are not installed on the receiver for convenience. Finally, the field lens is installed into the 4 K shell, and the 4 K, 50 K, and 300 K shells are mounted onto the receiver.

At this point, the second PTC is mounted onto the optics tube. It is mounted so that it will always be orientated at the same angle as the backend PTC. There are two heatstraps attached, one at the 50 K stage and one at the 4 K stage. These heatstraps are a combination of copper and 6N aluminum and wrapped in MLI after installation to prevent excess thermal loading and thermal shorts between stages.

The next major component is the polarization modulator assembly is mounted on the receiver. Bench-top tests are performed first to ensure that all the electronics associated with the assembly are in working order. Once these tests are successful, the assembly which includes the wave plate mounted to the rotor is secured onto the 50 K field lens shell.

An alumina filter is subsequently installed at the 50 Kelvin stage to block infrared radiation entering the receiver. Layers of radio transmissive multi-layer insulation (RT-MLI) is secured in front of it [5]. Finally, the window is installed. The window is made from ultra-high molecular weight polyethelyne and mounted in an aluminum fixture that caps the optics tube and seals it so that it can be put under vacuum.

Throughout this assembly process, thermometers were placed to monitor the temperature of critical elements in the cryogenic and optical design. The final step in completing optics tube assembly is to check that the thermometers can be readout by the warm electronics. Once this check is successful, the optics tube assembly is complete.

3.3　Receiver Optical Alignment

In order to achieve the designed optical performance, the lenses must be properly aligned so that the incoming beam is focused onto the focal plane. This is accomplished by iteratively measuring and adjusting the lens positions with respect to the detector plane during assembly. This alignment procedure was refined in the field and is described in this section. Additionally, measurements were taken so that the lens positions can be referenced to the outside of the receiver. This will be used for aligning the receiver with the telescope, which has not yet been completed at the time of this writing.

A model was constructed to produce the necessary lateral position and lens tilt tolerances when looking at photons at 280 GHz (see Table 3.1 for values). Since PB-2b measures signals in the spectral bands centered at 90 and 150 GHz, the tolerances were doubled as a conservative estimate for tolerances at these lower frequencies. These conservative tolerances were achieved with an acceptable margin of error.
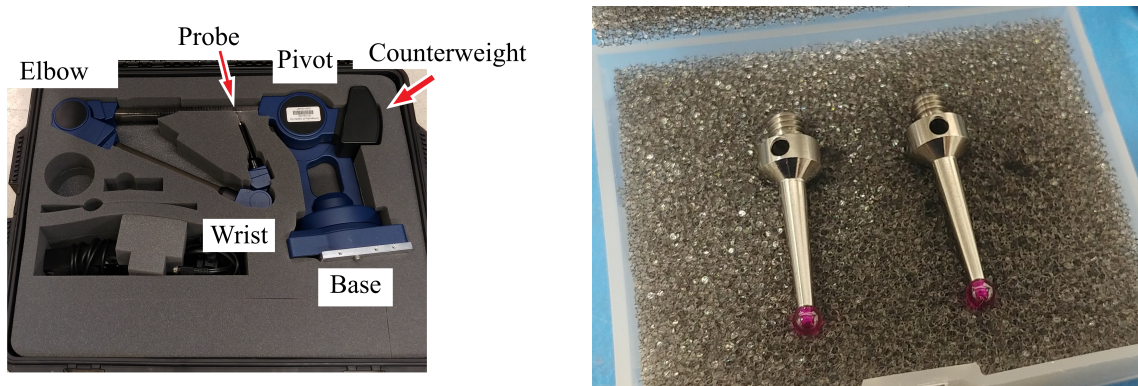
Figure 3.9: *Left*: This photo shows Microscribe instrument with key structures highlighted. *Right*: This photo shows two Microscribe probe tips. The tips are 3 mm diameter spheres.

The instrument we use to take measurements is the Microscribe MLX (see Figure 3.9). It is a portable instrument that consists of a swivel base and a double jointed

arm. The probe tip can rotate a full 360 degrees and is a 3 mm diameter sphere. The software used with this instrument is the MScribeUtility software. This is a small graphic user interface that can show the current coordinate position of the probe tip. This software also interfaces with other applications such as Microsoft Excel and Notepad for conveniently recording data.

The optical assembly of the three cryogenic re-imaging lenses is aligned as a unit. That unit's placement with respect to the focal plane is set by machining and assembly tolerances, which are precise enough to be within the tolerance of the optical design. As we build up the optics tube, we install each subsequent 300 K vacuum shell to be aligned with the previous 300 K vacuum shell. These 300 K shells are aligned to acceptable precision based on external inspections of the shells. Then, we reference the 300 K vacuum shell to the lens that resides within it. Using the relative position of the lens to its 300 K vacuum shell and our receiver model, we can determine the optical path alignment.

While each lens is measured in a similar manner, there are a few different things that are focused on depending on the lens. For the collimator lens, it is important to verify the distance between the lens and the focal plane and check that it is centered properly. For the aperture lens, it is important to check only the lateral position of the lens. If any adjustments are necessary to the lateral position, the most efficient method is to shift the 4 Kelvin shell that the lens resides in with respect to its 50 Kelvin shell. There is enough space in the clearance holes that mount the 4 K shell to move the lens on tens of a millimeter length scales. For the field lens, the lateral position of the lens and the degree of tilt must be measured.

To check the tilt of the field lens, we measure it first on the bench-top. The lens is mounted at an angle to an aluminum ring which allows us to measure the lens tilt before installing it into the receiver. Once the angle is correct, the field lens installation can continue.

We take measurement sets where each set consists of at least three data points

(a) Microscribe mounted on a table   (b) Example measurement locations
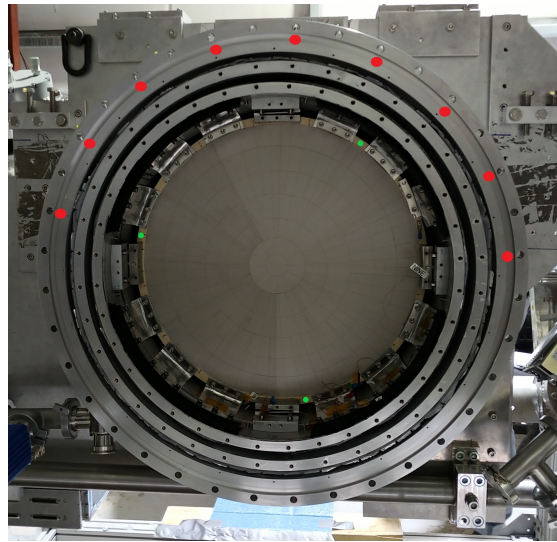
Figure 3.10: *Left*: This is an example of how the Microscribe was mounted to a table in front of the optics tube for taking measurements. The Microscribe base is attached to the table from underneath with a single screw which was enough to keep the Microscribe stable. *Right*: This photo is an example of measuring locations on the lens and 300 K shell. The green dots are for the lens flange, and the red dots are on the 300 K vacuum shell flange.

equidistant around the lens and at least six data points that span at least halfway around the sky-most vacuum shell flange as shown in Figure 3.10b. The analysis code generates a circle from each data set in three-dimensional space, determines the center of each circle, and takes the difference of their centers. This difference is what we compare with our required tolerances.

Table 3.1: This table outlines the design tolerances in the horizontal and vertical position of lens as well as its tilt. These quoted targets were developed from an optical model considering 280 GHz signals. For our purposes, we doubled these tolerances as the signals for PB-2b are 90/150 GHz.

Lens	Lateral Tolerance [mm]	Angular Tolerance [deg]
Collimator	± 5	± 0.25
Aperture	± 1	± 0.2
Field	± 1	± 0.5

A minimum of three sets are recorded for each lens. The difference between the lens center and the shell center is calculated for each set. The final result is recorded as the average and standard deviation of the differences from each set. An average of multiple measurements was determined to be a more robust determination of lens offsets than the original procedure of measuring positions just once.

Table 3.2: This table shows the actual alignment results that we achieved in the 2022 deployment. The lateral measurements are all from measuring the lens with respect to its 300 K shell. The results for the field lens angle is from measuring the lens installed on the receiver and not the bench-top measurements. The designed angle is 7°.

Lens	# of Sets Taken	Difference in X [mm]	Difference in Y [mm]	Lens Tilt [deg]
Collimator	3	0.96 ± 0.70	0.05 ± 0.94	0.13 ± 0.04
Aperture	5	0.78 ± 0.27	0.10 ± 0.20	0.19 ± 0.20
Field	4	0.96 ± 0.18	1.41 ± 0.05	6.902 ± 0.003

There are a few different factors that contribute to measurement error; however, Table 3.2 shows that we still achieved adequate lateral differences and angles. The

first factor is that while the individual taking the measurement strives to take each data point consistently, it is not possible to take each data point perfectly consistently. For example, the probe may be at a tiny different angle that is not noticeable to the naked eye especially since tenths of millimeters of precision is being measured. In order to quantify this error, multiple measurements were taken of the probe at different angles in the lens flange divot while making sure that the probe was fully in the divot. The standard deviation of the 13 data points was on average 0.1 mm in each dimension. Multiple data points were also taken in an effort to capture possible inconsistencies in measuring the shell flange. The standard deviation of 22 data points was at most 1.1 mm in the z-direction. However, it was 0.04 mm in the other two dimensions.

The second factor is the error in the Microscribe itself. The Microscribe MLX is designed to have an accuracy of less than 0.08 mm. To experimentally determine the tolerance of the probe itself, multiple measurements were taken while spinning a brand new probe in its home position. The standard deviation of 18 data points was on average 0.01 mm in each dimension.

The final source of error regards the stability of the instrument itself. The Microscribe needs to be setup on a stable surface for consistent measurements. This is usually achieved by screwing or taping the base of the Microscribe down to the surface. One must also be careful to not bump the structure supporting the Microscribe.

3.4   Collimator Lens Mounting Scheme

The original assembly design required that the collimator lens be installed into its 4 K taper shell before the shell was installed onto the receiver since access to the outside of the shell was necessary to install the collimator lens. The outside of the shell is only accessible when the shell is not installed in the receiver. Additionally,
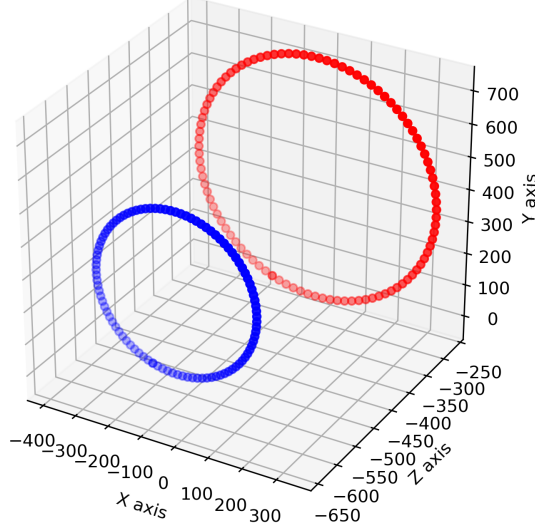
Figure 3.11: This plot shows the positions of the aperture lens (blue points) with respect to the sky-side (SS) flange of its 300 K shell (red points). This can aid in visualizing which direction the lens needs to be adjusted. The z-value decreases towards the focal plane. The x-y-z coordinate system origin is the base of the Microscribe. Thanks to Calvin Tsai for the plotting code.

it was required that this 4 K taper shell including the collimator lens be installed before the FPT. Because the 4 K taper shell is attached to the backend aperture at an interface between the collimator lens and the FPT, only one or the other can be present during installation. Therefore, with the colllimator lens installed, the only way to access that interface is by crawling into the backend space where the FPT mounts and attaching the 4 Kelvin taper shell from underneath the collimator lens. With the FPT is installed, this is not possible.

During the 2021 deployment, manufacturing delays prevented us from having the anti-reflection coated collimator lens ready to be installed before the FPT could be installed. Therefore, we decided to make modifications to the collimator lens mounting procedure. These modifications would allow the 4 K taper shell to be installed without the collimator lens, granting access to the mounting flange on the

shell even after the FPT is installed. Once the 4 K taper shell was installed on the backend, the collimator lens could then be lowered into it and secured. The collimator lens is attached to its shell by four mounting blocks spaced equidistant around the shell.

The first modification involved redesigning the lens mounting blocks (see Figure 3.12). These lens mounting blocks attach to the lens flange on one side and to the shell on the other side. Originally, one had to insert the screws from the outside of the shell through a washer plate into tapped holes in the mounting blocks. The washer plates were changed into nut plates, and the tapped holes in the mounting blocks were turned into clearance holes. This reversed the direction for inserting the screws which meant that we no longer had to insert screws from the outside of the shell. Additionally, since the new nut plates were bolted to the shell, they were stationary and did not require us to access the outside of the shell to hold them in place. The lens mounting blocks and nut plates were newly machined for deployment.

In order to address the second reason that required access to the outside of the shell, it was necessary to devise a method for attaching the heatstrap nut plates to the outside of the shell so that they would stay in place while we inserted the screws. The goal was to use existing nut plates without modification and simply develop a way to adhere them to the outside of the 4 K taper shell. The nut plates were secured using aluminum tape which held the nut plates well. Since these nut plates are not weight-bearing, they needed to remain in place, but did not need to be robustly attached to the shell.

3.5 Acknowledgements

Figure 3.12: *Left*: This drawing highlights in blue the mounting blocks that are used to mount the lens in its 4 Kelvin taper shell. The lens is colored in an earthen tone for contrast. The upper half of the mounting blocks that has four screw holes is what was modified. Originally, the screws were inserted from the outside-in radially. The blocks were modified so that the screws could be inserted from the inside-out. The 50 Kelvin and 300 Kelvin stage shells are transparent to emphasize the 4 Kelvin stage. The FPT (not shown) sits at the aperture at the bottom of this drawing. *Right*: This is cross-section view of the upper half (blue block) of the collimator lens mounting block. The four holes in this block are the holes that were changed from tapped holes into clearance holes. There are four corresponding holes on the red piece that were changed from clearance holes to tapped holes. Hence, the red piece is the new nut plate. The two holes on the outer edge of the plate are used to secure it to the 4 Kelvin taper shell. The other holes in the shell seen in these drawings are for the heatstraps.

Figure 3.13: This photo shows the nut plates for the heatstraps taped with aluminum tape to the outside of the 4 K taper shell. This was strong enough to solidly hold the nut plates in place. Photo courtesy of Lindsay Ng Lowry.

The dissertation author would like to acknowledge and thank Tucker Elleflot, Logan Howe, Lindsay Ng Lowry, Praween Siritinasak, and Calvin Tsai for their contributions to the receiver assembly method and documentation.

Additional thanks to Lindsay Ng Lowry for her help in the collimator lens mounting block redesign work.

Chapter 4

Detector and Readout Characterization of Polarbear-2b

In 2019, Polarbear-2b was assembled for the first time in the lab, fully integrated with a full focal plane tower (FPT) and all non-science-grade optics. There were various tests performed to characterize the detectors and verify that these detectors were suitable for science-grade operations. For this test run, the focal plane was comprised of five deployable detector modules and two modules that were eventually deemed insufficient for deployment. These two were replaced by modules that were verified at collaborating institutions.

Three of the deployable detector modules were tested optically. This meant they did not have a wafer cover, and optical signals transmitted from outside of the receiver could be sensed by the detectors. Cryogenic attenuating filters of various thicknesses were mounted in front of them to reduce the amount of optical power on the bolometers. The other four modules were tested dark since this was the first time testing these modules installed in the focal plane (see Figure 4.1).

The results presented here are a combination of the five deployed detector modules plus one additional module from one of the collaborating institutions. The

seventh module was validated for deployment but is not presented in the histograms in the following sections as the readout scheme was slightly different. Based on the measured critical temperature (0.44±0.006 K) and normal resistance (0.98±0.22 Ω)[1] of a characteristic set of detectors, this seventh module was approved for deployment.

The design values for the bolometer characteristics were chosen to optimally function with the DfMux readout, estimated optical power, and estimated noise [39]. The total noise can be expressed as noise-equivalent-power (NEP) which is the signal power required to give a signal-to-noise (SNR) ratio of 1 over a 1 Hz bandwidth usually in units $W/\sqrt{Hz}$. There are four noise sources considered which are photon noise, readout noise, Johnson noise and thermal noise. The latter two are inherent to the detector. The total noise is the sum in quadrature of these four sources (Equation 4.1).

$$NEP_{total} = \sqrt{NEP_\gamma^2 + NEP_{readout}^2 + NEP_{Johnson}^2 + NEP_{thermal}^2} \qquad (4.1)$$

The photon noise arises from quantum mechanics with the random rate of arrival of photons and includes shot noise and photon bunching. Since the photon noise is fundamental to the measurement and unavoidable, the best case is to be photon noise dominated. The readout noise comes from the readout circuit and is inversely proportional to TES responsivity, so with sufficiently high responsivity, the readout noise can be negligible. Johnson noise arises from thermal fluctuations of charge carriers and is also minimized by operating the TES with high loop gain. Thermal fluctuation noise (TFN) is noise from thermal fluctuations in the link between the TES and the bath (see Figure 2.12). TFN is minimized by tuning the bath temperature with the transition temperature of the bolometer so it is not a dominant noise source.

---

[1]These values can be compared to the target values mentioned in Section 4.4 and 4.1 respectively.
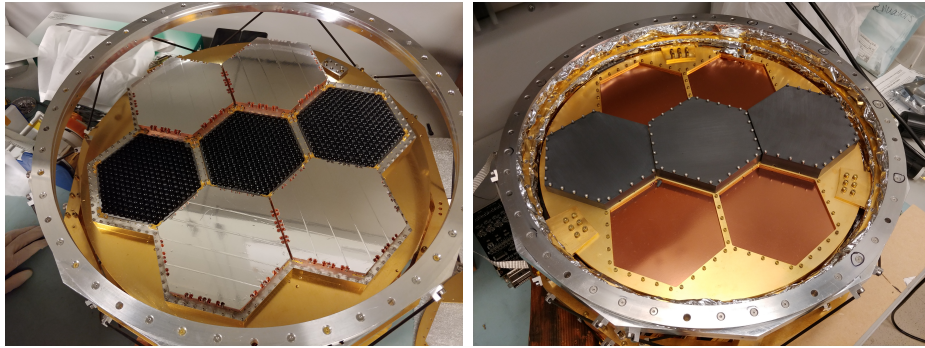
(a) Populated FPT

(b) FPT with MMF and NDFs

Figure 4.1: *Left*: This photo shows the FPT configuration for the final in-lab integrated run before the RF shield, MMF and NDFs were installed. Since the three center wafers were previously installed in the FPT and tested dark, optical tests were performed on them. The other four wafers were being tested for the first time as part of a full focal plane, so they were tested dark necessitating a cover over each one. *Right*: The same FPT now with the RF shield, MMF, and NDFs installed. The NDFs shown here are of varying thickness to determine which would be adequate for properly attenuating room temperature signals so that the optical bolometers would not be saturated.

The following parameters of the detectors are important to analyze in order to ensure that they are adequate for deployment given the design constraints. Each parameter section below has results from the final in-lab integration run as well as the design targets to satisfy the noise requirements in an effort to be photon noise limited.

4.1   Normal Resistance

The normal resistance (R_n) of the bolometer is the resistance of the bolometer when it is above its superconducting transition state and in its normal conducting state. It is measured by heating the bolometer to approximately 600 mK, which is above the designed upper limit of its superconducting transition temperature. Figure 4.2 shows the normal resistance of detectors on six of PB-2b's deployment modules. These values were corrected for parasitic resistance in the bias circuit by subtracting the measured resistance in series with the TES while the TES was in its superconducting state. Additionally, they were corrected for stray series inductance as described in Elleflot et al., 2020 [9], resulting in negligible dependence on channel resonator frequency.
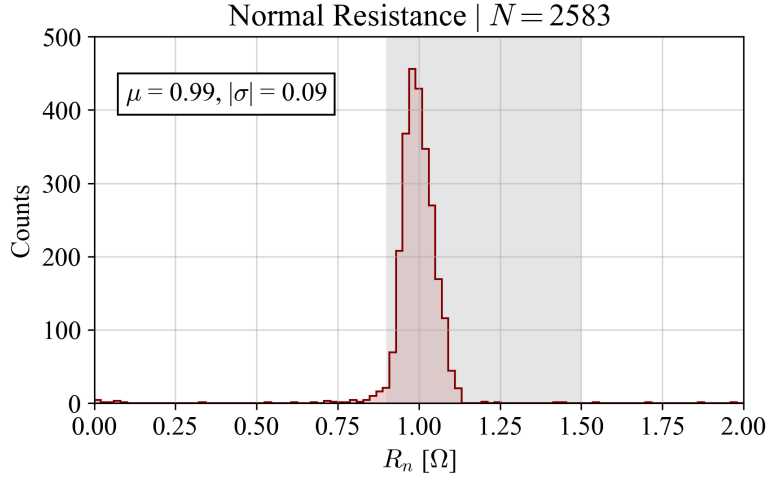
Figure 4.2: A histogram of the normal resistance of 2,583 detectors from six of PB-2b's deployment modules. These values were corrected for parasitic impedances in the bias circuit following the procedure outlined in Elleflot et al., 2020 [9] and resulted in $R_n = 0.99 \pm 0.09$ Ω. The small variance of the distribution results in acceptability for these six wafers. Less than 2% of the R_n values measured fell outside of $0-2$ Ω and were considered outliers or non-real values. These bolometers were designed to have a normal resistance of 1.2 ± 0.3 Ω (gray area) due to the requirements from the DfMux readout system [39]. The measured mean shows a slight deviation from the designed mean, but the overall distribution falls within the design range. The detector yield was diminished in part due to readout hardware failures investigated after the run that are not expected to affect operation in the field. Difficulties with warm readout networking also affected our measurement yield, but these issues were fixed later in the run. We believed this data to be a representative sample of our detectors so no further tests were performed after the networking issues were resolved. Additionally, data on a subset of detectors were excluded from this plot because measurements of stray impedances were insufficient for accurately performing the necessary corrections.

4.2   Turnaround Power

A key criterion in using a TES bolometer is the ability to maintain its operating point within the superconducting transition, and thus it is necessary that the optical and bias power do not drive the bolometer normal. Therefore, an optimal operation power is designed uniquely for each detector frequency band since the amount of optical loading from the atmosphere depends on the antenna frequency. However, measuring this operation power is difficult to do with an automated algorithm for thousands of detectors. Instead, we measure another parameter called turnaround power which is defined as the power when $dI/dV = 0$. This is $\sim10\%$ higher than the operation power.

Turnaround power is measured while there is negligible optical power deposited on the detectors. Thus, the total thermal power on the bolometer island is purely electrical and measurable. The method for performing this test begins with heating the bolometers so that they are in their normal metal state. Next, the bolometers are biased with a high voltage bias. This is called overbiasing the bolometer. Once the bolometers are overbiased, the bath temperatures are lowered to approximately 250 mK. Joule heating maintains the bolometers in their normal state even though their bath temperatures have been lowered. The voltage bias is then incrementally stepped down, lowering the bolometers into their superconducting transition.

With detector sensitivity setting an upper constraint and optical loading setting a lower constraint, the target turnaround power range for the 90 GHz band is $7.8-10.0$ pW, and the target range for the 150 GHz band is $18.9-26.7$ pW [39]. Figure 4.3 shows a histogram of the results fitted to two Gaussian distributions. The resulting means and standard deviations of the fit for 90 GHz and 150 GHz detectors are 9.5 ± 1.3 pW and 21.7 ± 2.2 pW respectively, sufficiently aligning with our target ranges.
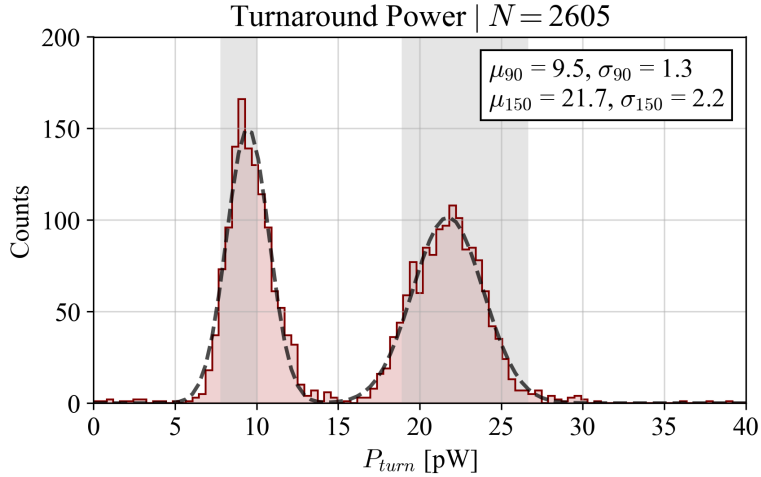
Figure 4.3: A histogram of the bimodal distribution of turnaround power for 2,605 detectors on six PB-2b detector modules. The same parasitic impedance measurements explained in Section 4.1 were used in correcting the turnaround power measurements. Detector yield was affected by the same issues mentioned in Figure 4.2. The lower power distribution is from the 90 GHz band, and the higher power distribution is from the 150 GHz band. The shaded regions indicate the turnaround power target ranges of $7.8-10.0$ pW for the 90 GHz band and $18.9-26.7$ pW for the 150 GHz band [39]. The data were fit to a sum of two Gaussian distributions as shown by the dashed line, and the resulting means and standard deviations for the 90 GHz and 150 GHz bands are 9.5 ± 1.3 pW and 21.7 ± 2.2 pW respectively. These means fall within our design ranges such that we are confident these detectors will be operable in the field.

4.3   Lowest Achieved Operating Resistance

In order to operate our detectors, we must be able to tune them deep enough in their superconducting transition so that we have adequate detector time constants and responsivity. The parameter $\alpha = \frac{\partial \log R}{\partial \log T}$ increases as the bolometer moves deeper into its transition which increases loop gain and responsivity and decreases the detector time constant [16]. As discussed later in Section 4.5, a representative sample of detectors have demonstrated suitable time constants when tuned between

a fractional resistance (R_{TES}/R_n) of 0.4 and 0.7.

In PB-2b's in-lab integration run, we measured the lowest achieved operating resistance for detectors in laboratory conditions for the five deployment wafers which gives information about the range of possible operating resistances. As the voltage bias is lowered and the TES moves deeper into its superconducting transition, there is a point when Joule heating is insufficient to keep the TES from completely transitioning, and the TES abruptly jumps to its superconducting state. This is referred to as latching, at which point the bolometer is no longer operational until it is overbiased again. It can be caused by an imperfect TES bias voltage due to series parasitic resistances or the detector speed exceeding the stability criterion as derived by K. Irwin and G. Hilton, 2006 [16]. The latching resistance (R_{latch}) is the resistance measured just before the TES fully transitions into its superconducting state. The fractional latching resistance is determined by measuring the latching resistance and dividing it by the normal resistance (R_{latch}/R_n), and thereby can indicate the lowest fractional operating resistances for these detectors. Results from these in-lab measurements shown in Figure 4.4 indicate a range of fractional resistances that are satisfactory given our desired time constants as outlined in Section 4.5 with 96% having a fractional latching resistance below 0.7.
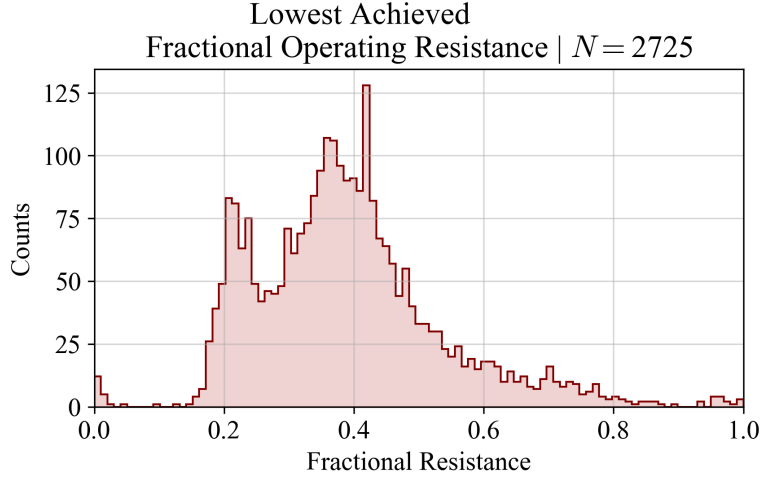
Figure 4.4: A histogram of the lowest achieved fractional operating resistance of 2,725 detectors from five PB-2b deployment detector modules. This shows the distribution of detectors' fractional resistance just before they fully transition to their superconducting state. These values were corrected for parasitic resistances in the same manner as Section 4.1. Less than 0.5% of the data were outside of the fractional resistance range of $0-1$ and are not included in this plot. The yield stated here was affected by the same difficulties as mentioned in Figure 4.2. However, the measurements taken are considered representative of all detectors on these wafers. The tail on the right of the distribution can be explained by premature latching of detectors on a single LC multiplexing chip because of a single detector latching as all channels on a single multiplexing chip were lowered into their transitions in parallel. Regardless, 96% of the detectors shown achieved a fractional resistance below 0.7 which indicates they are capable of operating with suitable time constants as shown in Figure 4.6. Note that this fractional latching resistance measurement is not equivalent to the parasitic resistance in the bias circuit, but it is affected by imperfect voltage bias due to parasitic resistance.

4.4 Critical Temperature

The transition temperature or critical temperature (T_c) is the temperature at which the TES transitions from its normal state to its superconducting state. We

define T_c to be the temperature at which the TES resistance is equal to 80% of its resistance at 500 mK ($\approx 0.8 \times R_n$). Characterizing the transition temperature is critical because the results could determine if the detector is usable. If the transition temperature is too low, we would be unable to use the detector since we might not have the capabilities to cool the detector below its transition. If the transition temperature is too high, the detector will not be sensitive enough to CMB photons because the noise level would be too high.

The method for measuring the transition temperature begins with heating the TESs above the expected critical temperature and biasing them with a minimal voltage bias so as not to cause excess Joule heating. Next, the TES temperature is lowered slowly (~ 5 mK per minute) so that the focal plane thermometer adequately thermalizes with the bolometer temperature. Like the measurements described in Sections 4.1−4.3, this data is taken with negligible optical power incident on the detectors. Figure 4.5 shows results from six deployment PB-2b modules. A different, though we believe equivalent, technique was used in measuring the sixth deployment wafer. The target design range is 0.42 K to 0.47 K [39] which considers the optimal range of critical temperatures given our TES bath temperature capabilities and thermal carrier noise constraints. Approximately 96% of our data falls within this target range.
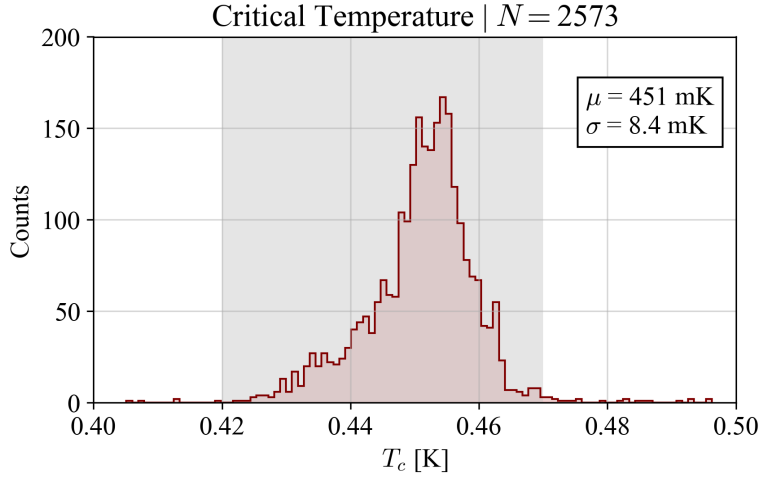
Figure 4.5: A histogram of critical temperature of 2,573 detectors from six of PB-2b's deployment detector modules. Less than 4% of the total measurements lie outside of 0.4−0.5 K and were considered as outliers or non-real values. Therefore, these are not included in this distribution. The detector yield was also diminished in part due to the complications mentioned in Figure 4.2 The gray area represents the design target range of 0.42−0.47 K[39], within which ∼ 96% of the measurements fall.

4.5 Time Constant

Detector time constants, τ, represents the detectors' response time. The lower bound is 0.9 ms set by the readout circuit, and the upper bound is ∼ 29 ms. This upper bound is calculated using our scan frequency and instrument beam size. The instrument beam size is 3.5′, and the designed scan speed is ∼ 2° per second. The scanning movement of the telescope will create a blurring of the sky map in the scan direction unless the detector time constant is at most a factor of a few smaller than the beam crossing time. To ensure that the detectors are fast enough, the designed time constant range is 1-5 ms. A description of the test procedure performed to measure the detector time constants and details about the results can be found in Ito and Lowry, et al. 2020 [17]. Figure 4.6 below are duplicated summaries from this

proceeding.
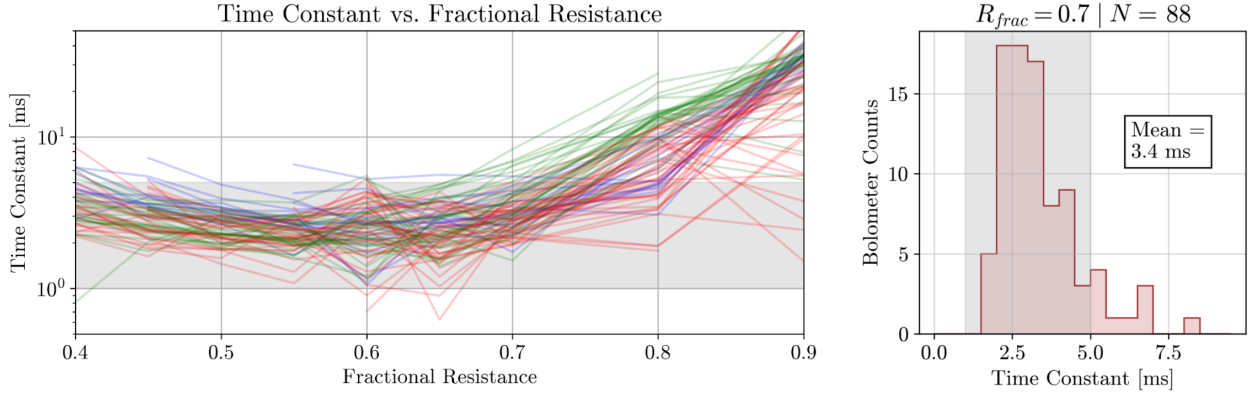
Figure 4.6: *Left:* This plot shows the time constant of a detector as a function of fractional resistance. Each line is a single detector, and lines of the same color are from the same detector module. There are three detector modules represented here. The shaded region is the desired range of time constant (1-5 ms). A high majority of the detectors are within the desired range at 0.7 fractional resistance and below. Analysis and plotting code thanks to Tucker Elleflot. *Right:* This histogram shows the spread of time constants for 88 detectors at 0.7 fractional resistance which is a reasonable operating resistance in the field. Of these, 89% have time constants that fall within the desired range. Plot thanks to Lindsay Ng Lowry.

4.6 SQUIDs

During PB-2b's final integration run, it was found that the SQUIDs originally intended for deployment produced excess noise that varied with current bias amplitude. Since there was insufficient time to properly explore this phenomenon before the scheduled deployment, the decision was made to switch to SA-13 SQUIDs produced by the National Institute of Standards and Technology (NIST). This type of SQUID has been successfully used with PB-2a and does not produce the same amplitude-dependent noise. The deployment set of SQUIDs for PB-2b was tested with open input coils in the PB-2c backend which is identical to PB-2b's backend

down to 4 Kelvin. The results are discussed in length in Ito and Lowry, et al. 2020 [17]. The primary parameters that are characterized are the SQUID transimpedance and the dynamic impedance. Transimpedance (Z_t) is a conversion factor between the change of current (δI_{in}) in the input coil of the SQUID and the change of voltage output (δV_{out}) across the SQUID ($Z_t = \delta V_{out}/\delta I_{in}$). The dynamic impedance (Z_{dyn}) is defined as $\delta V_{out}/\delta I_b$ where δV_{out} is the change of voltage output, and δI_b is the change in bias current in the SQUID. The SQUIDs passed the criteria for deployment as illustrated by Table 4.1. The integrated testing will happen in the field.

Table 4.1: This table summarizes the results from the deployment set of SQUIDs and compares them to the criteria required for deployment [17].

	Average Measured Value	Deployment Criteria
Z_t	627 Ω	≥ 350 Ω
Z_{dyn}	698 Ω	< 900 Ω

4.7   Acknowledgements

Chapter 4 includes material published in J. Ito, L. N. Lowry, T. Elleflot, K. T. Crowley, L. Howe, P. Siritanasak, T. Adkins, K. Arnold, C. Baccigalupi, D. Barron, B. Bixler, Y. Chinone, J. Groh, M. Hazumi, C. A. Hill, O. Jeong, B. Keating, A. Kusaka, A. T. Lee, K. Mitchell, M. Navaroli, A. T. P. Pham, C. Raum, C. L. Reichardt, T. J. Sasse, J. Seibert, A. Suzuki, S. Takakura, G. P. Teply, C. Tsai, and B. Westbrook, "Detector and readout characterization for POLARBEAR-2b," in Millimeter, Submillimeter, and Far-Infrared Detectors and Instrumentation for Astronomy X (J. Zmuidzinas and J.-R. Gao, eds.), vol. 11453, pp. 286 - 301, International Society for Optics and Photonics, SPIE, 2020. The dissertation author was the primary author on this work.

The dissertation author would also like to thank Lindsay Ng Lowry, Logan Howe, Tucker Elleflot, Kevin T. Crowley, Praween Siritinasak for their help in acquiring or

analyzing the data presented and referenced here.

Chapter 5

Conclusion

First light for POLARBEAR-2b has been long awaited and, at the time of this writing, on the brink of commencing. However, getting to this point was not without its struggles as we strove to deploy an instrument during the COVID-19 pandemic. Personnel deployment to the site was particularly limited due to Chile's entry requirements and due to collaborators' home institution's permissions for travel. Yet through some setbacks and obstacles, we succeeded in mounting the PB-2b receiver onto its telescope. Next, commissioning tasks will be performed and reviewed before regular calibration and science observations begin. We look forward to utilizing this instrument, analyzing our science observations, and presenting exciting scientific results in the coming years.

5.1   Polarbear-2b Receiver Deployment

The following entries outline the progress that was accomplished from the initial shipment from UCSD to hoisting the receiver onto the telescope.

November 2019 – the POLARBEAR-2b receiver was disassembled and packed into crates for shipping to Chile to protect the receiver. The focal plane tower was

removed from the receiver and the detector modules were uninstalled. Each detector module was shipped in a plastic case which was well packed in a pelican case. The focal plan tower itself was packaged in its own pelican case. The backend of the receiver was shipped in a dampening crate that was custom made for it. The optics tube shell sections were wrapped in plastic wrap and then bubble wrap and carefully packed in wooden crates. The lenses were shipped in their padded boxes in wooden crate. All the crates were professional packed into a container and shipped overseas down to the site in January 2020.

March 2020 – a team from UCSD deployed to meet the container when it arrived to the site. The container arrived just in time for the assembly team to unload the main crate before having to return to the USA due to the onset of the COVID-19 pandemic. During this time of quarantine, the team refined receiver assembly procedures and began developing calibration methods which is discussed in Section 5.2

February 2021 – a team from UCSD deployed to build the PB-2b receiver. During this time, the team focused on building the backend of the receiver. It was decided that only the backend would be assembled since a couple optical elements with AR coatings would be delayed[1] This change of schedule also impacted the order of operations of receiver assembly. In order to accommodate this, some modifications to receiver assembly instructions were devised such as that which is described in Section 3.4.

May 2021 – another team from UCSD returned to the site to finish the receiver assembly. The optical elements were completed and had arrived at the site. Unfortunately, the day the teams was allowed to go up after mandatory quarantine had the largest snow storm of the past four years. The snow was around 2 meters deep, and it was impossible to clear the road in a timely manner. The team waited for 5

---

[1]New AR methods were developed for PB-2b that differ from PB-2a as concerns about AR-coating delamination on lenses in PB-2a arose.

weeks with the hopes that the roads would be cleared, but it was not possible. The team left in July without being able to continue receiver assembly.

August 2021 – teams from UCSD and UC Berkeley were able to return and finish receiver assembly. Entry restrictions into Chile had relaxed significantly allowing for a larger group of individuals to enter.

November 2021 – the deployed team attempted to hoist the receiver into the telescope; however, one of the hoisting plates that connects the receiver to a lifting strap was installed with inadequate length screws and just as the receiver was in position to be bolted into the telescope boom, the screws pulled out and the receiver shifted its weight such that it was now hanging at an angle under the telescope. One of the vacuum ports was sheared off in the process which dramatically vented the receiver. Thankfully, no one was injured.

After safely lowering the receiver back to the ground, the team began disassembling the receiver, taking detailed notes of any observed damage. There were a couple items that were severely damaged and required replacing besides the vacuum shell with the sheared-off port. A linear actuator motor that is used to grip and hold the wave-plate in place was bent. The IR filter that lives just behind the window had spectacularly shattered. Additionally, some of the G10 struts were obviously damaged from this incident which prompted us to redesign these struts as is described in Section 2.4.2.

The Simons Array collaboration promptly addressed and discussed this incident with an external review board that gave design and procedural recommendations which were implemented in the next hoisting attempt.

April 2022 – teams from UCSD and UC Berkeley again deployed to the site to reassemble PB-2b. The receiver was successfully reassembled including the new parts that were made after the hoisting incident.

July 20, 2022 – the site team successfully hoisted and secured the receiver in the Paul Simons telescope.

At the time of this writing, PB-2b has commenced its initial cooldown for its commissioning run. Once cold, the detector noise will be characterized and reviewed in a commissioning review session to determine the effectiveness of PB-2b for science operations. After a successful commissioning review, PB-2b will continue its commissioning run by taking initial calibration data. After that, regular science observations, which include regular calibration activities, will begin. Some issues were discovered that have limited the sensitivity in PB-2a which are believed to have been fixed in PB-2b. With this increased sensitivity, the signal-to-noise ratio will increase allowing better study of CMB polarization.

5.2 Calibrating Polarbear-2b

There are four main calibration tasks that must be completed. Only the first one discusses what will be required for the commissioning review as this information can be used, along with the measured number of functioning detectors in the focal plane, to characterize instrument sensitivity.

The first calibration task requires understanding the conversion factor between the current measured in the bolometer and the on-sky temperature, otherwise known as detector gain. There is an absolute and relative gain calibration that is necessary. The absolute calibration requires a planet observation in order to have a known temperature source illuminate a single detector. The relative calibration utilizes a thermal source to measure detector gain variation as a function of time. The planet and thermal source measurements will also be used to calculate detector time constants which will be included in the commissioning review as well.

Another calibration is the pointing calibration. Since the telescope encoders are not completely accurate in giving the azimuth and elevation position on the sky, there is a calibration required. This calibration involves a pointing model that was implemented for POLARBEAR [4, 3]. There there are five, eight, and ten parameter

models. Multiple radio sources and planet observations are required to model the telescope pointing. Targets must be observed at locations across the sky to provide adequate coverage in the azimuth and elevation of the telescope (Figure 5.1). Pointing observations are taken on a weekly basis.

The third important calibration is polarization angle. This identifies the polarization orientation of each detector. There are three different methods available. The first is to shine a calibrated polarization source at our detectors. The second uses a wire grid which rotates at a known frequency. The third method requires the cross-spectrum of E-modes and B-modes to be null which is appropriate in the standard cosmology. Once this calibration task is complete, it does not need to be repeated throughout science observations.

The fourth calibration task is understanding the angular response of the detector by taking detector beam maps. This is done by scanning across a planet that is a point source as seen by the detector. Jupiter is usually scanned for this measurement. Since features on small angular scales are averaged out and not seen in the final CMB maps, beam maps are used to understand the averaging process that occurs in order to determine these features.

Using these calibration measurements, we can then construct a full hardware map. This hardware map outlines the detector position, frequency, and polarization and details the readout chain of this detector. Understanding these properties of each detector is important so that all detectors can be combined and analyzed to make well-understood maps of the sky. From these maps, power spectra are made from which science results can be taken. The results can be compared with theoretical predictions regarding the standard cosmological model and inflation. By constraining inflation, there is an opportunity to open a window into physics at energy scales current unimaginable and further explore the cosmology and perhaps cosmogony of our Universe.
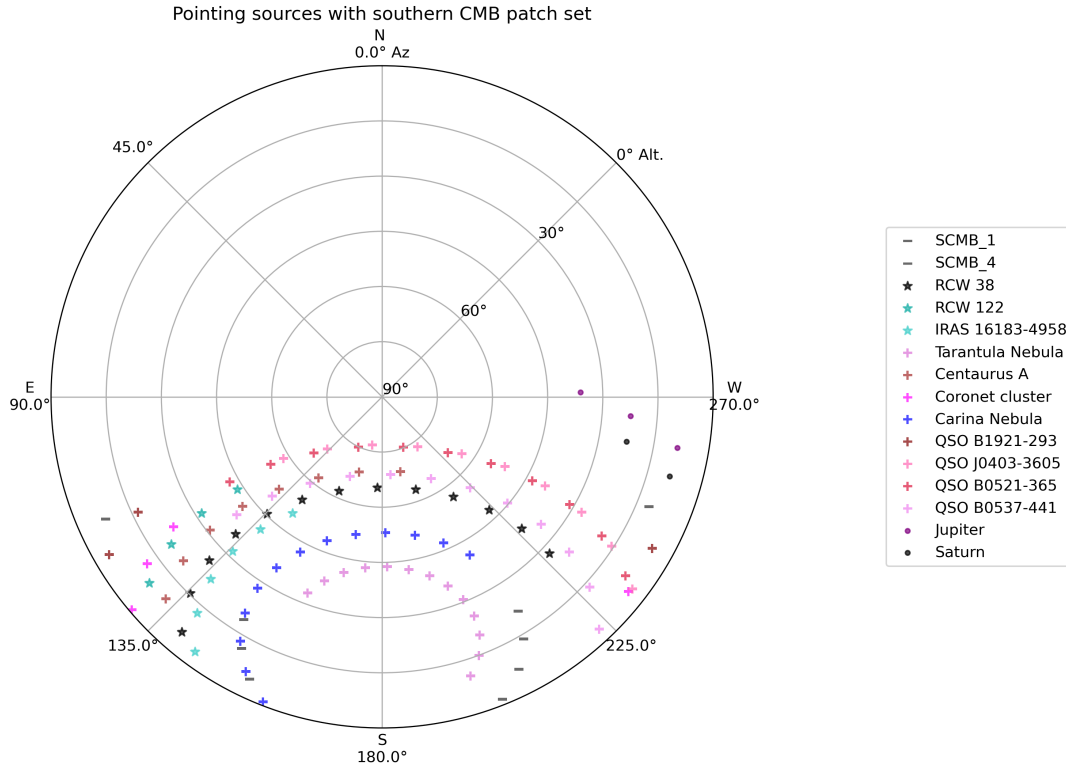
Figure 5.1: This figure shows the possible observable pointing sources that could be used for PB-2b. The map is a circular plot with zenith (right above the telescope) at the center of the plot and the outer circle representing the horizon. Each concentric circle is a 15° step in elevation. The compass directions are listed on the vertical and horizontal axes with north as 0° in azimuth. The flat dashed lines represent the elevation edges of the southern CMB patch. The star markers represent sources that have been observed and analyzed for PB-2a's pointing calibration. The plus signs are other possible sources that could be used to expand the azimuth and elevation coverage. Circular markers represent planets that can be used as pointing calibration sources. Source positions are shown at one hour increments over the time period that the CMB patch is below elevation of 30°.

5.3   Future Outlook

Beyond Simons Array, there are other new and exciting CMB projects that are up and coming. The Simons Observatory is currently under construction with its first three small aperture telescope platforms having arrived to the site in May of 2022 [21]. Additionally, many of the technologies used in Simons Observatory will be used in a larger project known as CMB-S4 which is a conglomerate of ground-based CMB experiments which will expand the limits of what we can observe from the ground [1]. CMB-S4 in Chile will be a neighbor to Simons Observatory. Other than ground-based experiments, there is a space-based project LiteBird which is a JAXA-led project [11]. These are just a couple other CMB projects currently being built and developed. As more detectors are on-sky, more will be revealed about the CMB and other aspects of our Universe.

CMB experimentation continues to be a fascinating field of exploration for two reasons. The first is an amazing symbiotic relationship between scientific demands and technological advancements. In developing CMB instrumentation, much research is required in order to build systems that are capable of obtaining the necessary sensitivity for studying the CMB. There is a natural feedback loop where results from a current instrument inform the design of the next, and the old adage "Necessity is the mother of invention" still rings true.

Secondly, CMB experimentation is a necessary piece in broadening cosmological understandings. It assists in validating or revising theoretical cosmological models. Results are used not only in understanding more about the very early Universe, but also in unveiling more about the evolution of the Universe we have now. It can provide insight into areas of study such as neutrinos, large scale structure of the Universe, dark matter, dark energy, and baryonic matter. Because of this broad utility, it will continue to be an area of expanding research and exploration for years to come.

Appendix A

Strut Testing Details

Here are further details about the strut testing described in Section 2.4.2.

Table A.1 shows results regarding backend aperture strut testing. The first few struts assembled were using G10 material type 1. Struts were made of both the longer and shorter lengths and were tested under tension and shear type 1 tests.

Table A.1: This table presents the maximum force achieved in tension and shear of the backend aperture struts.

G10 Strut	Max Force [N]	
	Tension	Shear Type 1
1	1293.65	-
2	1878.30	-
3	536.29	-
4	1005.47	-
5	-	89.38

Tables A.2, A.3, and A.4 show the results of type 1, type 2, and type 3 G10 material respectively, from tension and type 1 shear tests. For the struts that underwent both types of testing, the shear test was performed first, and no damage was seen after test completion so a tension test was performed afterwards.

Table A.2: This table presents the results from OT G10 struts made with type 1 G10 material.

G10 Strut	Max Force [N]	
	Tension	Shear Type 1
1	1004.53	32.21
2	1067.31	33.72
3	1365.83	-
4	755.35	-
5	705.27	-

Table A.3: This table presents the results from OT G10 struts made with type 2 G10 material.

G10 Strut	Max Force [N]	
	Tension	Shear Type 1
1	2972.51	163.22
2	2976.54	181.10
3	2840.71	-

Table A.4: This table presents the results from OT G10 struts made with type 3 G10 material.

G10 Strut	Max Force [N]	
	Tension	Shear Type 1
1	2721.45	115.63
2	2864.08	-

Bibliography

[1] Kevork Abazajian, Graeme Addison, Peter Adshead, Zeeshan Ahmed, Steven W. Allen, David Alonso, Marcelo Alvarez, Adam Anderson, Kam S. Arnold, Carlo Baccigalupi, Kathy Bailey, Denis Barkats, Darcy Barron, Peter S. Barry, James G. Bartlett, Ritoban Basu Thakur, Nicholas Battaglia, Eric Baxter, Rachel Bean, Chris Bebek, Amy N. Bender, Bradford A. Benson, Edo Berger, Sanah Bhimani, Colin A. Bischoff, Lindsey Bleem, Sebastian Bocquet, Kimberly Boddy, Matteo Bonato, J. Richard Bond, Julian Borrill, François R. Bouchet, Michael L. Brown, Sean Bryan, Blakesley Burkhart, Victor Buza, Karen Byrum, Erminia Calabrese, Victoria Calafut, Robert Caldwell, John E. Carlstrom, Julien Carron, Thomas Cecil, Anthony Challinor, Clarence L. Chang, Yuji Chinone, Hsiao-Mei Sherry Cho, Asantha Cooray, Thomas M. Crawford, Abigail Crites, Ari Cukierman, Francis-Yan Cyr-Racine, Tijmen de Haan, Gianfranco de Zotti, Jacques Delabrouille, Marcel Demarteau, Mark Devlin, Eleonora Di Valentino, Matt Dobbs, Shannon Duff, Adriaan Duivenvoorden, Cora Dvorkin, William Edwards, Joseph Eimer, Josquin Errard, Thomas Essinger-Hileman, Giulio Fabbian, Chang Feng, Simone Ferraro, Jeffrey P. Filippini, Raphael Flauger, Brenna Flaugher, Aurelien A. Fraisse, Andrei Frolov, Nicholas Galitzki, Silvia Galli, Ken Ganga, Martina Gerbino, Murdock Gilchriese, Vera Gluscevic, Daniel Green, Daniel Grin, Evan Grohs, Riccardo Gualtieri, Victor Guarino, Jon E. Gudmundsson, Salman Habib, Gunther Haller, Mark Halpern, Nils W. Halverson, Shaul Hanany, Kathleen Harrington, Masaya Hasegawa, Matthew Hasselfield, Masashi Hazumi, Katrin Heitmann, Shawn Henderson, Jason W. Henning, J. Colin Hill, Renée Hlozek, Gil Holder, William Holzapfel, Johannes Hubmayr, Kevin M. Huffenberger, Michael Huffer, Howard Hui, Kent Irwin, Bradley R. Johnson, Doug Johnstone, William C. Jones, Kirit Karkare, Nobuhiko Katayama, James Kerby, Sarah Kernovsky, Reijo Keskitalo, Theodore Kisner, Lloyd Knox, Arthur Kosowsky, John Kovac, Ely D. Kovetz, Steve Kuhlmann, Chao-lin Kuo, Nadine Kurita, Akito

Kusaka, Anne Lahteenmaki, Charles R. Lawrence, Adrian T. Lee, Antony Lewis, Dale Li, Eric Linder, Marilena Loverde, Amy Lowitz, Mathew S. Madhavacheril, Adam Mantz, Frederick Matsuda, Philip Mauskopf, Jeff McMahon, Matthew McQuinn, P. Daniel Meerburg, Jean-Baptiste Melin, Joel Meyers, Marius Millea, Joseph Mohr, Lorenzo Moncelsi, Tony Mroczkowski, Suvodip Mukherjee, Moritz Münchmeyer, Daisuke Nagai, Johanna Nagy, Toshiya Namikawa, Federico Nati, Tyler Natoli, Mattia Negrello, Laura Newburgh, Michael D. Niemack, Haruki Nishino, Martin Nordby, Valentine Novosad, Paul O'Connor, Georges Obied, Stephen Padin, Shivam Pandey, Bruce Partridge, Elena Pierpaoli, Levon Pogosian, Clement Pryke, Giuseppe Puglisi, Benjamin Racine, Srinivasan Raghunathan, Alexandra Rahlin, Srini Rajagopalan, Marco Raveri, Mark Reichanadter, Christian L. Reichardt, Mathieu Remazeilles, Graca Rocha, Natalie A. Roe, Anirban Roy, John Ruhl, Maria Salatino, Benjamin Saliwanchik, Emmanuel Schaan, Alessandro Schillaci, Marcel M. Schmittfull, Douglas Scott, Neelima Sehgal, Sarah Shandera, Christopher Sheehy, Blake D. Sherwin, Erik Shirokoff, Sara M. Simon, Anze Slosar, Rachel Somerville, David Spergel, Suzanne T. Staggs, Antony Stark, Radek Stompor, Kyle T. Story, Chris Stoughton, Aritoki Suzuki, Osamu Tajima, Grant P. Teply, Keith Thompson, Peter Timbie, Maurizio Tomasi, Jesse I. Treu, Matthieu Tristram, Gregory Tucker, Caterina Umiltà, Alexander van Engelen, Joaquin D. Vieira, Abigail G. Vieregg, Mark Vogelsberger, Gensheng Wang, Scott Watson, Martin White, Nathan Whitehorn, Edward J. Wollack, W. L. Kimmy Wu, Zhilei Xu, Siavash Yasini, James Yeck, Ki Won Yoon, Edward Young, and Andrea Zonca. Cmb-s4 science case, reference design, and project plan, 2019.

[2] S. Adachi, T. Adkins, M. A. O. Aguilar Faú ndez, K. S. Arnold, C. Baccigalupi, D. Barron, S. Chapman, K. Cheung, Y. Chinone, K. T. Crowley, T. Elleflot, J. Errard, G. Fabbian, C. Feng, T. Fujino, N. Galitzki, N. W. Halverson, M. Hasegawa, M. Hazumi, H. Hirose, L. Howe, J. Ito, O. Jeong, D. Kaneko, N. Katayama, B. Keating, T. Kisner, N. Krachmalnicoff, A. Kusaka, A. T. Lee, E. Linder, A. I. Lonappan, L. N. Lowry, F. Matsuda, T. Matsumura, Y. Minami, M. Murata, H. Nishino, Y. Nishinomiya, D. Poletti, C. L. Reichardt, C. Ross, Y. Segawa, P. Siritanasak, R. Stompor, A. Suzuki, O. Tajima, S. Takakura, S. Takatori, D. Tanabe, G. Teply, K. Yamada, and Y. Zhou. Improved upper limit on degree-scale CMB b-mode polarization power from the 670 square-degree POLARBEAR survey. *The Astrophysical Journal*, 931(2):101, May 2022.

[3] The Polarbear Collaboration: P. A. R. Ade, M. Aguilar, Y. Akiba, K. Arnold, C. Baccigalupi, D. Barron, D. Beck, F. Bianchini, D. Boettger, J. Borrill,

S. Chapman, Y. Chinone, K. Crowley, A. Cukierman, R. Dünner, M. Dobbs, A. Ducout, T. Elleflot, J. Errard, G. Fabbian, S. M. Feeney, C. Feng, T. Fujino, N. Galitzki, A. Gilbert, N. Goeckner-Wald, J. C. Groh, G. Hall, N. Halverson, T. Hamada, M. Hasegawa, M. Hazumi, C. A. Hill, L. Howe, Y. Inoue, G. Jaehnig, A. H. Jaffe, O. Jeong, D. Kaneko, N. Katayama, B. Keating, R. Keskitalo, T. Kisner, N. Krachmalnicoff, A. Kusaka, M. Le Jeune, A. T. Lee, E. M. Leitch, D. Leon, E. Linder, L. Lowry, F. Matsuda, T. Matsumura, Y. Minami, J. Montgomery, M. Navaroli, H. Nishino, H. Paar, J. Peloton, A. T. P. Pham, D. Poletti, G. Puglisi, C. L. Reichardt, P. L. Richards, C. Ross, Y. Segawa, B. D. Sherwin, M. Silva-Feaver, P. Siritanasak, N. Stebor, R. Stompor, A. Suzuki, O. Tajima, S. Takakura, S. Takatori, D. Tanabe, G. P. Teply, T. Tomaru, C. Tucker, N. Whitehorn, and A. Zahn. A measurement of the cosmic microwave backgroundib/i-mode polarization power spectrum at subdegree scales from two years of polarbear data. *The Astrophysical Journal*, 848(2):121, October 2017.

[4] The Polarbear Collaboration: P. A. R. Ade, Y. Akiba, A. E. Anthony, K. Arnold, M. Atlas, D. Barron, D. Boettger, J. Borrill, S. Chapman, Y. Chinone, M. Dobbs, T. Elleflot, J. Errard, G. Fabbian, C. Feng, D. Flanigan, A. Gilbert, W. Grainger, N. W. Halverson, M. Hasegawa, K. Hattori, M. Hazumi, W. L. Holzapfel, Y. Hori, J. Howard, P. Hyland, Y. Inoue, G. C. Jaehnig, A. H. Jaffe, B. Keating, Z. Kermish, R. Keskitalo, T. Kisner, M. Le Jeune, A. T. Lee, E. M. Leitch, E. Linder, M. Lungu, F. Matsuda, T. Matsumura, X. Meng, N. J. Miller, H. Morii, S. Moyerman, M. J. Myers, M. Navaroli, H. Nishino, A. Orlando, H. Paar, J. Peloton, D. Poletti, E. Quealy, G. Rebeiz, C. L. Reichardt, P. L. Richards, C. Ross, I. Schanning, D. E. Schenck, B. D. Sherwin, A. Shimizu, C. Shimmin, M. Shimon, P. Siritanasak, G. Smecher, H. Spieler, N. Stebor, B. Steinbach, R. Stompor, A. Suzuki, S. Takakura, T. Tomaru, B. Wilson, A. Yadav, and O. Zahn. A measurement of the cosmic microwave background b-mode polarization power spectrum at sub-degree scales with polarbear. *The Astrophysical Journal*, 794(2):171, October 2014.

[5] Juhyeok Choi, H Ishitsuka, Satoru Mima, S Oguri, K Takahashi, and O Tajima. Radio-transparent multi-layer insulation for radiowave receivers. *The Review of scientific instruments*, 84:114502, November 2013.

[6] Kevin D. Crowley, Peter Dow, Jordan E. Shroyer, John C. Groh, Bradley Dober, Jacob Spisak, Nicholas Galitzki, Tanay Bhandarkar, Mark J. Devlin, Simon Dicker, Patricio A. Gallardo, Kathleen Harrington, Bradley R. Johnson, Delwin

Johnson, Anna M. Kofman, Akito Kusaka, Adrian Lee, Michele Limon, Jeffrey Iuliano, Federico Nati, John Orlowski-Scherer, Lyman Page, Michael Randall, Grant Teply, Tran Tsan, Edward J. Wollack, Zhilei Xu, and Ningfeng Zhu. The Simons Observatory: Design and Measured Performance of a Carbon Fiber Strut for a Cryogenic Truss. *arXiv e-prints*, page arXiv:2201.06094, January 2022.

[7] Dictionary.com. Cosmology, 2022.

[8] M. A. Dobbs, M. Lueker, K. A. Aird, A. N. Bender, B. A. Benson, L. E. Bleem, J. E. Carlstrom, C. L. Chang, H. M. Cho, J. Clarke, T. M. Crawford, A. T. Crites, D. I. Flanigan, T. de Haan, E. M. George, N. W. Halverson, W. L. Holzapfel, J. D. Hrubes, B. R. Johnson, J. Joseph, R. Keisler, J. Kennedy, Z. Kermish, T. M. Lanting, A. T. Lee, E. M. Leitch, D. Luong-Van, J. J. McMahon, J. Mehl, S. S. Meyer, T. E. Montroy, S. Padin, T. Plagge, C. Pryke, P. L. Richards, J. E. Ruhl, K. K. Schaffer, D. Schwan, E. Shirokoff, H. G. Spieler, Z. Staniszewski, A. A. Stark, K. Vanderlinde, J. D. Vieira, C. Vu, B. Westbrook, and R. Williamson. Frequency multiplexed superconducting quantum interference device readout of large bolometer arrays for cosmic microwave background measurements. *Review of Scientific Instruments*, 83(7):073113–073113–24, July 2012.

[9] T. Elleflot, K. Arnold, D. Barron, K. T. Crowley, M. Dobbs, J. Groh, M. Hasegawa, M. Hazumi, C. Hill, L. Howe, J. Ito, O. Jeong, D. Kaneko, N. Katayama, B. Keating, A. Kusaka, A. T. Lee, L. N. Lowry, C. Raum, J. Seibert, M. Silva-Feaver, P. Siritanasak, A. Suzuki, S. Takakura, S. Takatori, C. Tsai, and B. Westbrook. Effect of Stray Impedance in Frequency-Division Multiplexed Readout of TES Sensors in POLARBEAR-2b. *Journal of Low Temperature Physics*, 199(3-4):840–848, March 2020.

[10] Tucker Elleflot. *Measuring the Polarization of the Cosmic Microwave Background with POLARBEAR-1 and Developing the Next-Generation Experiment POLARBEAR-2*. PhD thesis, University of California, San Diego, 2019.

[11] Masashi Hazumi, Peter A. Ade, Alexandre Adler, Erwan Allys, Kam Arnold, Didier Auguste, Jonathan Aumont, Ragnhild Aurlien, Jason Austermann, Carlo Baccigalupi, Anthony J. Banday, R. Banjeri, Rita B. Barreiro, Soumen Basak, Jim Beall, Dominic Beck, Shawn Beckman, Juan Bermejo, Paolo de Bernardis, Marco Bersanelli, Julien Bonis, Julian Borrill, Francois Boulanger,

Sophie Bounissou, Maksym Brilenkov, Michael Brown, Martin Bucher, Erminia Calabrese, Paolo Campeti, Alessandro Carones, Francisco J. Casas, Anthony Challinor, Victor Chan, Kolen Cheung, Yuji Chinone, Jean F. Cliche, Loris Colombo, Fabio Columbro, Javier Cubas, Ari Cukierman, David Curtis, Giuseppe D'Alessandro, Nadia Dachlythra, Marco De Petris, Clive Dickinson, Patricia Diego-Palazuelos, Matt Dobbs, Tadayasu Dotani, Lionel Duband, Shannon Duff, Jean M. Duval, Ken Ebisawa, Tucker Elleflot, Hans K. Eriksen, Josquin Errard, Thomas Essinger-Hileman, Fabio Finelli, Raphael Flauger, Cristian Franceschet, Unni Fuskeland, Mathew Galloway, Ken Ganga, Jian R. Gao, Ricardo Genova-Santos, Martina Gerbino, Massimo Gervasi, Tommaso Ghigna, Eirik Gjerløw, Marcin L. Gradziel, Julien Grain, Frank Grupp, Alessandro Gruppuso, Jon E. Gudmundsson, Tijmen de Haan, Nils W. Halverson, Peter Hargrave, Takashi Hasebe, Masaya Hasegawa, Makoto Hattori, Sophie Henrot-Versillé, Daniel Herman, Diego Herranz, Charles A. Hill, Gene Hilton, Yukimasa Hirota, Eric Hivon, Renee A. Hlozek, Yurika Hoshino, Elena de la Hoz, Johannes Hubmayr, Kiyotomo Ichiki, Teruhito Iida, Hiroaki Imada, Kosei Ishimura, Hirokazu Ishino, Greg Jaehnig, Tooru Kaga, Shingo Kashima, Nobuhiko Katayama, Akihiro Kato, Takeo Kawasaki, Reijo Keskitalo, Theodore Kisner, Yohei Kobayashi, Nozomu Kogiso, Alan Kogut, Kazunori Kohri, Eiichiro Komatsu, Kunimoto Komatsu, Kuniaki Konishi, Nicoletta Krachmalnicoff, Ingo Kreykenbohm, Chao-Lin L. Kuo, Akihiro Kushino, Luca Lamagna, Jeff V. Lanen, Massimiliano Lattanzi, Adrian T. Lee, Clément Leloup, François Levrier, Eric Linder, Thibaut Louis, Gemma Luzzi, Thierry Maciaszek, Bruno Maffei, Davide Maino, Muneyoshi Maki, Stefano Mandelli, Enrique Martinez-Gonzalez, Silvia Masi, Tomotake Matsumura, Aniello Mennella, Marina Migliaccio, Yuto Minami, Kazuhisa Mitsuda, Joshua Montgomery, Ludovic Montier, Gianluca Morgante, Baptiste Mot, Yasuhiro Murata, John A. Murphy, Makoto Nagai, Yuya Nagano, Taketo Nagasaki, Ryo Nagata, Shogo Nakamura, Toshiya Namikawa, Paolo Natoli, Simran Nerval, Toshiyuki Nishibori, Haruki Nishino, Fabio Noviello, Créidhe O'Sullivan, Hideo Ogawa, Hiroyuki Ogawa, Shugo Oguri, Hiroyuki Ohsaki, Izumi S. Ohta, Norio Okada, Nozomi Okada, Luca Pagano, Alessandro Paiella, Daniela Paoletti, Guillaume Patanchon, Julien Peloton, Francesco Piacentini, Giampaolo Pisano, Gianluca Polenta, Davide Poletti, Thomas Prouvé, Giuseppe Puglisi, Damien Rambaud, Christopher Raum, Sabrina Realini, Martin Reinecke, Mathieu Remazeilles, Alessia Ritacco, Gilles Roudil, Jose A. Rubino-Martin, Megan Russell, Haruyuki Sakurai, Yuki Sakurai, Maura Sandri, Manami Sasaki, Giorgio Savini, Douglas Scott, Joseph Seibert, Yutaro Sekimoto, Blake Sherwin, Keisuke Shinozaki, Maresuke Shiraishi, Peter

Shirron, Giovanni Signorelli, Graeme Smecher, Samantha Stever, Radek Stompor, Hajime Sugai, Shinya Sugiyama, Aritoki Suzuki, Junichi Suzuki, Trygve L. Svalheim, Eric Switzer, Ryota Takaku, Hayato Takakura, Satoru Takakura, Yusuke Takase, Youichi Takeda, Andrea Tartari, Ellen Taylor, Yutaka Terao, Harald Thommesen, Keith L. Thompson, Ben Thorne, Takayuki Toda, Maurizio Tomasi, Mayu Tominaga, Neil Trappe, Matthieu Tristram, Masatoshi Tsuji, Masahiro Tsujimoto, Carole Tucker, Joe Ullom, Gerard Vermeulen, Patricio Vielva, Fabrizio Villa, Michael Vissers, Nicola Vittorio, Ingunn Wehus, Jochen Weller, Benjamin Westbrook, Joern Wilms, Berend Winter, Edward J. Wollack, Noriko Y. Yamasaki, Tetsuya Yoshida, Junji Yumoto, Mario Zannoni, and Andrea Zonca. LiteBIRD satellite: JAXA's new strategic l-class mission for all-sky surveys of cosmic microwave background polarization. In Makenzie Lystrup, Natalie Batalha, Edward C. Tong, Nicholas Siegler, and Marshall D. Perrin, editors, *Space Telescopes and Instrumentation 2020: Optical, Infrared, and Millimeter Wave*. SPIE, December 2020.

[12] Norriss Hetherington and Patrick McCray. Cosmic journey: A history of scientific cosmology, January 2007.

[13] C. A. Hill, A. Kusaka, P. Ashton, P. Barton, T. Adkins, K. Arnold, B. Bixler, S. Ganjam, A. T. Lee, F. Matsuda, T. Matsumura, Y. Sakurai, R. Tat, and Y. Zhou. A cryogenic continuously rotating half-wave plate mechanism for the polarbear-2b cosmic microwave background receiver. *Review of Scientific Instruments*, 91(12):124503, 2020.

[14] Charles A. Hill, Shawn Beckman, Yuji Chinone, Neil Goeckner-Wald, Masashi Hazumi, Brian Keating, Akito Kusaka, Adrian T. Lee, Frederick Matsuda, Richard Plambeck, Aritoki Suzuki, and Satoru Takakura. Design and development of an ambient-temperature continuously-rotating achromatic half-wave plate for CMB polarization modulation on the POLARBEAR-2 experiment. In Wayne S. Holland and Jonas Zmuidzinas, editors, *Millimeter, Submillimeter, and Far-Infrared Detectors and Instrumentation for Astronomy VIII*, volume 9914, pages 699 – 716. International Society for Optics and Photonics, SPIE, 2016.

[15] Logan Howe, Calvin Tsai, Lindsay Lowry, Kam Arnold, Gabriele Coppi, John Groh, Xiaoyu Guo, Brian Keating, Adrian Lee, Andrew J. May, Lucio Piccirillo, Nathan Stebor, and Grant Teply. Design and characterization of the polarbear-2b and polarbear-2c cosmic microwave background cryogenic receivers. arXiv, 2018.

[16] K. Irwin and G. Hilton. Transition-edge sensors. 2006.

[17] J. Ito, L. N. Lowry, T. Elleflot, K. T. Crowley, L. Howe, P. Siritanasak, T. Adkins, K. Arnold, C. Baccigalupi, D. Barron, B. Bixler, Y. Chinone, J. Groh, M. Hazumi, C. A. Hill, O. Jeong, B. Keating, A. Kusaka, A. T. Lee, K. Mitchell, M. Navaroli, A. T. P. Pham, C. Raum, C. L. Reichardt, T. J. Sasse, J. Seibert, A. Suzuki, S. Takakura, G. P. Teply, C. Tsai, and B. Westbrook. Detector and readout characterization for POLARBEAR-2b. In Jonas Zmuidzinas and Jian-Rong Gao, editors, *Millimeter, Submillimeter, and Far-Infrared Detectors and Instrumentation for Astronomy X*, volume 11453, pages 286 – 301. International Society for Optics and Photonics, SPIE, 2020.

[18] O. Jeong. *Development of Simons Array Optics for Cosmic Microwave Background Polarimetry.* PhD thesis, University of California, Berkeley, Berkeley, California, USA, 2021.

[19] Daisuke Kaneko, S. Adachi, P. A. R. Ade, M. Aguilar Faúndez, Y. Akiba, K. Arnold, C. Baccigalupi, D. Barron, D. Beck, S. Beckman, F. Bianchini, D. Boettger, J. Borrill, J. Carron, S. Chapman, K. Cheung, Y. Chinone, K. Crowley, A. Cukierman, M. Dobbs, R. Dżnner, H. El-Bouhargani, T. Elleflot, J. Errard, G. Fabbian, S. M. Feeney, C. Feng, T. Fujino, N. Galitzki, A. Gilbert, N. Goeckner-Wald, J. Groh, G. Hall, N. W. Halverson, T. Hamada, M. Hasegawa, M. Hazumi, C. A. Hill, L. Howe, Y. Inoue, G. Jaehnig, O. Jeong, N. Katayama, B. Keating, R. Keskitalo, S. Kikuchi, T. Kisner, N. Krachmalnicoff, A. Kusaka, A. T. Lee, D. Leon, E. Linder, L. N. Lowry, A. Mangu, F. Matsuda, Y. Minami, M. Navaroli, H. Nishino, J. Peloton, A. T. P. Pham, D. Poletti, G. Puglisi, C. L. Reichardt, C. Ross, Y. Segawa, M. Silva-Feaver, P. Siritanasak, N. Stebor, R. Stompor, A. Suzuki, O. Tajima, S. Takakura, S. Takatori, D. Tanabe, G. P. Teply, T. Tomaru, C. Tsai, C. Verges, B. Westbrook, and Y. Zhou. Deployment of POLARBEAR-2A. *Journal of Low Temperature Physics*, 199(3-4):1137–1147, March 2020.

[20] Helge Kragh. Cosmology and the Origin of the Universe: Historical and Conceptual Perspectives. *arXiv e-prints*, page arXiv:1706.00726, June 2017.

[21] Adrian Lee, Maximilian H. Abitbol, Shunsuke Adachi, Peter Ade, James Aguirre, Zeeshan Ahmed, Simone Aiola, Aamir Ali, David Alonso, Marcelo A. Alvarez, Kam Arnold, Peter Ashton, Zachary Atkins, Jason Austermann, Humna Awan, Carlo Baccigalupi, Taylor Baildon, Anton Baleato Lizancos, Darcy Barron, Nick Battaglia, Richard Battye, Eric Baxter, Andrew

Bazarko, James A. Beall, Rachel Bean, Dominic Beck, Shawn Beckman, Benjamin Beringue, Tanay Bhandarkar, Sanah Bhimani, Federico Bianchini, Steven Boada, David Boettger, Boris Bolliet, J. Richard Bond, Julian Borrill, Michael L. Brown, Sarah Marie Bruno, Sean Bryan, Erminia Calabrese, Victoria Calafut, Paolo Calisse, Julien Carron, Fred. M. Carl, Juan Cayuso, Anthony Challinor, Grace Chesmore, Yuji Chinone, Jens Chluba, Hsiao-Mei Sherry Cho, Steve Choi, Susan Clark, Philip Clarke, Carlo Contaldi, Gabriele Coppi, Nicholas F. Cothard, Kevin Coughlin, Will Coulton, Devin Crichton, Kevin D. Crowley, Kevin T. Crowley, Ari Cukierman, John M. D'Ewart, Rolando Dünner, Tijmen de Haan, Mark Devlin, Simon Dicker, Bradley Dober, Cody J. Duell, Shannon Duff, Adri Duivenvoorden, Jo Dunkley, Hamza El Bouhargani, Josquin Errard, Giulio Fabbian, Stephen Feeney, James Fergusson, Simone Ferraro, Pedro Fluxa, Katherine Freese, Josef C. Frisch, Andrei Frolov, George Fuller, Nicholas Galitzki, Patricio A. Gallardo, Jose Tomas Galvez Ghersi, Jiansong Gao, Eric Gawiser, Martina Gerbino, Vera Gluscevic, Neil Goeckner-Wald, Joseph Golec, Sam Gordon, Megan Gralla, Daniel Green, Arpi Grigorian, John Groh, Chris Groppi, Yilun Guan, Jon E. Gudmundsson, Mark Halpern, Dongwon Han, Peter Hargrave, Kathleen Harrington, Masaya Hasegawa, Matthew Hasselfield, Makoto Hattori, Victor Haynes, Masashi Hazumi, Erin Healy, Shawn W. Henderson, Brandon Hensley, Carlos Hervias-Caimapo, Charles A. Hill, J. Colin Hill, Gene Hilton, Matt Hilton, Adam D. Hincks, Gary Hinshaw, Renee Hložek, Shirley Ho, Shuay-Pwu Patty Ho, Thuong D. Hoang, Jonathan Hoh, Selim C. Hotinli, Zhiqi Huang, Johannes Hubmayr, Kevin Huffenberger, John P. Hughes, Anna Ijjas, Margaret Ikape, Kent Irwin, Andrew H. Jaffe, Bhuvnesh Jain, Oliver Jeong, Matthew Johnson, Daisuke Kaneko, Ethan D. Karpel, Nobuhiko Katayama, Brian Keating, Reijo Keskitalo, Theodore Kisner, Kenji Kiuchi, Jeff Klein, Kenda Knowles, Anna Kofman, Brian Koopman, Arthur Kosowsky, Nicoletta Krachmalnicoff, Akito Kusaka, Paul La Plante, Jacob Lashner, Adrian Lee, Eunseong Lee, Antony Lewis, Yaqiong Li, Zack Li, Michele Limon, Eric Linder, Jia Liu, Carlos Lopez-Caraballo, Thibaut Louis, Marius Lungu, Mathew Madhavacheril, Daisy Mak, Felipe Maldonado, Hamdi Mani, Ben Mates, Frederick Matsuda, Loïc Maurin, Phil Mauskopf, Andrew May, Nialh McCallum, Heather McCarrick, Chris McKenney, Jeff McMahon, P. Daniel Meerburg, James Mertens, Joel Meyers, Amber Miller, Mark Mirmelstein, Kavilan Moodley, Jenna Moore, Moritz Munchmeyer, Charles Munson, Masaaki Murata, Sigurd Naess, Toshiya Namikawa, Federico Nati, Martin Navaroli, Laura Newburgh, Ho Nam Nguyen, Andrina Nicola, Mike Niemack, Haruki Nishino, Yume Nishinomiya, John Orlowski-Scherer, Luca Pagano,

Bruce Partridge, Francesca Perrotta, Phumlani Phakathi, Lucio Piccirillo, Elena Pierpaoli, Giampaolo Pisano, Davide Poletti, Roberto Puddu, Giuseppe Puglisi, Chris Raum, Christian L. Reichardt, Mathieu Remazeilles, Yoel Rephaeli, Dominik Riechers, Felipe Rojas, Aditya Rotti, Anirban Roy, Sharon Sadeh, Yuki Sakurai, Maria Salatino, Mayuri Sathyanarayana Rao, Lauren Saunders, Emmanuel Schaan, Marcel Schmittfull, Neelima Sehgal, Joseph Seibert, Uros Seljak, Paul Shellard, Blake Sherwin, Meir Shimon, Carlos Sierra, Jonathan Sievers, Cristobal Sifon, Precious Sikhosana, Maximiliano Silva-Feaver, Sara M. Simon, Adrian Sinclair, Kendrick Smith, Wuhyun Sohn, Rita Sonka, David Spergel, Jacob Spisak, Suzanne T. Staggs, George Stein, Jason R. Stevens, Radek Stompor, Aritoki Suzuki, Osamu Tajima, Satoru Takakura, Grant Teply, Daniel B. Thomas, Ben Thorne, Robert Thornton, Hy Trac, Jesse Treu, Calvin Tsai, Carole Tucker, Joel Ullom, Sunny Vagnozzi, Alexander van Engelen, Jeff Van Lanen, Daniel D. Van Winkle, Eve M. Vavagiakis, Clara Vergès, Michael Vissers, Kasey Wagoner, Samantha Walker, Yuhan Wang, Jon Ward, Ben Westbrook, Nathan Whitehorn, Jason Williams, Joel Williams, Edward Wollack, Zhilei Xu, Siavash Yasini, Edward Young, Byeonghee Yu, Cyndia Yu, Fernando Zago, Mario Zannoni, Hezi Zhang, Kaiwen Zheng, Ningfeng Zhu, and Andrea Zonca. The Simons Observatory. In *Bulletin of the American Astronomical Society*, volume 51, page 147, September 2019.

[22] Andrew Liddle. *An Introduction to Modern Cosmology; 2nd ed.* John Wiley Sons Ltd, West Sussex, England, 2003.

[23] L.N. Lowry. *Preparation and Deployment of the Telescopes and POLARBEAR-2b Receiver for the Simons Array Cosmic Microwave Background Polarization Experiment.* PhD thesis, UC San Diego, June 2021.

[24] Dan Maoz. *Astrophysics in a nutshell; 2nd ed.* Princeton Univ. Press, Princeton, NJ, 2016.

[25] J. C. Mather, E. S. Cheng, Jr. Eplee, R. E., R. B. Isaacman, S. S. Meyer, R. A. Shafer, R. Weiss, E. L. Wright, C. L. Bennett, N. W. Boggess, E. Dwek, S. Gulkis, M. G. Hauser, M. Janssen, T. Kelsall, P. M. Lubin, Jr. Moseley, S. H., T. L. Murdock, R. F. Silverberg, G. F. Smoot, and D. T. Wilkinson. A Preliminary Measurement of the Cosmic Microwave Background Spectrum by the Cosmic Background Explorer (COBE) Satellite. , 354:L37, May 1990.

[26] J. Montgomery. *Digital Frequency Domain Multiplexing readout: Design and*

performance of the SPT-3G instrument and LiteBIRD satellite readout. PhD thesis, McGill University, Montreal, Quebec, Canada, 11 2020.

[27] J. R. Pardo, J. Cernicharo, and E. Serabyn. Atmospheric transmission at microwaves (ATM): an improved model for millimeter/submillimeter applications. *IEEE Transactions on Antennas and Propagation*, 49(12):1683–1694, December 2001.

[28] Planck Collaboration, Adam, R., Ade, P. A. R., Aghanim, N., Alves, M. I. R., Arnaud, M., Ashdown, M., Aumont, J., Baccigalupi, C., Banday, A. J., Barreiro, R. B., Bartlett, J. G., Bartolo, N., Battaner, E., Benabed, K., Benoît, A., Benoit-Lévy, A., Bernard, J.-P., Bersanelli, M., Bielewicz, P., Bock, J. J., Bonaldi, A., Bonavera, L., Bond, J. R., Borrill, J., Bouchet, F. R., Boulanger, F., Bucher, M., Burigana, C., Butler, R. C., Calabrese, E., Cardoso, J.-F., Catalano, A., Challinor, A., Chamballu, A., Chary, R.-R., Chiang, H. C., Christensen, P. R., Clements, D. L., Colombi, S., Colombo, L. P. L., Combet, C., Couchot, F., Coulais, A., Crill, B. P., Curto, A., Cuttaia, F., Danese, L., Davies, R. D., Davis, R. J., de Bernardis, P., de Rosa, A., de Zotti, G., Delabrouille, J., Désert, F.-X., Dickinson, C., Diego, J. M., Dole, H., Donzelli, S., Doré, O., Douspis, M., Ducout, A., Dupac, X., Efstathiou, G., Elsner, F., Enßlin, T. A., Eriksen, H. K., Falgarone, E., Fergusson, J., Finelli, F., Forni, O., Frailis, M., Fraisse, A. A., Franceschi, E., Frejsel, A., Galeotta, S., Galli, S., Ganga, K., Ghosh, T., Giard, M., Giraud-Héraud, Y., Gjerløw, E., González-Nuevo, J., Górski, K. M., Gratton, S., Gregorio, A., Gruppuso, A., Gudmundsson, J. E., Hansen, F. K., Hanson, D., Harrison, D. L., Helou, G., Henrot-Versillé, S., Hernández-Monteagudo, C., Herranz, D., Hildebrandt, S. R., Hivon, E., Hobson, M., Holmes, W. A., Hornstrup, A., Hovest, W., Huffenberger, K. M., Hurier, G., Jaffe, A. H., Jaffe, T. R., Jones, W. C., Juvela, M., Keihänen, E., Keskitalo, R., Kisner, T. S., Kneissl, R., Knoche, J., Kunz, M., Kurki-Suonio, H., Lagache, G., Lähteenmäki, A., Lamarre, J.-M., Lasenby, A., Lattanzi, M., Lawrence, C. R., Le Jeune, M., Leahy, J. P., Leonardi, R., Lesgourgues, J., Levrier, F., Liguori, M., Lilje, P. B., Linden-Vørnle, M., López-Caniego, M., Lubin, P. M., Macías-Pérez, J. F., Maggio, G., Maino, D., Mandolesi, N., Mangilli, A., Maris, M., Marshall, D. J., Martin, P. G., Martínez-González, E., Masi, S., Matarrese, S., McGehee, P., Meinhold, P. R., Melchiorri, A., Mendes, L., Mennella, A., Migliaccio, M., Mitra, S., Miville-Deschênes, M.-A., Moneti, A., Montier, L., Morgante, G., Mortlock, D., Moss, A., Munshi, D., Murphy, J. A., Naselsky, P., Nati, F., Natoli, P., Netterfield, C. B., Nørgaard-Nielsen, H. U., Noviello, F., Novikov, D., Novikov, I., Orlando, E., Oxborrow, C. A., Paci, F., Pagano, L., Pajot, F.,

Paladini, R., Paoletti, D., Partridge, B., Pasian, F., Patanchon, G., Pearson, T. J., Perdereau, O., Perotto, L., Perrotta, F., Pettorino, V., Piacentini, F., Piat, M., Pierpaoli, E., Pietrobon, D., Plaszczynski, S., Pointecouteau, E., Polenta, G., Pratt, G. W., Prézeau, G., Prunet, S., Puget, J.-L., Rachen, J. P., Reach, W. T., Rebolo, R., Reinecke, M., Remazeilles, M., Renault, C., Renzi, A., Ristorcelli, I., Rocha, G., Rosset, C., Rossetti, M., Roudier, G., Rubiño-Martín, J. A., Rusholme, B., Sandri, M., Santos, D., Savelainen, M., Savini, G., Scott, D., Seiffert, M. D., Shellard, E. P. S., Spencer, L. D., Stolyarov, V., Stompor, R., Strong, A. W., Sudiwala, R., Sunyaev, R., Sutton, D., Suur-Uski, A.-S., Sygnet, J.-F., Tauber, J. A., Terenzi, L., Toffolatti, L., Tomasi, M., Tristram, M., Tucci, M., Tuovinen, J., Umana, G., Valenziano, L., Valiviita, J., Van Tent, F., Vielva, P., Villa, F., Wade, L. A., Wandelt, B. D., Wehus, I. K., Wilkinson, A., Yvon, D., Zacchei, A., and Zonca, A. Planck 2015 results - x. diffuse component separation: Foreground maps. *A&A*, 594:A10, 2016.

[29] Planck Collaboration, P. A. R. Ade, N. Aghanim, C. Armitage-Caplan, M. Arnaud, M. Ashdown, F. Atrio-Barandela, J. Aumont, C. Baccigalupi, A. J. Banday, R. B. Barreiro, J. G. Bartlett, E. Battaner, K. Benabed, A. Benoît, A. Benoit-Lévy, J.-P. Bernard, M. Bersanelli, P. Bielewicz, J. Bobin, J. J. Bock, A. Bonaldi, J. R. Bond, J. Borrill, F. R. Bouchet, M. Bridges, M. Bucher, C. Burigana, R. C. Butler, E. Calabrese, B. Cappellini, J.-F. Cardoso, A. Catalano, A. Challinor, A. Chamballu, R.-R. Chary, X. Chen, H. C. Chiang, L.-Y Chiang, P. R. Christensen, S. Church, D. L. Clements, S. Colombi, L. P. L. Colombo, F. Couchot, A. Coulais, B. P. Crill, A. Curto, F. Cuttaia, L. Danese, R. D. Davies, R. J. Davis, P. de Bernardis, A. de Rosa, G. de Zotti, J. Delabrouille, J.-M. Delouis, F.-X. Désert, C. Dickinson, J. M. Diego, K. Dolag, H. Dole, S. Donzelli, O. Doré, M. Douspis, J. Dunkley, X. Dupac, G. Efstathiou, F. Elsner, T. A. Enßlin, H. K. Eriksen, F. Finelli, O. Forni, M. Frailis, A. A. Fraisse, E. Franceschi, T. C. Gaier, S. Galeotta, S. Galli, K. Ganga, M. Giard, G. Giardino, Y. Giraud-Héraud, E. Gjerløw, J. González-Nuevo, K. M. Górski, S. Gratton, A. Gregorio, A. Gruppuso, J. E. Gudmundsson, J. Haissinski, J. Hamann, F. K. Hansen, D. Hanson, D. Harrison, S. Henrot-Versillé, C. Hernández-Monteagudo, D. Herranz, S. R. Hildebrandt, E. Hivon, M. Hobson, W. A. Holmes, A. Hornstrup, Z. Hou, W. Hovest, K. M. Huffenberger, A. H. Jaffe, T. R. Jaffe, J. Jewell, W. C. Jones, M. Juvela, E. Keihänen, R. Keskitalo, T. S. Kisner, R. Kneissl, J. Knoche, L. Knox, M. Kunz, H. Kurki-Suonio, G. Lagache, A. Lähteenmäki, J.-M. Lamarre, A. Lasenby, M. Lattanzi, R. J. Laureijs, C. R. Lawrence, S. Leach, J. P. Leahy, R. Leonardi, J. León-Tavares, J. Lesgour-

gues, A. Lewis, M. Liguori, P. B. Lilje, M. Linden-Vørnle, M. López-Caniego, P. M. Lubin, J. F. Macías-Pérez, B. Maffei, D. Maino, N. Mandolesi, M. Maris, D. J. Marshall, P. G. Martin, E. Martínez-González, S. Masi, M. Massardi, S. Matarrese, F. Matthai, P. Mazzotta, P. R. Meinhold, A. Melchiorri, J.-B. Melin, L. Mendes, E. Menegoni, A. Mennella, M. Migliaccio, M. Millea, S. Mitra, M.-A. Miville-Deschênes, A. Moneti, L. Montier, G. Morgante, D. Mortlock, A. Moss, D. Munshi, J. A. Murphy, P. Naselsky, F. Nati, P. Natoli, C. B. Netterfield, H. U. Nørgaard-Nielsen, F. Noviello, D. Novikov, I. Novikov, I. J. O'Dwyer, S. Osborne, C. A. Oxborrow, F. Paci, L. Pagano, F. Pajot, R. Paladini, D. Paoletti, B. Partridge, F. Pasian, G. Patanchon, D. Pearson, T. J. Pearson, H. V. Peiris, O. Perdereau, L. Perotto, F. Perrotta, V. Pettorino, F. Piacentini, M. Piat, E. Pierpaoli, D. Pietrobon, S. Plaszczynski, P. Platania, E. Pointecouteau, G. Polenta, N. Ponthieu, L. Popa, T. Poutanen, G. W. Pratt, G. Prézeau, S. Prunet, J.-L. Puget, J. P. Rachen, W. T. Reach, R. Rebolo, M. Reinecke, M. Remazeilles, C. Renault, S. Ricciardi, T. Riller, I. Ristorcelli, G. Rocha, C. Rosset, G. Roudier, M. Rowan-Robinson, J. A. Rubiño-Martín, B. Rusholme, M. Sandri, D. Santos, M. Savelainen, G. Savini, D. Scott, M. D. Seiffert, E. P. S. Shellard, L. D. Spencer, J.-L. Starck, V. Stolyarov, R. Stompor, R. Sudiwala, R. Sunyaev, F. Sureau, D. Sutton, A.-S. Suur-Uski, J.-F. Sygnet, J. A. Tauber, D. Tavagnacco, L. Terenzi, L. Toffolatti, M. Tomasi, M. Tristram, M. Tucci, J. Tuovinen, M. Türler, G. Umana, L. Valenziano, J. Valiviita, B. Van Tent, P. Vielva, F. Villa, N. Vittorio, L. A. Wade, B. D. Wandelt, I. K. Wehus, M. White, S. D. M. White, A. Wilkinson, D. Yvon, A. Zacchei, and A. Zonca. iplanck/i2013 results. XVI. cosmological parameters. *Astronomy &amp Astrophysics*, 571:A16, October 2014.

[30] Planck Collaboration, N. Aghanim, M. Arnaud, M. Ashdown, J. Aumont, C. Baccigalupi, A. J. Banday, R. B. Barreiro, J. G. Bartlett, N. Bartolo, E. Battaner, K. Benabed, A. Benoît, A. Benoit-Lévy, J. P. Bernard, M. Bersanelli, P. Bielewicz, J. J. Bock, A. Bonaldi, L. Bonavera, J. R. Bond, J. Borrill, F. R. Bouchet, F. Boulanger, M. Bucher, C. Burigana, R. C. Butler, E. Calabrese, J. F. Cardoso, A. Catalano, A. Challinor, H. C. Chiang, P. R. Christensen, D. L. Clements, L. P. L. Colombo, C. Combet, A. Coulais, B. P. Crill, A. Curto, F. Cuttaia, L. Danese, R. D. Davies, R. J. Davis, P. de Bernardis, A. de Rosa, G. de Zotti, J. Delabrouille, F. X. Désert, E. Di Valentino, C. Dickinson, J. M. Diego, K. Dolag, H. Dole, S. Donzelli, O. Doré, M. Douspis, A. Ducout, J. Dunkley, X. Dupac, G. Efstathiou, F. Elsner, T. A. Enßlin, H. K. Eriksen, J. Fergusson, F. Finelli, O. Forni, M. Frailis, A. A. Fraisse, E. Franceschi, A. Frejsel,

S. Galeotta, S. Galli, K. Ganga, C. Gauthier, M. Gerbino, M. Giard, E. Gjerløw, J. González-Nuevo, K. M. Górski, S. Gratton, A. Gregorio, A. Gruppuso, J. E. Gudmundsson, J. Hamann, F. K. Hansen, D. L. Harrison, G. Helou, S. Henrot-Versillé, C. Hernández-Monteagudo, D. Herranz, S. R. Hildebrandt, E. Hivon, W. A. Holmes, A. Hornstrup, K. M. Huffenberger, G. Hurier, A. H. Jaffe, W. C. Jones, M. Juvela, E. Keihänen, R. Keskitalo, K. Kiiveri, J. Knoche, L. Knox, M. Kunz, H. Kurki-Suonio, G. Lagache, A. Lähteenmäki, J. M. Lamarre, A. Lasenby, M. Lattanzi, C. R. Lawrence, M. Le Jeune, R. Leonardi, J. Lesgourgues, F. Levrier, A. Lewis, M. Liguori, P. B. Lilje, M. Lilley, M. Linden-Vørnle, V. Lindholm, M. López-Caniego, J. F. Macías-Pérez, B. Maffei, G. Maggio, D. Maino, N. Mandolesi, A. Mangilli, M. Maris, P. G. Martin, E. Martínez-González, S. Masi, S. Matarrese, P. R. Meinhold, A. Melchiorri, M. Migliaccio, M. Millea, S. Mitra, M. A. Miville-Deschênes, A. Moneti, L. Montier, G. Morgante, D. Mortlock, S. Mottet, D. Munshi, J. A. Murphy, A. Narimani, P. Naselsky, F. Nati, P. Natoli, F. Noviello, D. Novikov, I. Novikov, C. A. Oxborrow, F. Paci, L. Pagano, F. Pajot, D. Paoletti, B. Partridge, F. Pasian, G. Patanchon, T. J. Pearson, O. Perdereau, L. Perotto, V. Pettorino, F. Piacentini, M. Piat, E. Pierpaoli, D. Pietrobon, S. Plaszczynski, E. Pointecouteau, G. Polenta, N. Ponthieu, G. W. Pratt, S. Prunet, J. L. Puget, J. P. Rachen, M. Reinecke, M. Remazeilles, C. Renault, A. Renzi, I. Ristorcelli, G. Rocha, M. Rossetti, G. Roudier, B. Rouillé d'Orfeuil, J. A. Rubiño-Martín, B. Rusholme, L. Salvati, M. Sandri, D. Santos, M. Savelainen, G. Savini, D. Scott, P. Serra, L. D. Spencer, M. Spinelli, V. Stolyarov, R. Stompor, R. Sunyaev, D. Sutton, A. S. Suur-Uski, J. F. Sygnet, J. A. Tauber, L. Terenzi, L. Toffolatti, M. Tomasi, M. Tristram, T. Trombetti, M. Tucci, J. Tuovinen, G. Umana, L. Valenziano, J. Valiviita, F. Van Tent, P. Vielva, F. Villa, L. A. Wade, B. D. Wandelt, I. K. Wehus, D. Yvon, A. Zacchei, and A. Zonca. Planck 2015 results. XI. CMB power spectra, likelihoods, and robustness of parameters. , 594:A11, September 2016.

[31] E.E. Quealy. *The POLARBEAR Cosmic Microwave Background Polarization Experiment and Anti-Reflection Coatings for Millimeter Wave Observations.* PhD thesis, University of California, Berkeley, Berkeley, California, USA, 2012.

[32] Kana Sakaguri, Masaya Hasegawa, Yuki Sakura, Charles Hill, and Akito Kusaka. Broadband multi-layer anti-reflection coatings with mullite and duroid for half-wave plates and alumina filters for CMB polarimetry. In Press.

[33] Randy W. Simon, Michael J. Burns, Mark S. Colclough, Greg Zaharchuk, and Robin Cantor. Mr. SQUID User's Guide.

[34] Christopher Smeenk and George Ellis. Philosophy of Cosmology. In Edward N. Zalta, editor, *The Stanford Encyclopedia of Philosophy*. Metaphysics Research Lab, Stanford University, Winter 2017 edition, 2017.

[35] Satoru Takakura, Mario Aguilar, Yoshiki Akiba, Kam Arnold, Carlo Baccigalupi, Darcy Barron, Shawn Beckman, David Boettger, Julian Borrill, Scott Chapman, Yuji Chinone, Ari Cukierman, Anne Ducout, Tucker Elleflot, Josquin Errard, Giulio Fabbian, Takuro Fujino, Nicholas Galitzki, Neil Goeckner-Wald, Nils W. Halverson, Masaya Hasegawa, Kaori Hattori, Masashi Hazumi, Charles Hill, Logan Howe, Yuki Inoue, Andrew H. Jaffe, Oliver Jeong, Daisuke Kaneko, Nobuhiko Katayama, Brian Keating, Reijo Keskitalo, Theodore Kisner, Nicoletta Krachmalnicoff, Akito Kusaka, Adrian T. Lee, David Leon, Lindsay Lowry, Frederick Matsuda, Tomotake Matsumura, Martin Navaroli, Haruki Nishino, Hans Paar, Julien Peloton, Davide Poletti, Giuseppe Puglisi, Christian L. Reichardt, Colin Ross, Praween Siritanasak, Aritoki Suzuki, Osamu Tajima, Sayuri Takatori, and Grant Teply. Performance of a continuously rotating half-wave plate on the POLARBEAR telescope. *Journal of Cosmology and Astroparticle Physics*, 2017(05):008–008, May 2017.

[36] Huan Tran, Adrian Lee, Shaul Hanany, Michael Milligan, and Tom Renbarger. Comparison of the crossed and the gregorian mizuguchi-dragone for wide-field millimeter-wave astronomy. *Appl. Opt.*, 47(2):103–109, January 2008.

[37] Huan T Tran. Polarization comparison between on-axis and off-axis dual reflector telescopes: Zemax and grasp8 simulations. *New Astronomy Reviews*, 47(11):1091–1096, 2003. Proceedings of the Workshop on The Cosmic Microwave Background Radiation and its Polarization.

[38] E. M. Vavagiakis, S. W. Henderson, K. Zheng, H.-M. Cho, N. F. Cothard, B. Dober, S. M. Duff, P. A. Gallardo, G. Hilton, J. Hubmayr, K. D. Irwin, B. J. Koopman, D. Li, F. Nati, M. D. Niemack, C. D. Reintsema, S. Simon, J. R. Stevens, A. Suzuki, and B. Westbrook. Magnetic Sensitivity of AlMn TESes and Shielding Considerations for Next-Generation CMB Surveys. volume 193, pages 288–297, May 2018.

[39] B. Westbrook, P. A. R. Ade, M. Aguilar, Y. Akiba, K. Arnold, C. Baccigalupi, D. Barron, D. Beck, S. Beckman, A. N. Bender, F. Bianchini, D. Boettger, J. Borrill, S. Chapman, Y. Chinone, G. Coppi, K. Crowley, A. Cukierman, T. de Haan, R. Dünner, M. Dobbs, T. Elleflot, J. Errard, G. Fabbian, S. M. Feeney, C. Feng, G. Fuller, N. Galitzki, A. Gilbert, N. Goeckner-Wald, J. Groh, N. W.

Halverson, T. Hamada, M. Hasegawa, M. Hazumi, C. A. Hill, W. Holzapfel, L. Howe, Y. Inoue, G. Jaehnig, A. Jaffe, O. Jeong, D. Kaneko, N. Katayama, B. Keating, R. Keskitalo, T. Kisner, N. Krachmalnicoff, A. Kusaka, M. Le Jeune, A. T. Lee, D. Leon, E. Linder, L. Lowry, A. Madurowicz, D. Mak, F. Matsuda, A. May, N. J. Miller, Y. Minami, J. Montgomery, M. Navaroli, H. Nishino, J. Peloton, A. Pham, L. Piccirillo, D. Plambeck, D. Poletti, G. Puglisi, C. Raum, G. Rebeiz, C. L. Reichardt, P. L. Richards, H. Roberts, C. Ross, K. M. Rotermund, Y. Segawa, B. Sherwin, M. Silva-Feaver, P. Siritanasak, R. Stompor, A. Suzuki, O. Tajima, S. Takakura, S. Takatori, D. Tanabe, R. Tat, G. P. Teply, A. Tikhomirov, T. Tomaru, C. Tsai, N. Whitehorn, and A. Zahn. The POLARBEAR-2 and Simons Array Focal Plane Fabrication Status. *Journal of Low Temperature Physics*, 193(5-6):758–770, December 2018.